TECHNISCHE UNIVERSITÄT MÜNCHEN

FAKULTÄT FÜR ELEKTROTECHNIK UND INFORMATIONTECHNIK

Charge Transport in Organic Field-Effect Transistors: A Multi-dimensional Theoretical Study

Mohammed A. F. I. Darwish, M.Sc.

Vollständiger Abdruck der von der Fakultät für Elektrotechnik und Informationtechnik der Technischen Universität München zur Erlangung des akademischen Grades eines

Doktor-Ingenieurs

genehmigten Dissertation.

Vorsitzender:	Prof. Dr.-Ing. Andreas Jossen
Prüfer der Dissertation:	1. Prof. Dr. rer. nat. Alessio Gagliardi
	2. Assoc. Prof. Aldo Di Carlo, Ph.D.

Die Dissertation wurde am 19.06.2019 bei der Technischen Universität München eingereicht und durch die Fakultät für Elektrotechnik und Informationtechnik am 04.10.2019 angenommen.

To my parents and three sisters.

Acknowledgments

First and foremost, I would like to thank Prof. Dr. Alessio Gagliardi for giving me the opportunity to work in his research group. This begun with writing my Master's thesis, and now this doctoral dissertation. He provided me with the freedom to express myself, and the motivation to undertake the challenge presented to me over the past few years. Alessio was always ever-present for the engaging discussions and meetings, from which I learned a lot. Without his supervision, the work on this thesis would have not been possible, and for that I am grateful.

I further acknowledge the Deutsche Forschungsgemeinschaft (DFG) for funding my research project.

I would also like to thank my fellow colleagues and friends Waldemar Kaiser, Michael Rinderle, Dr. Tim Albes, and Marlon Rück for their support, as well as the countless and interesting discussions on various topics being related either to our scientific research or otherwise. All four of you always had my best interest at heart, and helping me to improve on myself.

Moreover, I would like to extend my thanks to our collaborators that I had the pleasure to work alongside. This goes out to the experimental groups of Prof. Dr. Marc Tornow from the *Professorship of Molecular Electronics, TUM*, and Priv.-Doz. Dr. Bert Nickel from the *Faculty of Physics and Center of NanoScience (CeNS), LMU*, for their valuable insight on the work presented in this thesis.

Last but definitely not least, special thanks and gratitude goes out to my family. My mother, father, and three sisters. Without their unwavering, unconditional love and support from the moment I decided to pursue my post graduate studies, none of this would have been possible. They were always there, by my side during both the good and difficult times, and for that I am immensely thankful. This thesis is dedicated to them.

List Of Publications

Journal articles

- M. Darwish, H. Boysan, C. Liewald, B. Nickel, A. Gagliardi: "A resistor network simulation model for laser-scanning photo-current microscopy to quantify low conductance regions in organic thin films," *Org. Electron., 62, 474-480 (2018)*

- M. Darwish, A. Gagliardi: "A drift-diffusion simulation model for organic field effect transistors: on the importance of the gaussian density of states and traps," *J. Phys. D.: Appl. Phys.* **(Submitted)**

Conference proceedings

- M. Darwish, A. Gagliardi: "Modeling and simulation of trap densities in organic thin films," *Proc. IEEE International Conference on Nanotechnology (2017)*, Pittsburgh, Pennsylvania, USA

- T. Meister, F. Ellinger, ..., M. Darwish, A. Gagliardi, ...: "Program FFlexCom - High frequency flexible bendable electronics for wireless communication systems," *Proc. IEEE International Conference on Microwaves, Antennas, Communications and Electronic Systems (COMCAS) (2017)*, Tel-Aviv, Israel

Abstract

Research into organic electronics has gathered a lot of pace over the past decades. Devices based on organic semiconductors can complement current technologies, but also possess numerous advantages over their inorganic counterparts. The possibility of low cost production on a large scale, obtaining devices with bendable capabilities, and the vast array of materials available are a number of reasons behind the extensive effort placed into studying such a technology. Examples include organic- field effect transistors (OFETs) for radio frequency identification tags or sensors, light emitting diodes (OLEDs) for displays, and solar cells (OSCs) for energy harvesting. Whichever device is chosen, they all must exhibit and maintain good performance measures. In OFETs which are the main focus in this study, these measures are high charge carrier mobilities, low operating voltages, and device stability. The need (or want) to achieve lower device dimensions, coupled with the clear difference in the nature of charge transport between organic and inorganic semiconductors, this led to a shift in knowledge (a requirement) from mainly device engineering to that of a multi-disciplinary one. This included engineering, material science, as well as chemistry. Furthermore, despite the many important steps taken towards understanding charge transport in organics, the exact nature is yet to be clear, and the experimental work has been guided mostly by a trial and error analysis.

A theoretical approach is therefore required. Not to replace experimental investigations, rather to aid them in providing a much needed insight towards a much more comprehensive understanding. The complex nature of charge transport in organic semiconductors requires theoretical investigations to span across the entire dimension scale. Firstly, on the atomistic scale, this involves uncovering how charges flow between individual molecules (or indeed atoms) through electronic structure and transport calculations based on first principle methods. Secondly, comes the macro-scale, focusing on device characterization by utilizing models proposed used to describe charge transport in the presence of performance limiting factors such as charge trapping. Thirdly, at the top of the dimension scale are circuit level analysis, used to further expand on the macro-scale investigations. Models considering circuital elements such as resistors can also be used to validate experimental data.

The work in this thesis further acts as a basis towards a multi-scale approach, where separate investigations can be connected to (dependent on) one another. Results from a lower dimension analysis is passed forward to the next level. This could in fact prove crucial towards achieving a much sought after understanding on the nature of charge transport in organic materials and devices.

Kurzfassung

Die Forschung im Bereich organische Elektronik hat in den letzten Jahrzehnten stark an Tempo gewonnen. Bauteile basierend auf organischen Halbleitern können aktuelle Technologien ergänzen, haben aber auch zahlreiche Vorteile gegenüber ihren anorganischen Pendants. Die Möglichkeit zur kostengünstigen Produktion im großen Maßstab, die Herstellung biegsamer Bauteile und die große Vielzahl an verfügbaren Materialien sind einige der Gründe für die großen Anstrengungen, die unternommen werden um diese Technologie zu erforschen. Einige Beispiele sind organische Feldeffekttransistoren (OFETs) für Radiofrequenz-Identifikations-Marker oder Sensoren, organische Leuchtdioden (OLEDs) für Displays und organische Solarzellen (OSCs) zur Energiegewinnung. Für alle Bauteile gilt, sie müssen gute Leistungsdaten aufweisen und aufrechterhalten. Bei OFETs, die im Mittelpunkt dieser Arbeit stehen, sind dies hohe Ladungsträgermobilität, geringe Betriebsspannung und die Langzeitstabilität des Bauteils. Die Notwendigkeit (oder der Wunsch) kleinere Bauteilabmessungen zu erreichen und die Tatsache, dass sich der Ladungstransport organischen Halbleitern grundsätzlich von dem anorganischer Halbleiter unterscheidet, führen auch zu einer Verschiebung der Anforderungen von hauptsächlich Bauteilentwicklung hin zu interdisziplinärem Wissen. Dazu gehören Ingenieurwesen, Materialwissenschaften und Chemie. Außerdem ist trotz der vielen wichtigen Schritte zur Untersuchung des Ladungstransports in organischen Materialien die genaue Natur desselben noch nicht klar und experimentelle Arbeiten werden häufig von dem Trial-and-Error-Prinzip geleitet.

Daher ist ein theoretischer Ansatz erforderlich. Nicht um experimentelle Untersuchungen zu ersetzen, sondern diese zu unterstützen und ihnen den dringend benötigten Einblick in ein weit umfassenderes Verständnis zu geben. Die Komplexität des Ladungstransports in organischen Halbleitern erfordert theoretische Untersuchungen auf allen Größenskalen. Erstens, auf atomistischer Ebene geht es darum herauszufinden wie sich Ladungen zwischen Molekülen (oder einzelnen Atomen) bewegen. Dies geschieht durch Untersuchungen der elektronischen Struktur der Moleküle basierend auf grundlegenden Methoden. Zweitens, auf der Makroebene liegt der Fokus auf der Bauteilcharakterisierung. Hier werden Modelle vorgestellt, die den Ladungstransport in Gegenwart limitierender Faktoren, wie Ladungsträger-Fallen, untersuchen. Drittens, am oberen Ende der Größenskala stehen elektrische Schaltkreise, mit denen die Untersuchungen auf der Makroebene weiter ausgebaut werden sollen. Modelle die Schaltungselemente wie Widerstände verwenden, können auch zur Validierung experimenteller Daten verwendet werden.

Diese Arbeit dient außerdem als Basis für zukünftige Multi-Skalen-Methoden, bei denen die einzelnen Untersuchungen verbunden werden können und aufeinander aufbauen. Ergebnisse von Analysen einer kleinen Größenskala werden in die nächst größere Skala weitergegeben. Dieses Vorgehen könnte sich auf dem Weg ein tieferes Verständnis des Ladungstransportes in organischen Materialien und Bauteilen zu erlangen als entscheidend erweisen.

Contents

Chapter 1

Introduction

Since their introduction in the 1980s, organic based devices have been at the forefront of the research community due to their flexible properties, as well as the large scale roll-to-roll cheaper fabrication procedures. Eventhough, inorganic semiconductors have been (and still are to a large extent) the go-to materials for today's electronic industry, research have come a long way in improving performance measures of organic based devices. Such devices include organic- solar cells (OSCs) [1, 2, 3], and light emitting diodes (OLEDs) [4, 5, 6, 7]. The latter one especially made a breakthrough over the past years on a commercial scale for display applications (i.e. mobile phones, and the recently introduced OLED TVs). Organic field effect transistors (OFETs) are another member of this increasingly interesting family of novel devices. One advantageous attribute of OFETs, is that they can be used as the only functioning transistor architecture within integrated circuits for certain applications. Radio frequency identification tags (RFIDs) [8, 9], and sensors [10, 11, 12] serve as two examples. OFETs can also be used as "driver" transistors. This implies OFETs being responsible for switching other devices on and off. To this day most of the OLED based displays are driven by a back-plane of inorganic transistors. On the other hand, combining both OFETs and OLEDs together into one ecosystem would certainly be regarded as a massive achievement. An excellent review on the use of organic transistors in optical displays and microelectronic applications can be found here [13].

1.1 OFETs: the working principle

As the main theme of this chapter and indeed the entirety of the work that will be presented focuses on OFETs, it would be useful to briefly outline their working principle. Organic transistors are identical to their inorganic counterparts, in that they consist of a metal-insulator-semiconductor structure (MISFET). More commonly known as a MOSFET, where the insulator is usually an oxide (see Fig. 1.1). Another similarity subscribed to OFETs, is the widely known theory of "A Unipolar Field Effect Transistor" (i.e. the gradual channel approximation (GCA)) put forward by William Shockley [14]. A number of assumptions are associated with the GCA, namely: (1) charges are injected/extracted via ohmic contacts, (2) no diffusion of charges, and (3) a bias independent mobility [15, 16]. Within the GCA, the current passing though a transistor is defined as,

$$I_{DS} = \frac{\mu C_{ox} W}{L}\left((V_{GS} - V_{TH})V_{DS} - \frac{V_{DS}^2}{2}\right) \tag{1.1a}$$

$$\text{for} \qquad |V_{DS}| < |V_{GS} - V_{TH}| \qquad \text{(linear regime)}$$

$$I_{DS} = \frac{\mu C_{ox} W}{2L}(V_{GS} - V_{TH})^2 \tag{1.1b}$$

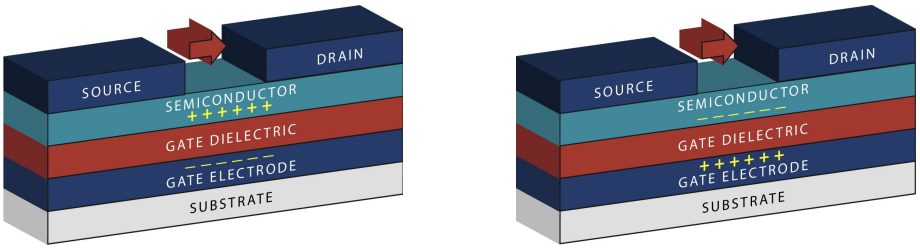

(a) p-type OFET **(b) n-type OFET**

Fig. 1.1: Example device topologies of OFETs exhibiting either **(a)** p-type, or **(b)** n-type conduction. Charges flow from source to drain as indicated by the red arrow.

$$\text{for} \qquad |V_{DS}| \geq |V_{GS} - V_{TH}| \qquad \text{(saturation regime)}$$

where I_{DS} is the drain-source current, V_{DS} the drain-source voltage, V_{GS} the gate-source voltage, V_{TH} the threshold voltage, μ the charge mobility, C_{ox} the gate oxide capacitance, W and L the channel width and length respectively. Rearranging Eqs. (1.1a)-(1.1b) gives the mobility

$$\mu_{lin} = \frac{L}{WC_{ox}V_{DS}} \frac{\partial I_{DS_{lin}}}{\partial V_{GS}} \tag{1.2a}$$

$$\mu_{sat} = \frac{2L}{WC_{ox}} \left(\frac{\partial \sqrt{I_{DS_{sat}}}}{\partial V_{GS}} \right)^2 \tag{1.2b}$$

where μ_{lin} and μ_{sat} are the linear and saturation mobilities. Two important characteristics are always plotted to describe the behaviour of a transistor. Firstly, the output characteristics show the relation I_{DS} vs. V_{DS} at different V_{GS}. Here the linear and saturation regimes should be clearly depicted. Secondly, the transfer characteristics show the relation I_{DS} vs. V_{GS} at different V_{DS}. The transfer characteristics are particularly useful because they show the transition between off- and on-states of a device. Transfer characteristics depicting the relation $\sqrt{I_{DS}}$ vs. V_{GS} are used to extract mobilities (i.e. slope), and threshold voltages (i.e. for $I_{DS} = 0$).

A transistor that complies with the GCA, and can be characterized with the aforementioned relations, is labeled as an ideal device. Considering the difference in chemical and mechanical properties between inorganic and organic materials, the latter suffers from the lack of extended states and a large amount of defects, leading to OFETs exhibiting non-ideal behaviour [17]. Nevertheless, the research community kept on applying the GCA to OFETs. This required a much deeper look into the literature, examining the reported performance measures.

1.2 Current issues and recent progress in OFETs

In a recent review published by Paterson *et al.* [18], the autors provide a graphic showing the progress achieved in OFET mobilities over the past 30 years. According to this graphic, both p- and n-type mobilities have reached up to 20 cm^2/Vs and 10 cm^2/Vs respectively (see Fig. 1.2(a)). Furthermore, Fig. 1.2(b) illustrates that mobilities of solution processed OFETs are comparable with that of single crystal and vacuum processed OFETs. This definitely spells significant improvements, but they go on to highlight that these values do not paint the entire picture. In reality there is what they refer to as a "mobility hype". This hype points towards that

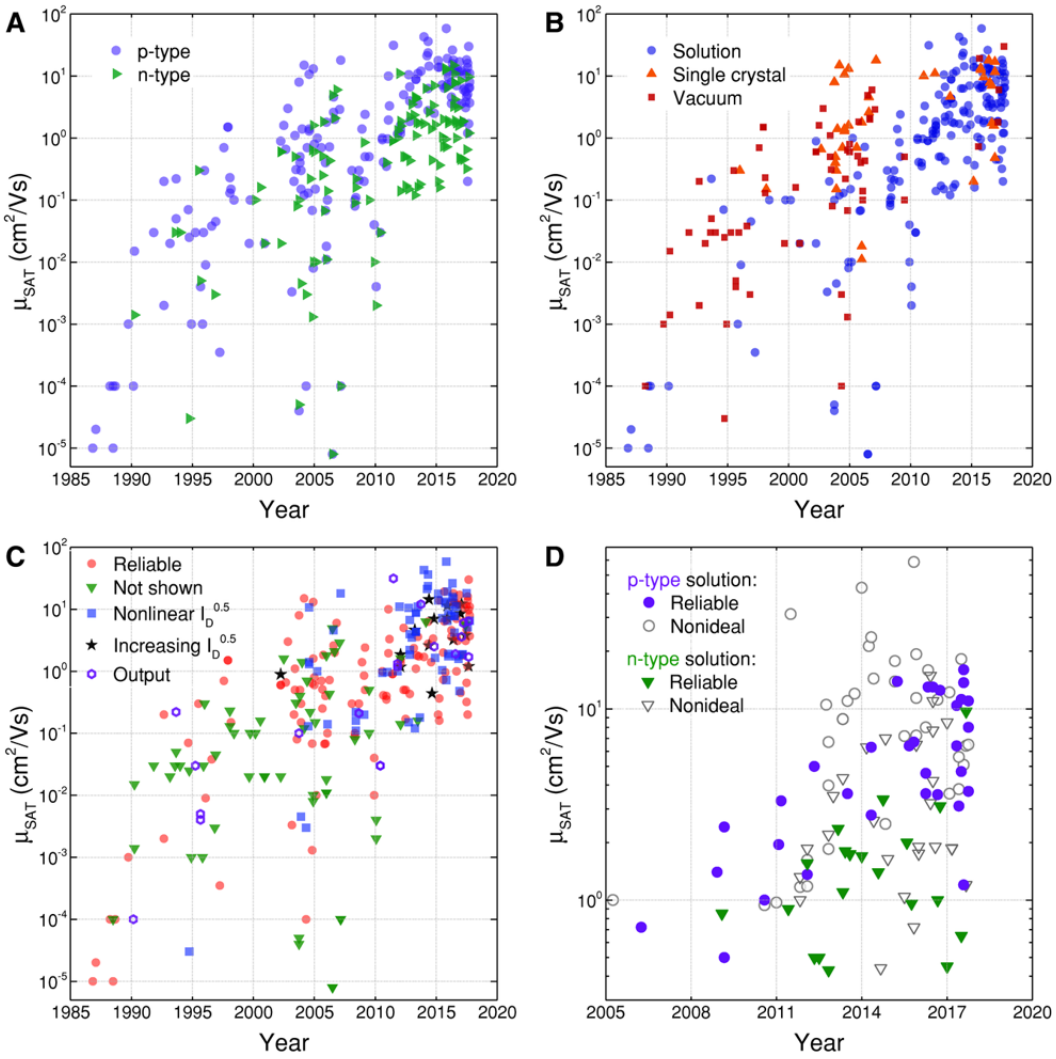

Fig. 1.2: Progress of OFET mobilities reported in the literature over the past 30 years. **(a)** Reported mobilities with respect to charge carrier type. **(b)** Reported mobilities based on material/device processing technique. **(c)** Extracted mobilities from the presented data sets (i.e. I-V characteristics) in the literature. **(d)** A focus on the reliability of extracted mobilities only from solution processing techniques for both charge carrier types. *Reproduced with permission from [18]. Copyright 2018 Wiley-VCH Verlag GmbH*

there has been an overestimation in OFET mobilities, as a consequence of extracting it from characteristics that show non-ideal behaviour. This non-ideality is depicted as a "double slope" or "kink", leading to overestimated mobilities from the steeper portion of the transfer characteristics. Contact resistance has been identified as the main cause for the resulting non-idealities [19, 20, 21, 22].

Contact resistances arise from the difference in alignment between the metal workfunction and the energy band of the organic material. This difference creates a built in potential as charges are transferred from the organic to the metal in order to achieve balance in energy level between

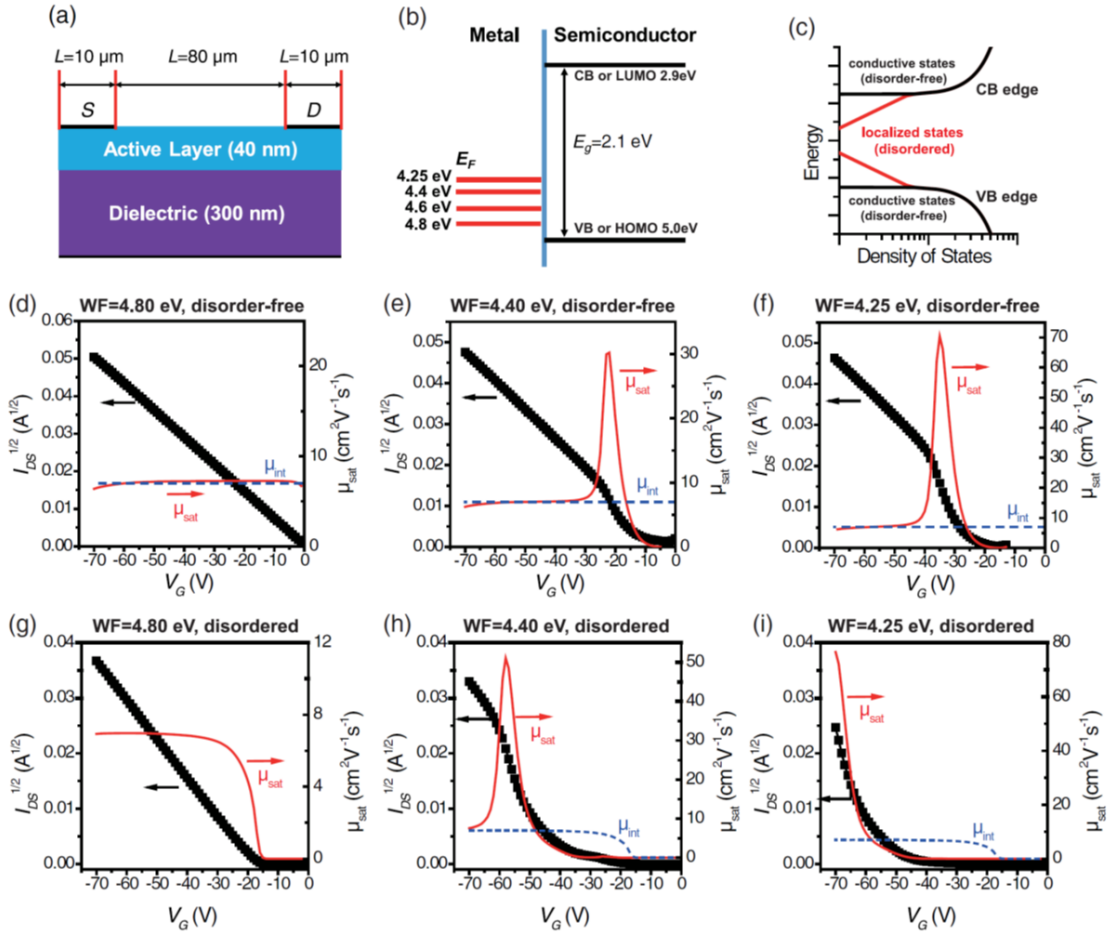

Fig. 1.3: Effect of injection barriers, and consequently contact resistances on extracted mobilities. Schematic of **(a)** device structure, **(b)** metal workfunctions and semiconductor energy levels, **(c)** density of states for disorder-free and disordered semiconductors. **(d,g)** Reliable characteristics at low injection barriers/contact resistances for both disorder-free and disordered cases. **(e-f,h-i)** Manifestation of non-idealities in the characteristics with increasing injection barriers/contact resistances for both disorder-free, and disordered cases and it's effect on extracted mobilities. *Reproduced with permission from [23]. Copyright 2017 American Physical Society*

the respective surfaces. As a result a potential barrier is formed (known as a Schottky barrier), negatively affecting charge injection. Hence the total drain current, according to Ohm's law, is dependent on both contact and channel resistances,

$$I_{DS} = \frac{V_{DS}}{(R_C + R_{CH})} \tag{1.3}$$

where R_C and R_{CH} are the resistances of the contact and channel respectively. Fig. 1.2(c), shows the effect of non-ideal OFET behaviour has on the reported mobilities. Shown data points represent extracted mobilites based on: (i) reliable data, (ii) no characteristics were provided

showing how the mobility was evaluated, (iii) an observed kink or (iv) steep increase in the transfer characteristics, and finally (v) non-saturating output characteristics. As it can be seen, a significant amount of reported mobilities represent non-ideal OFET behaviour. This trend increased with passing years, as intrinsic material mobility is improved, placing an even bigger emphasis on contact resistances. Fig. 1.2(d) narrows down the data sets, by focusing only on solution processed materials.

Furthermore, Liu *et al.* [23] presented simulation results, further highlighting the effect of R_C on the mobility. For a p-type OFET, they varied the barrier between the metal and organic semiconductors in the presence and absence of disorder. When R_C is at a minimum, an ideal behaviour is observed from the transfer characteristics (Fig. (1.3(d,g)). Once the R_C starts to become significant, the kink takes shape (Fig. 1.3(e,h)), leading to an overestimation in the mobility by almost a factor of ten (Fig. 1.3(f)). For the last case of highest R_C with included disorder (Fig. 1.3(i)) no kink is present, yet a steep increase in the current is observed, which is another manifestation leading to overestimating the mobility.

Nevertheless, even in the presence of this mobility hype, there is no denying the fact that improvements in OFET mobilities have been made. Some of the different avenues explored towards improving OFET performance measures will be briefly presented in the following subsections.

1.2.1 p- and n-type organic semiconductors

One of the explored avenues towards improving OFET performance measures are the organic materials available. Unlike inorganics, where there is only a few materials to utilize (silicon being the most common one), there is a wealth of different materials available to choose from for organic based devices. An extensive database of the different materials can be found here [24]. These materials are categorized into two groups. Small molecules and polymers respectively. The former comes with some degree (usually high) of crystallinity, and the latter lends itself towards being amorphous in nature. Moreover, some materials can exhibit both structural forms. There are many organic semiconductors that have been famously investigated, to be either p-type (hole conducting) or n-type (electron conducting). But generally speaking, it mainly relies on the favoured alignment between the energy band of the organic semiconductor (either valence or conduction) and the metal workfunction. Hence, depending on the chosen combination of metal and semiconductor, one material can either be p- or n-type.

Fig. 1.4 shows a few example structures for different p- an n-type materials used for OFETs. Poly(3-hexylthiophene) (P3HT, see Fig. 1.4(a)) is one of the well known polymers used for p-type OFETs. P3HT polymers tend to self organize into lamellar structures, where domains of closely packed backbones are separated by disorder alkyl chains. These polymers have been shown to orient themselves relative to the substrate either in an edge-on or face-on fashion, exhibiting mobilities around $0.1\,\mathrm{cm}^2/\mathrm{Vs}$ [25]. Due to the massive attention that P3HT polymers gained, further improvements to the mobility was achieved. For example, Fei *et al.* [26] reported that by introducing structural deviations to the thiophene backbone, mobilities as high as $4.6\,\mathrm{cm}^2/\mathrm{Vs}$ were measured. N-type OFETs are not reported on as often as that of p-type OFETs. Furthermore, reported mobilities are lower for the former. The main reason behind why n-type OFETs fall short in terms of mobility, is that these organic semiconductors suffer from long term stability. To facilitate electron conduction, n-type organic semiconductors should possess low LUMO levels, in line with a reduction potential below that of water or oxygen, so that n-type OFETs are stable in ambient environments [27]. Polymers based on naphthalene diimide (NDI) cores (see Fig. 1.4(b)) are candidates for n-type OFETs, exhibiting excellent ambient stability and mobilities up to

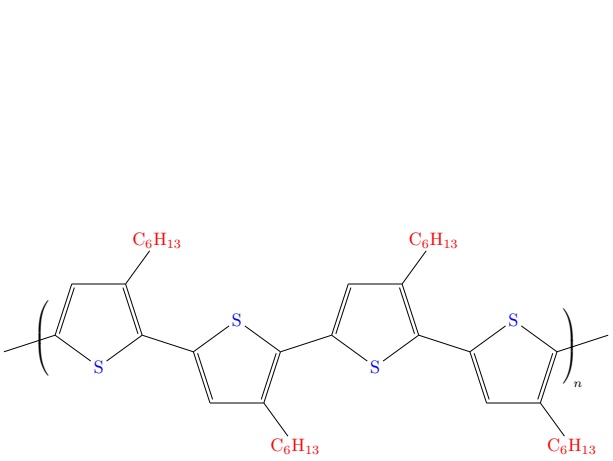

(a) P3HT

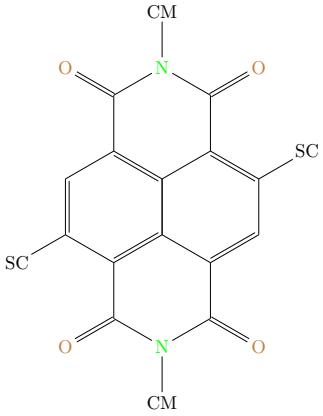

SC: Side Chain;**CM:**Comonomer

(b) Naphthalene Diimide (NDI)

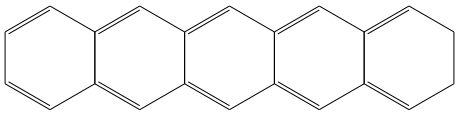

(c) Pentacene

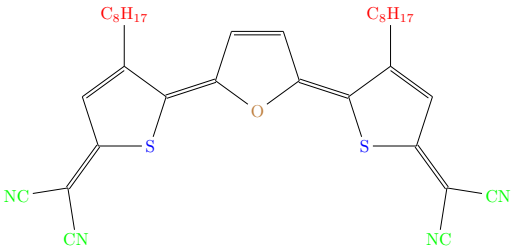

(d) Quinoidal

Fig. 1.4: Molecular structures of organic polymers **(a)** Poly(3-hexylthiophene) (P3HT), **(b)** Naphthalene Diimide (NDI), and organic small molecules **(c)** Pentacene, **(d)** Quinoidal.

0.85 cm^2/Vs [28]. A similar approach of altering the side chain regiochemistry in P3HT was taken by Kim *et al.* [29]. They obtained an NDI based polymer, and fabricated top-gate bottom-contact OFETs with a mobility of 1.8 cm^2/Vs and good on/off ratio of 10^6.

These were two examples of p- and n-type polymer organic semiconductors for OFETs. Pentacene (p-type, Fig. 1.4(c)) [30], and quinoidal semiconductors (n-type, Fig. 1.4(d)) [31] are famous examples of small molecules used for OFETs. For a more extensive review on the various types organic semiconductors, the review by Paterson *et al.* [18] provides an excellent read.

1.2.2 Doping of organic semiconductors

Doping have been a well known and established mechanism used to enhance FET performance. In inorganic devices dopants are added which can either act as a donor or an acceptor. A donor supplies the target semiconductor with excess electrons, while an acceptor withdraws an electron leaving behind a hole for enhanced hole conduction. This mechanism is exactly the same in organic semiconductors. A dopant molecule which can either be electron rich or electron deficient is added to the host molecule and a charge transfer occurs between them. But this charge transfer

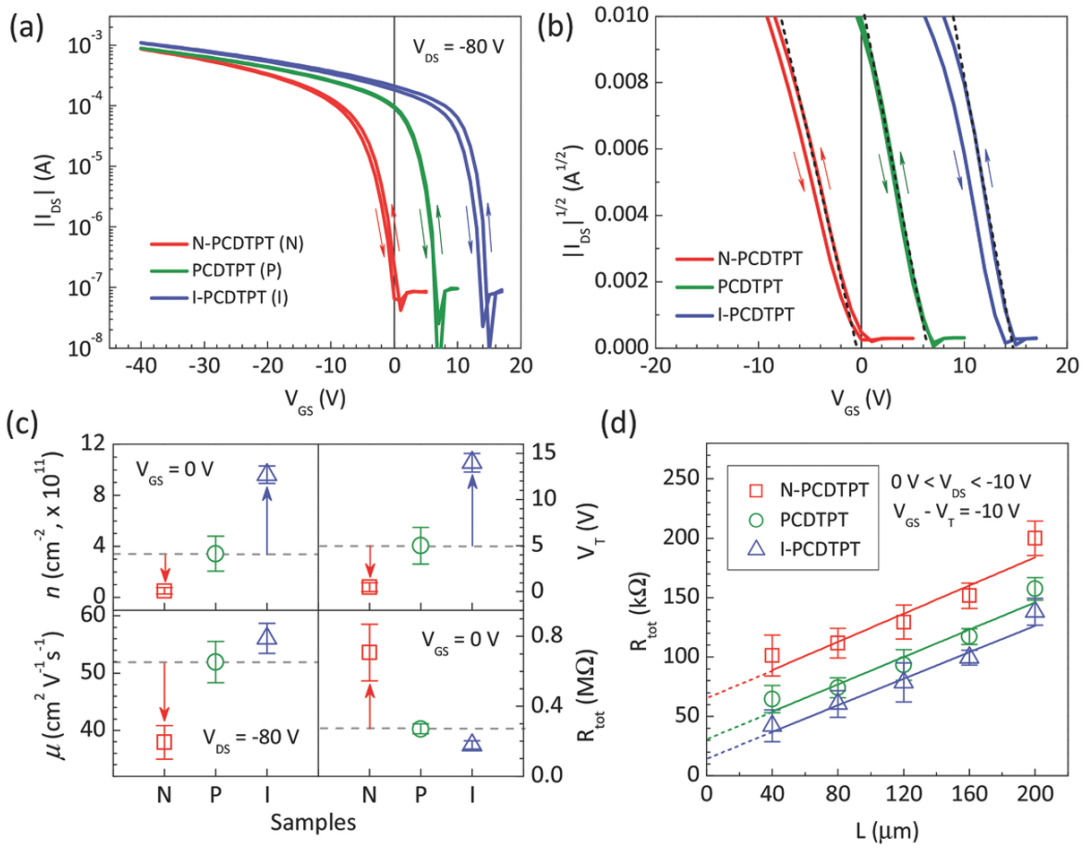

Fig. 1.5: Doping-induced charge density modulation in polymer OFETs, and it's effect on **(a,b)** transfer characteristics, **(c)** device mobility, and **(d)** device resistance (i.e. contact + channel). *Reproduced with permission from [33]. Copyright 2015 Wiley-VCH Verlag GmbH.*

is not as straight forward, due to the lower dielectric constant in organic materials [32]. The strong coulomb interactions does not mean that the transferred charge is necessarily free. Hence, the choice of both the host and dopant molecules is crucial for efficient charge transfer.

Lee *et al.* [33] reported on doping induced carrier density modulation in OFETs. Their investigation were conducted on bottom-gate bottom-contact transistors incorporating the p-type regioregular polymer PCDTPT as the active material. In a previous publication they demonstrated OFETs with an average mobility of 51.9 cm^2/Vs [34]. Such a high mobility was attributed to the applied fabrication procedure, resulting in highly ordered crystalline nanostructures. Nevertheless, measured threshold voltages of +7 V indicated the presence of trapped holes in the channel (see Fig. 1.5(a,b)). To rectify this issue, devices were treated to chemical vapor from ammonia (NH_3) for charge compensation. This led to a decrease in charge density (at zero gate bias), a shift in the threshold voltage to 0 V, and a recorded mobility of 37.9 cm^2/Vs respectively (see Fig. 1.5(c)). This was followed by intentional doping with iodine (I_2) vapor and thermal annealing. Final OFET performance parameters included an increase of the mobility up to 56.1 cm^2/Vs (i.e. higher than that of pristine devices), and a shift in threshold voltage to +14 V. Even-more, doped devices exhibited small hysteresis, lowest device resistances (i.e. contact and channel, see Fig. 1.5(d)), and no observed kinks in the transfer characteristics. These results demonstrate how doping can be

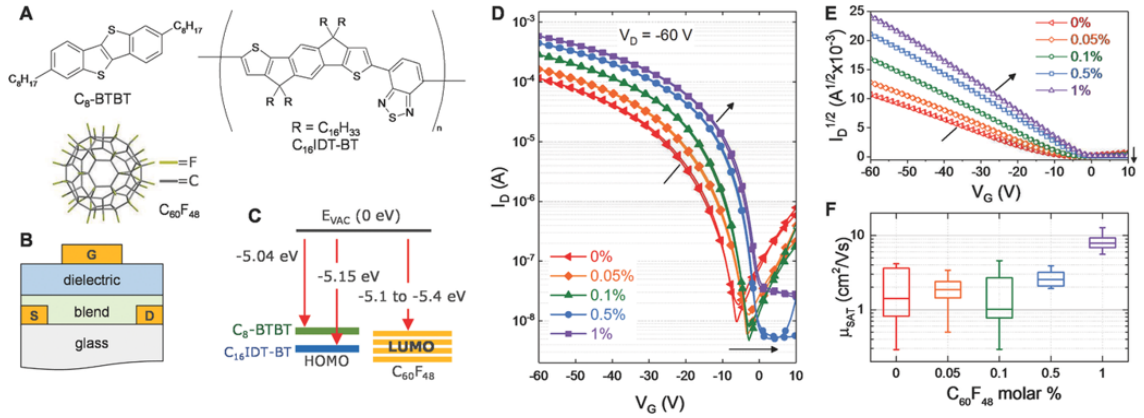

Fig. 1.6: (a) Molecular structures of the small molecule-polymer (C_8-BTBT/C_{16}IDT-BT) blend based materials, and the molecular dopant ($C_{60}F_{48}$). **(b,c)** Schematic of a top gate-bottom contact (TG-BC) OFET, and the energy levels. **(d,e)** Transfer characteristics in both logarithmic and linear (i.e. $\sqrt{I_d}$) scales for different doping concentrations. Shown here in molar weight %. **(f)** Impact of the doping on device mobilities. *Reproduced with permission from [38]. Copyright 2018 Wiley-VCH Verlag GmbH.*

used as a mechanism to realize high performance OFETs.

1.2.3 Blend based OFETs

Small molecules have been shown to exhibit high charge mobility, due to their crystalline features. Yet they are fabricated from vapor deposition. Conversely, polymers are fabricated from solution processes, which is regarded as a much easier and cheaper procedure. But due to their higher degree of disorder, they suffer from low mobilities. This led the to the proposition of blend based OFETs, that is to combine the best of both worlds. The high mobility of small molecules, and the easier processability of polymers. The effect of the polymer is to make the small molecule soluble for subsequent deposition from solution processes. Following the blend deposition, a vertical phase separation occurs, where the small molecule is located on the bottom with crystalline domains, and the polymer on top [35]. Varying processing parameters can also lead to lateral phase separation [36], and even trilayer separation [37].

In 2015, Niazi *et al.* [39] fabricated bottom-gate bottom-contact devices with small molecule/polymer blends of TIPS-pentacene and polystyrene. These devices recorded mobilities up to 6.7 cm^2/Vs, with threshold voltages and subthreshold swings as low as $+1$ V and 0.5 V/dec respectively. This new idea of device/material processing was pushed even further by adding a third component, creating so-called ternary blends. The third component here being a dopant. Paterson *et al.* [38] showed by adding a molecular dopant $C_{60}F_{48}$, into a blend of C_8-BTBT (small molecule) and C_{16}IDT-BT (polymer), mobilities of 13 cm^2/Vs were achieved (see Fig. 1.6). These mobilities were higher than that of OFETs based on the single materials, and even more so the undoped blend.

Other reports on blend based OFETs in the literature can be found here [40, 41, 42, 43, 44]. Not much is present to date, but with the early promise blends have shown, more interest will certainly focus on that front.

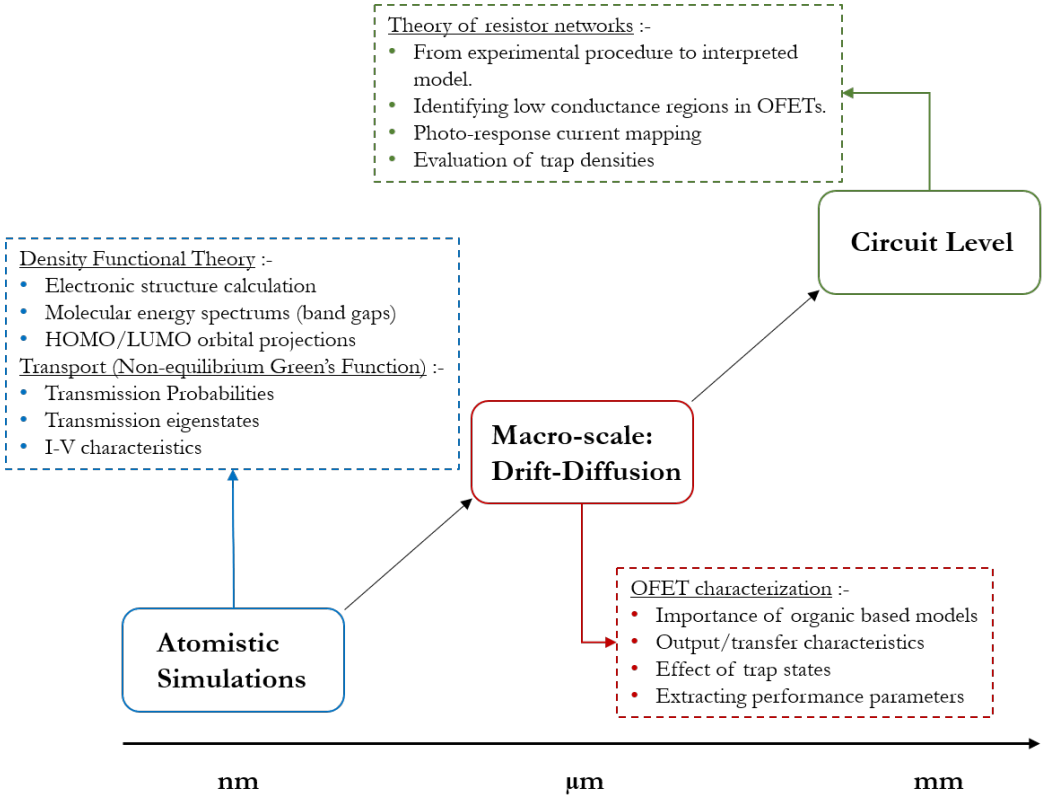

Fig. 1.7: Process flow of the theoretical approach presented and applied in this work. Investigating charge transport in organic based devices arcoss the entire dimension scale. A proposed approach as a basis towards full multi-scale implementation.

1.3 Motivation: the need for a theoretical approach

The discussion outlined in Sec. 1.2, provided a small overview on the progress in organic based devices, focusing specifically on OFETs. In reality, the literature is full of an immense amount of reports and demonstrations showcasing the efforts of the research community towards realizing high performance OFETs. All the while, retaining flexible properties, and using low cost fabrication techniques. The need (or want) to achieve lower device dimensions, coupled with the clear difference in the nature of charge transport in organic semiconductors, the knowledge shifted (as a requirement) from mainly device engineering to that of a multi-disciplinary one. This included engineering, material science, as well as chemistry. Furthermore, despite the important steps taken in understanding charge transport in organics, the exact nature is yet to be clear, and the experimental work has been guided mostly by a trial and error analysis.

There are still a number questions that are rather difficult to answer through experimental procedures alone. Presented experimental results are often limited by the accuracy of the measurement technique, and/or the device dimension. For example, it is well documented that improved charge transport occurs when organic semiconductors exhibit high degree of crystallinity (implying minimal structural and/or energetic disorder). This is obvious, but how to charges exactly flow at the atomistic level between individual molecules that are assumed to be

closely packed together? Is there a favoured directionality in transport? Another example revolves around charge mobilites in OFETs. The mobility is regarded as the most important parameter needed to characterize OFETs. The complexity in extracting accurate device mobilities, arises from it's dependence on several factors such as the temperature, electric field, and charge density. The latter affected further by charge trapping. Yet with many factors to take into consideration, device mobilites are usually extracted from the transfer characteristics. On the subject of traps, there has been proposed methods to identify local defective regions in organic films, and their subsequent effect on the output currents. This provides an excellent qualitative picture, but simultaneously unable to expand further by providing trap denisites (in terms of quantity) at these defective regions.

The intention here, is not implying that theoretical (i.e. simulation) approaches should be regarded as the main tools for an investigation. Rather, to highlight the areas where it could assist experimental studies to gain a complete understanding of how something behaves. The aforementioned examples basically outlined the specific theoretical work presented here, and is further illustrated in Fig. 1.7. This involves carrying out investigations across the entire dimension scale. Starting on atomistic (nanometer) scale, up to the circuit level. Moreover, this work could act as a foundation towards a multi-scale approach, whereby investigations on a certain dimension relies on outputs from the results obtained on the previous dimension. This approach is used here to a certain extent, but a full implementation across all dimensions is definitely possible.

1.4 Outline

This thesis is organized as follows:

Chapter 2 provides an introduction to the different methodologies applied in this work. Density functional theory (DFT) and the non-equilibrium Green's function (NEGF) are used to investigate electronic structure and charge transport on the atomistic/molecular level. The drift-diffusion (DD) model within the finite element method (FEM) is applied for the electrical characterization of OFETs.

In Chapter 3, organic molecules used as the active material for self-assembled monolayer FETs (SAMFETs), are the subject of a first principle investigation using DFT and NEGF. Electronic structures in both gas phase, and on substrate are compared. This is followed by charge transport analysis through these SAM-forming molecules.

In Chapter 4, the DD model is applied to characterize OFETs, extracting important performance measures. The investigation also focuses on the importance of a correct description of the sub-models used within DD, such as the density of states, the mobility model, and the trap model.

Chapter 5 provides an introduction to the circuit level model applied to identify low conductance regions in organic thin films. These regions are highlighted by extracting appropriate colormaps of the evaluated photo-current. The model is initially validated, then compared to experimental measurements. This chapter also highlights how a multiscale approach can be applied utilizing the different models presented here.

Chapter 6 summarizes the results presented in this thesis, and provides an outlook on future research directions.

Chapter 2

Methodology

This chapter provides a detailed discussion of the different theoretical methods applied in this work. From a quantum mechanical perspective, knowledge about electronic structures is achieved by solving the Schrödinger equation, which is near impossible for large systems. Hence, certain approaches are taken to simplify this task. Sec. 2.1 presents the different approximations leading the widely known and used method of density functional theory (DFT). This is followed by the theory of charge transport on the atomistic scale. More specifically, the Landauer formalism of electronic transport within the non equilibrium Green's function (NEGF) method (discussed in Sec. 2.2). Both DFT and NEGF methods are applied for the investigation carried out and presented in chapter 3.

In Sec. 2.3, the finite element method (FEM) and the drift-diffusion model (DD) are introduced. Both FEM and DD are used towards the generation of multidimensional structures for which a set of equations are solved, to understand and quantify any physical phenomena. These techniques are applied towards the simulation and characterization of OFETs on the macro-scale (discussed in chapter 4).

2.1 Electronic structure and NEGF theories

The first step in studying molecular structures, is finding the atomic arrangements corresponding to the the lowest total energy, and hence the most stable state. In doing so, one must solve the non-relativistic time independent Schrödinger equation expressed as

$$\hat{H}\Psi(\{R_A\},\{r_i,s_i\}) = E\Psi(\{R_A\},\{r_i,s_i\}), \tag{2.1}$$

For a system consisting of M nuclei and N electrons, the many body wavefunction Ψ is given in terms of all spatial coordinates of nuclei (R_A, where $A = 1,2,3,...,M$), and spatial and spin coordinates of electrons (r_i, s_i, where $i = 1,2,3,...,N$). The Hamiltonian $\hat{H}$ is the sum of all possible interactions between nuclei and electrons given by

$$\hat{H} = -\sum_{i=1}^{N}\frac{1}{2}\nabla_i^2 - \sum_{A=1}^{M}\frac{1}{2M_A}\nabla_A^2 + \sum_{i=1}^{N}\sum_{j>i}^{N}\frac{1}{|r_i - r_j|} + \sum_{A=1}^{M}\sum_{B>A}^{M}\frac{Z_A Z_B}{R_A - R_B|} - \sum_{i=1}^{N}\sum_{A=1}^{M}\frac{Z_A}{|r_i - R_A|}. \tag{2.2}$$

In Eq. (2.2), M_A is the ratio of the mass of nucleus A to the mass of an electron, Z_A the atomic number of nucleus A, and ∇_i^2 and ∇_A^2 the Laplacian operators respectively. The first and second terms in Eq. (2.2) are the kinetic energies of all electrons and nuclei, with the third and fourth terms representing the coulomb repulsion between electrons and nuclei. Lastly, the fifth term describes the coulomb attraction between electrons and nuclei[1]. Eventhough Eq. (2.2) is easy to

[1]Atomic units are employed throughout. Electronic charge e, it's mass m_e, and Planck's constant are all unity. Energies are given in Hartree (i.e. $1\,\mathrm{H} = 27.2\,\mathrm{eV}$), and all distances are given in Bohr radii (i.e. $a_0 = 0.529\,\text{Å}$)

understand, it is very complex to solve. Therefore, several approximations have been introduced to reduce this complexity.

2.1.1 Born-Oppenheimer approximation

The Born-Oppenheimer (BO) approximation [45] plays an important role in electronic structure calculations. It is based on the fact that mass of nuclei are much heavier than that of electrons. As nuclei move much slower than electrons, this realization allows the dynamics of both particles to be separated. Nuclei are treated as fixed particles with electrons moving around them. Within the BO approximation the second term in Eq. (2.2) can be neglected, and the fourth term becomes a constant having no affect on the wavefunction, rather simply shifts the total energy of a system. Eq. (2.2) then becomes

$$\hat{H} = -\sum_{i=1}^{N} \frac{1}{2}\nabla_i^2 + \sum_{i=1}^{N}\sum_{j>i}^{N} \frac{1}{|r_i - r_j|} - \sum_{i=1}^{N}\sum_{A=1}^{M} \frac{Z_A}{|r_i - R_A|} \tag{2.3a}$$

$$\hat{H}_{elec}\Psi_{elec}(\{x_i\}) = E_{elec}\Psi_{elec}(\{x_i\}) \tag{2.3b}$$

Eqs. (2.3a)-(2.3b) are called the *electronic* Hamiltonian and Schrödinger equations. For simplicity, both r_i and s_i are described by the variable x_i. The total energy is the sum of the electronic energy E_{elec} and the constant value of the nuclear repulsion.

$$E_{tot} = E_{elec} + \sum_{A=1}^{M}\sum_{B>A}^{M} \frac{Z_A Z_B}{|R_A - R_B|} \tag{2.4}$$

However, it is important to note that the BO approximation is not universally valid, and will breakdown in the presence of multiple energy surfaces close to each other. This gives a rise to electronic and vibrational interactions that cannot be neglected. Dissociative adsorption of molecules on metal surfaces is one example, hence more caution should be taken when dealing with such systems [46, 47, 48, 49].

2.1.2 Hartree-Fock approximation

From the BO approximaiton, the complexity of the Schrödinger equation was reduced. But there still lies a major difficulty in solving Eq. (2.3b), referring to the interactions between electrons responsible for the quantum effects that needs to be understood. A system that requires a treatment of 4^N variable (i.e. spatial and spin coordinates of electrons) is difficult to solve. The introduction of the Hartree-Fock [50, 51] approximation aims to further simplify this issue. The HF approximation is based on molecular orbital theory, and posits that each electron's motion can be described by a single-particle function which does not depend explicitly on the instantaneous motion of other electrons. In other words, it maps the N-electron problem into a one electron Schrödinger-like equation.

In HF, the wavefunciton is described by a single Slater determinant. The key essence of this determinant, is that it obeys the Pauli exclusion principle. Electrons are fermions, and if two sets of electron coordinates are exchanged, their wavefunctions must be anti-symmetric.

$$\Psi(x_1, ..., x_i, ..., x_j, ..., x_N) = -\Psi(x_1, ..., x_j, ..., x_i, ..., x_N) \tag{2.5}$$

To realize this anti-symmetry, consider the following two electron example:

$$\Psi(x_1, x_2) = \frac{1}{\sqrt{2}} \begin{vmatrix} \chi_1(x_1) & \chi_2(x_1) \\ \chi_1(x_2) & \chi_2(x_2) \end{vmatrix} \tag{2.6}$$

Expanding Eq. (2.6) gives,

$$\Psi(x_1, x_2) = \frac{1}{\sqrt{2}} \left[\chi_1(x_1)\chi_2(x_2) - \chi_2(x_1)\chi_1(x_2)\right] = -\Psi(x_2, x_1) \tag{2.7}$$

Hence, a general representation of the Slater determinant in the HF approximation can be written in the form,

$$\Psi^{HF}(x_i, x_j, ..., x_N) = \frac{1}{\sqrt{N!}} \begin{vmatrix} \chi_i(x_i) & \chi_j(x_i) & \dots & \chi_N(x_i) \\ \chi_i(x_j) & \chi_j(x_j) & \dots & \chi_N(x_j) \\ \vdots & \vdots & \ddots & \vdots \\ \chi_i(x_N) & \chi_j(x_N) & \dots & \chi_N(x_N) \end{vmatrix} \tag{2.8}$$

where the rows denote the electrons, and the coloumns denote the spin orbitals. Although using a single Slater determinant is a good description of the wavefunction, it is not enough to comupute the "exact" solution of the Schrödinger equation as it requires several determinants to be employed. With the form of the approximate wavefunction now known, the HF energy for a given system is expressed as follows,

$$\begin{aligned} E^{HF} &= \langle \Psi^{HF} | H_{elec} | \Psi^{HF} \rangle \\ &= \sum_{i=1}^{N} \int \chi_i^*(x_i) \Big[-\frac{\nabla_i^2}{2} + \frac{Z_A}{r_{iA}} \Big] \chi_i(x_i) dx_i \\ &+ \frac{1}{2} \sum_{i=1}^{N} \sum_{j=1}^{N} \iint \chi_i^*(x_i) \chi_j^*(x_j) \frac{1}{|r_i - r_j|} \chi_i(x_i) \chi_j(x_j) dx_i dx_j \\ &- \frac{1}{2} \sum_{i=1}^{N} \sum_{j=1}^{N} \iint \chi_i^*(x_i) \chi_j^*(x_j) \frac{1}{|r_i - r_j|} \chi_j(x_i) \chi_i(x_j) dx_i dx_j \end{aligned} \tag{2.9}$$

Minimizing the energy E^{HF} is achieved by using the "best" approximate wavefunction[2]. This is obtained employing the variation principle, which states that the orbitals can be varied while maintaining the constraint that they orthonormal (i.e $\langle \chi_i(x_i) | \chi_j(x_j) \rangle = \delta_{ij}$). From Eq. (2.9), the first term,

$$\sum_{i=1}^{N} \int \chi_i^*(x_i) \Big[-\frac{\nabla_i^2}{2} + \frac{Z_A}{r_{iA}} \Big] \chi_i(x_i) dx_i = \langle \chi_i(x_i) | h(x_i) | \chi_i(x_i) \rangle \tag{2.10}$$

represents the kinetic energy and the potential energy for the attraction between an electron and the nuclei, where $h(x_i)$ is referred to as the one electron operator. The second term describes the coulomb interaction between two electrons,

$$\frac{1}{2} \sum_{i=1}^{N} \sum_{j=1}^{N} \iint \chi_i^*(x_i) \chi_j^*(x_j) \frac{1}{|r_i - r_j|} \chi_i(x_i) \chi_j(x_j) dx_i dx_j = \langle \chi_i(x_i) | \mathcal{J}_j(x_i) | \chi_i(x_i) \rangle \tag{2.11}$$

[2]Given a single Slater determinant

where the $\mathcal{J}_j(x_i)$ is defined as the Coulomb operator. The last term does not have a simple classical analogy. It arises from the anti-symmetric requirement of the wavefunction. It looks similar to the Coulomb term, except the orbitals χ_i and χ_j are exchanged. Hence,

$$\frac{1}{2}\sum_{i=1}^{N}\sum_{j=1}^{N}\iint \chi_i^*(x_i)\chi_j^*(x_j)\frac{1}{|r_i - r_j|}\chi_j(x_i)\chi_i(x_j)dx_i dx_j = \langle\chi_i(x_i)|\mathcal{K}_j(x_i)|\chi_i(x_i)\rangle \tag{2.12}$$

where $\mathcal{K}_j(x_i)$ is the exchange operator. Within the HF approximation, Eqs. (2.9)-(2.12) can be used to write the one electron Schrödinger-like equation in a more compact form.

$$\hat{F}_i\chi_i(x_i) = \epsilon_i\chi_i(x_i), \;\; \hat{F}_i = -\frac{\nabla_i^2}{2} + V_{Attraction} + V_{Repulsion} + V_{Exchange} \tag{2.13}$$

Eq. (2.13) is an eigenvalue equation, where $\hat{F}_i$ is known as the Fock operator. $\hat{F}_i$ combines all of the attraction, repulsion and exchange potentials described above. The Fock operator has a functional dependence on the orbitals, therefore it needs to be solved in an iterative fashion. An initial guess for the orbitals is made, the Fock operator is constructed and Eq. (2.13) is solved to obtain the energy and a new set of orbitals. This process is repeated until self-consistency is reached.

2.1.3 Basis sets

Carrying out a successful self-consistent procedure of Eq. (2.13), and subsequently minimizing the energy relies on the description of the *molecular* orbitals. Molecular orbitals are unknown functions, yet they can be represented with a linear combination of *atomic* orbitals which are known functions, and referred to as "basis sets". The larger the basis set is, the more accurate the description of a molecular orbital. At the very bottom are the so called minimal basis sets. For example, minimal basis sets for elements in the first row of the periodic table (e.g. H or He) consists of one s-fuction. For the second row (e.g. Li, Be, B, C, etc.) the minimal basis sets consist of two s-functions (1s, 2s) and one p-function ($2p_x$, $2p_y$, $2p_z$). These minimal basis sets are called single-zeta (SZ) basis sets. Naturally adding more functions improves the molecular orbital description. For the second row, a double-zeta (DZ) basis set consists of four s-fucntions (1s, 1s', 2s, 2s') and two p-functions ($2p_x$, $2p_y$, $2p_z$, $2p_x$',$2p_y$',$2p_z$'). In a similar fashion there are triple-zeta (TZ) and so forth.

Basis sets can also be introduced in a split-valence approach. This approach separates the core from the valence atomic orbitals. Single functions are applied for the core orbitals, and multiple functions for the valence orbitals respectively. The reasoning behind core and valence orbital splitting, is that the former is relatively independent of the chemical environment and might not require a large degree of flexibility in terms of description. The latter on the other hand, participates in a wide range of chemical reactions and requires a much more accurate description. Fig. 2.1 illustrates the difference between a normal and split valence basis sets for a Beryllium atom. Further improvements can be applied for a better description of the molecular orbitals. A shape of an orbital in a free isolated atom is different to that of an atom within a chemical environment. In the latter case, orbitals become distorted from their original atomic shape. This distortion can be accounted for by adding polarization functions to a particular basis set. An orbital with angular momentum l can be polarized by adding another orbital with an angular momentum of $l + 1$. For example, a double-zeta basis set would then appropriately termed a double-zeta polarized basis set (DZP). Over the years, a large amount of basis sets have been proposed. Famous examples include the Pople-style [52, 53] and Dunning-style basis

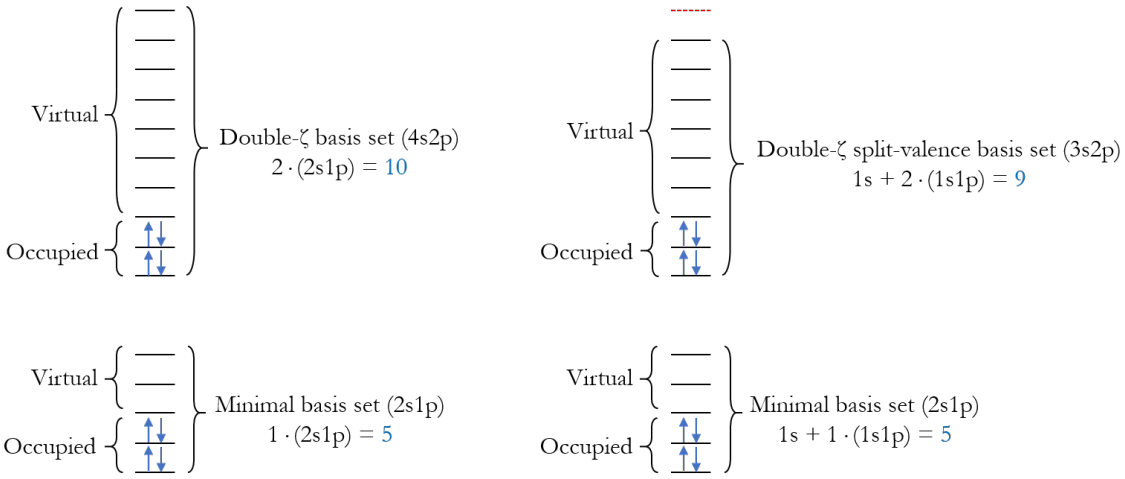

Fig. 2.1: The difference between a normal and split-valence basis set for a Beryllium atom. The first two basis levels are illustrated. The orbital level highlighted in *red* refers to the orbital not required for the basis set description. For a triple-ζ basis set, the normal would include *15* orbitals, while the split-valence would include *13* and so forth.

sets [54, 55, 56]. One can try different types or further increase the size of these sets. Increasing basis set size will eventually result in reaching the complete basis set (CBS) limit. At this point, the introduced basis sets comes at a high computational cost without further improvement in energy minimization. Choosing the right basis set depends mainly on the system at hand, and a compromise between level of accuracy and computational power.

2.1.4 Density functional theory

Density functional theory (DFT) presented a huge leap in computing the electronic structure of molecular and condensed matter. Despite the fact that HF (which is a wavefunction based method) is a good approach, the idea of dealing with 4^N variables was becoming increasingly difficult, especially for large systems. DFT differs from HF rather by taking into consideration the density as the main quantity. This simplifies the electronic structure problem to a great extent. Regardless of how many electrons are in a system, the density will always be three dimensional. This is the reason why DFT is presently the most successful and well established approach being used in studying molecular systems.

2.1.4.1 Thomas-Fermi model

The first approach towards computing the electronic structure in terms of the density, was taken by Llewellyn Thomas and Enrico Fermi in 1972 [57, 58]. The electron density is defined as the integral the spin coordinates of all electrons, and all but one of the spatial coordinates.

$$\rho(r) = N \int ... \int |\Psi(x_1, x_2, ..., x_N)|^2 ds_1 dx_2 ... dx_N \tag{2.14}$$

$\rho(r)$ determines the probability of finding N electrons within a volume r. It is a non-negative function of the three spatial variables which vanishes at infinity, and integrates to the total number of electrons.

$$\rho(r \to \infty) = 0, \;\; N = \int \rho(r) dr \tag{2.15}$$

Based on the uniform electron gas, they proposed the following functional for the kinetic energy.

$$T^{TF}[\rho(r)] = \frac{3}{10}(3\pi^2)^{\frac{2}{3}} \int \rho^{\frac{5}{3}}(r) dr \tag{2.16}$$

Adding the treatments of the electron-nuclear attraction and electron-electron repulsion, the energy functional is expressed as

$$E^{TF}[\rho(r)] = \frac{3}{10}(3\pi^2)^{\frac{2}{3}} \int \rho^{\frac{5}{3}}(r) dr - Z \int \frac{\rho(r)}{r} dr + \frac{1}{2} \iint \frac{\rho(r_1)\rho(r_2)}{r_{12}} dr_1 dr_2 \tag{2.17}$$

The significance of the Thomas-Fermi model was not how accurately it describes the energy, but the fact that is was derived using the electron density.

2.1.4.2 Hohenberg-Kohn Theorems

Much of what DFT is based on relies on the two theorems, Pierre Hohenberg and Walter Kohn outlined in 1964 [59].

1. The first theorem:
   - It states that an external potential $V_{ext}(r)$ is a unique functional of the electron density. Let us assume that there were two external potentials $V_{ext}(r)$ and $V'_{ext}(r)$ differing by more than a constant, and giving the same electron density for the ground state. This provides two Hamiltonians $\hat{H}$ and $\hat{H}'$ whose ground state densities were the same, although the normalized wavefunctions Ψ and Ψ' would be different. Taking Ψ' as a trial wavefunction for the Hailtonian $\hat{H}$ problem gives,

$$\begin{aligned} E_0 < \langle \Psi' | \hat{H} | \Psi' \rangle &= \langle \Psi' | \hat{H}' | \Psi' \rangle + \langle \Psi' | \hat{H} - \hat{H}' | \Psi' \rangle \\ &= E'_0 + \int \rho(r)[V_{ext}(r) - V'_{ext}(r)] dr \end{aligned} \tag{2.18}$$

     where E_0 and E'_0 are the ground state energies for $\hat{H}$ and $\hat{H}'$ respectively. Similarly, taking Ψ as a trial wavefunction for the Hamiltonian $\hat{H}'$ problem,

$$\begin{aligned} E'_0 < \langle \Psi | \hat{H}' | \Psi \rangle &= \langle \Psi | \hat{H} | \Psi \rangle + \langle \Psi | \hat{H}' - \hat{H} | \Psi \rangle \\ &= E_0 + \int \rho(r)[V_{ext}(r) - V'_{ext}(r)] dr \end{aligned} \tag{2.19}$$

     Adding Eqs. (2.18)-(2.19) results in,

$$E_0 + E'_0 < E'_0 + E_0 \tag{2.20}$$

     Eq. (2.20) is a contradiction, and so there cannot be two different potentials that would give the same electron density for the ground state. This is the proof that $\rho(r)$ uniquely determines the number of electrons N and the potential $V_{ext}(r)$. Hence, the total energy is expressed as

$$\begin{aligned} E[\rho(r)] &= T[\rho(r)] + E_{en}[\rho(r)] + E_{ee}[\rho(r)] \\ &= \int \rho(r) V_{ext}(r) dr + F_{HK}[\rho(r)] \end{aligned} \tag{2.21}$$

where,

$$F_{HK}[\rho(r)] = T[\rho(r)] + E_{ee}[\rho(r)] \tag{2.22}$$

Eqs. (2.21)-(2.22) are solely dependent on the density making them universal funciton-als. This applies equally to small atoms and large molecules alike.

2. The second theorem
   - It states that the functional $F_{HK}[\rho(r)]$ delivers the lowest energy *if and only if* the input density is the true ground state density. This is simply implying the use of the variation principle. In other words, this means that for a trial density, which satisfies the necessary conditions (i.e. $\tilde{\rho}(r) > 0$ and $N = \int \tilde{\rho}(r)dr$)) and is associated with some external potential, the result is the upper bound of the true ground state energy.

2.1.4.3 Kohn-Sham Equations

Granted, from the Hohenberg-Kohn theorems, it was proved that the total energy can be obtained from the ground state density. Yet there was still a problem as to how the density is described. Adding to that, the explicit form of the functional $F_{HK}[\rho(r)]$ required further elaborations. This was achieved by Walter Kohn and Lu Jeu Sham in 1965 [60]. The first step is that they realized the incomplete description of the kinetic energy according to the Thomas-Fermi model, that it did not employ orbitals. They suggested that if the electrons are "non-interacting" in the HF sense, then one can just use the HF expression for the kinetic energy incorporating orbital. It is then written in the following form

$$T_s[\rho(r)] = \sum_i^N \left\langle \chi_i \middle| -\frac{1}{2}\nabla^2 \middle| \chi_i \right\rangle \tag{2.23}$$

where the electron density is expressed in terms of the orbital as,

$$\rho(r) = \sum_i^N \sum_s |\chi_i(r,s)|^2 \tag{2.24}$$

As for the second term of the functional $F_{HK}[\rho(r)]$, the electron-electron interactions E_{ee} consist of both the repulsion (classical part) and exchange (non-classical part) terms. Hence,

$$\begin{aligned} E_{ee}[\rho(r)] &= \frac{1}{2}\iint \frac{\rho(r_1)\rho(r_2)}{r_1 - r_2} dr_1 dr_2 + E_{Exchange}[\rho(r)] \\ &= \mathcal{J}[\rho(r)] + E_{Exchange}[\rho(r)] \end{aligned} \tag{2.25}$$

Kohn and Sham further stated that the kinetic energy from Eq. (2.23) is not the true energy, due to a correlation between electrons that must be accounted for. Under this consideration the functional $F_{HK}[\rho(r)]$ becomes

$$F_{HK}[\rho(r)] = T_s[\rho(r)] + \mathcal{J}[\rho(r)] + E_{xc}[\rho(r)] \tag{2.26}$$

where the $E_{xc}[\rho(r)]$ is called the exchange-correlation functional,

$$E_{xc}[\rho(r)] = (T[\rho(r)] - T_s[\rho(r)]) + (E_{ee}[\rho(r)] - \mathcal{J}[\rho(r)]) \tag{2.27}$$

Combining Eqs. (2.21)-(2.27) yields the following expression for the energy,

$$
\begin{aligned}
E[\rho(r)] = &\sum_{i}^{N} \left\langle \chi_i \right| -\frac{1}{2}\nabla^2 \left| \chi_i \right\rangle \\
&- \sum_{i}^{N} \int \sum_{A}^{M} \frac{Z_A}{|r_1 - R_A|} |\chi_i(r_1)|^2 dr_1 \\
&+ \frac{1}{2} \sum_{i}^{N} \sum_{j}^{N} \iint |\chi_i(r_1)|^2 \frac{1}{r_1 - r_2} |\chi_j(r_2)|^2 dr_1 dr_2 \\
&+ E_{xc}[\rho(r)]
\end{aligned} \tag{2.28}
$$

The only term to which no explicit form is given, is the $E_{xc}[\rho(r)]$. The variation principle is applied to minimize the energy under the usual constraint (i.e $\langle \chi_i(x_i) | \chi_j(x_j) \rangle = \delta_{ij}$). The result is the central equation in Kohn-Sham DFT, which is a one-electron Schrödinger-like expression,

$$
(-\frac{1}{2}\nabla^2 + V_{eff})\chi_i = \epsilon \chi_i \tag{2.29a}
$$

$$
V_{eff} = V_{ext} + V_{rep} + V_{xc} \tag{2.29b}
$$

where χ_i are the Kohn-Sham orbitals, and V_{eff} combines all potentials acting on the system (i.e. external, replusion, and exchange). Eq. (2.29a) is solved iteratively, with an initial guess of the electron density to construct V_{eff} and provide the Kohn-Sham orbital. A new density is obtained, and the process repeated until convergence is reached.

2.1.4.4 Exchange Correlation

The difference between various DFT methods, is the choice of the functional form for the exchange-correlation energy. Yet an explicit functional form of this potential has been elusive so far. For this reason, a lot of different approximations have been proposed with different levels of accuracy, and computational complexity to approximate it. When expressing this functional in a written form the exchange and correlation terms are separated and given by,

$$
E_{xc}[\rho(r)] = E_x[\rho(r)] + E_c[\rho(r)] = \int \rho(r)\epsilon_x[\rho(r)]dr + \int \rho(r)\epsilon_c[\rho(r)]dr \tag{2.30}
$$

where ϵ_x (exchange) and ϵ_c (correlation) are the energies per particle respectively. J. P. Perdew and K. Schmidt were credited for grouping the different flavors of the exchange-correlation functionals in what is referred to as "Jacob's Ladder" [61]. At the bottom is the Hartree-Fock theory, and moving upwards one would expect an improvement in the accuracy for each higher step. Only the first two steps will be briefly discussed to give a perspective on the role of this functional in DFT.

Local Density Approximation (LDA), is the simplest approximation for the exchange-correlation functional. At the center of this model is the idea of uniform electron gas. A system is divided up in equal infinitesimal portions with the same density. By applying the uniform electron gas results on each portion and summing up over all space, results in the exchange energy. The exchange energy for LDA is given by the analytical expression,

$$
E_x^{LDA}[\rho(r)] = -\frac{3}{4}\left(\frac{3}{\pi}\right)^{1/3} \int \rho^{4/3}(r)dr \tag{2.31}
$$

The correlation energy is more complicated and generally obtained by fitting to the many-body studies of Gell-Man/Brueckner [62] and Ceperly/Alder [63]. The Perdew-Zunger (PZ) [64],

Perdew-Wang (PW) [65] and Vosko-Wilk-Nusair (VWN) [66] functionals are all common LDA functionals. LDA is applicable to systems with slowly varying densities, but it does not apply for highly inhomogeneous systems such as molecules. In such complex systems, it tends to underestimate the exchange and overestimate the correlation. Studies showed binding energies were overestimated by 15%-20%, while lattice constants were underestimated by 2%-3% for metals and insulators [67, 68, 69]. Due to these inconsistencies, more accurate approximations were required.

Improvements over the LDA approach consider a non-uniform electron gas. Generalized Gradient Approximations (GGA) take a step in that direction. In GGAs, the exchange and correlation energies are both dependent on the electron density, and the derivatives of the density. It gives the value of the density a specific location, and the direction for which it is changing with respect to that location. This led to GGA yielding better results with respect to geometries and ground state energies for molecules and solids. The form of the exchange energy in GGAs is given by,

$$E_x^{GGA}[\rho(r)] = \int \rho(r)\epsilon_x(\rho(r))F_{GGA}dr \tag{2.32}$$

From Eq. (2.32), $F_{GGA}(x)$ represents a correction in the description of the exchange energy compared to LDA for a given density, with x being a dimensionless gradient variable.

$$x = \frac{|\nabla\rho(r)|}{2(3\pi^2)^{1/3}\rho(r)^{4/3}} \tag{2.33}$$

There are various exchange functionals including the very popular A. D. Becke (B88) [70] and Perdew-Burke-Ernzerhof (PBE) [71]. These functionals differ in the way they describe the correction term. If the variable x in Eq.(2.33) is equal to zero, the exchange energy reverts back to the LDA description. Therefore, GGA will always offer a better representation of the exchange energy. Furthermore, there are also several proposed functionals for the correlation energy, most notably the Perdew-Wang (PW86, PW91) [72, 73], and Lee-Yang-Parr (LYP) [74], of which all are based on fittings.

2.2 Electronic transport

2.2.1 The quantum of conductance

According to Ohm's law the conductance is described as,

$$G = \sigma\frac{A}{L} \tag{2.34}$$

where A is the area of the cross section of a conductor, L the length, and σ the conductivity respectively. From Ohm's law this means that the conductance should either vanish when the area is small, or infinitely large when the length is short. But that is not the case for atomic-size conductors because neither does the conductance vanishes, nor reaches infinity. An indication that Ohm's law must breakdown. There are three important characteristics that define the size of a conductor, when the macroscopic description is not applicable anymore [75] (1) the de Broglie wavelength relate to the kinetic energy of electrons, (2) the mean free path defined as the distance the electrons travel without changing momentum, and (3) the phase relaxation length defined as the distance electrons travel without altering their phase. Phase relaxation lengths are related to the inelastic scattering of the electron-electron and electron-phonon interactions. This contributed

to what is known as non-coherent transport. As the focus of the presented work (see chapter 3) is on coherent transport, phase relaxation regimes will not be discussed further.

In order to have a full understanding about the conductance in atomic-scale devices, a quantum mechanical treatment is required. Consider a single energy level (i.e. channel) device under a voltage bias located between two contacts with chemical potentials μ_1 and μ_2 respectively. One would argue that by coupling the channel strongly to the contacts, the conductance would continue to increase. But in reality, the conductance eventually reaches a maximum value. This is due to so-called level broadening, related to the density of states of both the channel and contacts [76]. Before coupling takes place, the channel is sharp and well defined. Once coupling is achieved, the channel loses that sharp definition, which is significant for the channel but has no influence on the contacts. As a consequence channel is broadened, and part of it will lie outside the window defined by the chemical potentials. This partial exclusion will not contribute to any charge flow, hence giving the proof of maximum conductance.

2.2.2 Landauer formalism (NEGF)

A simple picture was painted above regarding conductance from a quantum mechanical standpoint. Nevertheless, a question presents itself on how the electrons actually flow from one contact to the next though a given channel. To answer this question, the focus turns to the quantum mechanical formalism of electronic transport through one dimensional devices proposed by Rolf Landauer [77, 78]. Landauer suggested a relation between the conductance and the transmission probability of an electron to flow from one contact to another passing though certain available channels. At the point of equilibrium, both contacts are filled up with electrons up to the respective Fermi levels, that are aligned with each other perfectly. If a voltage is applied the Fermi levels start to shift and become separated from their equilibrium state by an amount of,

$$\mu_1 - \mu_2 = qV_D \tag{2.35}$$

where q is the electronic charge, and V_D the applied voltage respectively. This gives a rise to two different Fermi functions expressed as,

$$f_1(E) = \frac{1}{1 + \exp\left[(E - \mu_1)/k_b T\right]} \tag{2.36a}$$

$$f_2(E) = \frac{1}{1 + \exp\left[(E - \mu_2)/k_b T\right]} \tag{2.36b}$$

From this point, each contact will try to bring the channel into equilibrium with itself. One contact continues to inject electrons into the channel, while the other extracts them. As equilibrium is never achieved with either contact under the constant injection and extraction of electrons, this leads to current flow. All of this was already known to Landauer, but he further specified that there lies a finite probability for an electron to be transmitted. The current was expressed accordingly as,

$$I = \frac{2e}{h} \int_{-\infty}^{+\infty} T(E, V)[f_1(E) - f_2(E)]dE \tag{2.37}$$

where $T(E, V)$ represents the transmission probability and is dependent on both the energy and applied voltage. Furthermore, this probability can be expanded within the non-equilibrium Green's function (NEGF) method and rewitten as follows,

$$I = \frac{2e}{h}\int_{-\infty}^{+\infty} T(G_d^{\dagger}\Gamma_2 G_d \Gamma_1)[f_1(E) - f_2(E)]dE \tag{2.38}$$

hence achieving a connection between the Landauer formalism and DFT. The different terms listed in Eq. (2.38) will be briefly discussed, but the reader can find a complete and detailed derivations in Ref. [76].

The Hamiltonian and wavefunction of a system can be divided into three parts, $(H_1, |\Psi_1\rangle)$ for one contact, $(H_2, |\Psi_2\rangle)$ for the other contact, and $(H_d, |\Psi_d\rangle)$ for the device respectively.

$$\begin{pmatrix} H_1 & \tau_1 & 0 \\ \tau_1^{\dagger} & H_d & \tau_2^{\dagger} \\ 0 & \tau_2 & H_2 \end{pmatrix} \begin{pmatrix} |\Psi_1\rangle \\ |\Psi_d\rangle \\ |\Psi_2\rangle \end{pmatrix} = E \begin{pmatrix} |\Psi_1\rangle \\ |\Psi_d\rangle \\ |\Psi_2\rangle \end{pmatrix} \tag{2.39}$$

Where $\tau_{1,2}$ describe the interaction between the device and contacts. The Green's function (i.e. G_d and $G_d^{\dagger}$ in Eq. 2.38) is used in transport calculations and is defined by,

$$(E - H)G(E) = I \tag{2.40}$$

Furthermore, it gives a response of a system under a constant perturbation in the Schrödinger equation.

$$\begin{aligned} H|\Psi\rangle &= E|\Psi\rangle + |\nu\rangle \\ (E - H)|\Psi\rangle &= -|\nu\rangle \\ |\Psi\rangle &= -G(E)|\nu\rangle \end{aligned} \tag{2.41}$$

Using the Green's function makes it easier calculate the system properties than solving the whole eigenvalue problem. The example shown below solves for the wavefunction of the second contact $|\Psi_2\rangle$, given that the wavefunction of the device $|\Psi_d\rangle$ is known. Using the third row in Eq. (2.40) and the expansion in Eq. (2.41),

$$\begin{aligned} H_2|\Psi_2\rangle + \tau_2|\Psi_d\rangle &= E|\Psi_2\rangle \\ (E - H_2)|\Psi_2\rangle &= \tau_2|\Psi_d\rangle \\ |\Psi_2\rangle &= g_2(E)\tau_2|\Psi_d\rangle \end{aligned} \tag{2.42}$$

Note the difference between the uppercase G and the lowercase g. The former denotes the full Green's function and it's sub-matrices (i.e G_1, G_d, G_{1d}), while the latter refers to the Green's function of the isolated subsystem. Furthermore, a difference also exists between G and $G^{\dagger}$. The first corresponds to outgoing waves and referred to as the retarded Green's function. The second corresponds to incoming waves and is called the advanced Green's function.

Moreover, it is also possible to calculate the Green's function of the device (G_d) without the need to calculate the full Green function (G). Using the definition from Eq. (2.40)

$$\begin{pmatrix} E - H_1 & -\tau_1 & 0 \\ -\tau_1^{\dagger} & E - H_d & -\tau_2^{\dagger} \\ 0 & -\tau_2 & E - H_2 \end{pmatrix} \begin{pmatrix} G_1 & G_{1d} & G_{12} \\ G_{d1} & G_d & G_{d2} \\ G_{21} & G_{2d} & G_2 \end{pmatrix} = \begin{pmatrix} I & 0 & 0 \\ 0 & I & 0 \\ 0 & 0 & I \end{pmatrix} \tag{2.43}$$

To solve for G_d, the second coloumn is taken, resulting in

$$(E - H_1)G_{1d} - \tau_1 G_d = 0 \tag{2.44a}$$

$$-\tau_1^\dagger G_{1d} + (E - H_d)G_d - \tau_2^\dagger G_{2d} = I \tag{2.44b}$$

$$-\tau_2 G_d + (E - H_2)G_{2d} = 0 \tag{2.44c}$$

Solving Eqs. (2.44a)-(2.44c) yields

$$G_{1d} = g_1 \tau_1 G_d \tag{2.45a}$$

$$G_{2d} = g_2 \tau_2 G_d \tag{2.45b}$$

Substituting Eqs. (2.45a)-(2.45b) into Eq. (2.44b) gives,

$$G_d = (E - H_d - \Sigma_1 - \Sigma_2)^{-1}, \qquad \begin{cases} \Sigma_1 = \tau_1^\dagger g_1 \tau_1 \\ \Sigma_2 = \tau_2^\dagger g_2 \tau_2 \end{cases} \tag{2.46}$$

$\Sigma_{1,2}$ are called self-energies. They arise from the coupling between the device and contacts, triggering a redistribution of the states (i.e. transfer of electrons between both device and contact). The self energies consist of real and imaginary parts. The real part represents the shift in energy level of the device, due to the induced perturbation of the contacts. The imaginary part represents level broadening due to the same perturbation and is expressed as,

$$\Gamma_{1,2} = i(\Sigma_{1,2} - \Sigma_{1,2}^\dagger) = i\tau(g_{1,2} - g_{1,2}^\dagger)\tau^\dagger \tag{2.47}$$

To summarize the terms from Eq. (2.38), the Green's functions G_d and $G_d^\dagger$ solve for the wavefunctions of incoming and outgoing waves through the device, while Γ_1 and Γ_2 define the broadening. These terms complete the description of the transmission probability required to evaluate the currents under an applied within the Landauer formalism.

2.3 The drift-diffusion model

In this section, the drift-diffusion (DD) model, derivation, and application within the finite element method (FEM) is briefly presented. For a more comprehensive discussion on the DD model, the reader is referred to the excellent books written by Ansgar Jüngel [79] and Karl Hess [80].

The standard semi-classical transport theory within the DD model, is based on the Boltzmann equation

$$\frac{\partial f}{\partial t} + v \cdot \nabla_r f + \frac{eE}{\hbar} \cdot \nabla_k f = \sum_{k'} \Big(S(k',k) f(r,k',t)\big[1 - f(r,k,t)\big] - S(k,k') f(r,k,t)\big[1 - f(r,k',t)\big] \Big) \tag{2.48}$$

where r is the position, k the momentum, $f(r,k,t)$ the distribution function (i.e. occupation probability), v the group velocity, E the electric field, $S(k,k')$ is the transition (or scattering) rate

between momentum states k and k', and $[1 - f(k', t)]$ the probability that momentum state k' is not occupied. The main attribute of the Boltzmann equation, is that it takes into account short-range particle interactions. Such as collisions between particles or with the crystal lattice. This effectively means that the distribution function f infact changes with time, due to occurrence of events arsing from these interactions. The summation on the right hand side of Eq. (2.48) is the collision term, which accounts for all scattering events. The term on the left hand side, is the dependence of the distribution function on time, space (in relation to the velocity), and momentum (in relation to the electric field).

The collision term on the right hand side of Eq. (2.48) can be substituted with the term

$$\frac{f_{eq} - f(r, k, t)}{\tau} \tag{2.49}$$

where f_{eq} refers to the equilibrium distribution function, and τ is a microscopic relaxation time. It is more adequate to express the distribution function in terms of velocity rather than momentum, as it is easier in regards to calculating electrical currents. In equilibrium the Maxwell-Boltzmann distribution function can be used

$$f_{eq}(r, v) = n(r)\left(\frac{2\pi k_b T_0}{m^*}\right)^{-\frac{3}{2}} \exp\left(-\frac{m^*|v|^2}{2k_b T_0}\right)^3 \tag{2.50}$$

where $n(r)$ is the carrier density, T_0 is the lattice temperature, k_b is the Boltzmann constant, and m^* is the effective mass. The use of Eq. (2.49) for semiconductors is justified in equilibrium as long as degeneracy is not present. The carrier density is directly related to the distribution function according to

$$n(r) = \int f(r, v) dv \tag{2.51}$$

The significance of the relaxation time τ can be understood if the electric field is removed instantaneously and a space-independent distribution is considered. Hence, the Boltzmann equation can be expressed as

$$\frac{\partial f}{\partial t} = \frac{f_{eq} - f}{\tau} \tag{2.52}$$

Therefore, the relaxation time is regarded to be a characteristic decay constant for the return to the equilibrium state.

From here the drift-diffusion current equations can be easily derived from the Boltzmann equation. Considering a 1-dimensional (1D) geometry, the Boltzmann equation can be expressed as follows

$$\frac{eE}{m^*}\frac{\partial f}{\partial v} + v\frac{\partial f}{\partial x} = \frac{f_{eq} - f(v, x)}{\tau} \tag{2.53}$$

Here, the relation $m^* v = \hbar k$ is applied, which is valid for a parabolic energy band. Furthermore, consideration of the proper sign of the charge e should be taken with respect to the particle (i.e. positive for holes, negative for electrons). A general definition of the current density is given by

$$J(x) = e \int v f(v, x) dv \tag{2.54}$$

This definition can be related to Eq. (2.53) by multiplying both sides by v and integrating on v. The left hand side of Eq. (2.53) becomes

[3] In a 1-dimensional (1D) treatment, the $-\frac{3}{2}$ exponent is replaced with $-\frac{1}{2}$, while the appropariate thermal kinetic energy becomes $\frac{k_b T}{2}$ instead of $\frac{3k_b T}{2}$

$$\frac{1}{\tau}\left[\int v f_{eq} dv - \int v f(v,x) dv\right] = -\frac{J(x)}{e\tau} \tag{2.55}$$

The first term in Eq. (2.55) is an odd function (symmetric in v), and it's integral is equal to zero. Therefore, Eq. (2.53) becomes

$$J(x) = -e\frac{e\tau}{m^*} E \int v \frac{\partial f}{\partial v} dv - e\tau \frac{d}{dx} \int v^2 f(v,x) dv \tag{2.56}$$

Integrating by parts, one gets

$$\int v \frac{\partial f}{\partial v} dv = \underbrace{\left[v f(v,x)\right]_{-\infty}^{+\infty}}_{=0} - \int f(v,x) dv = -n(x) \tag{2.57}$$

It can be written that

$$\int v^2 f(v,x) dv = n(x)\langle v^2 \rangle \tag{2.58a}$$

$$\langle v^2 \rangle = \frac{1}{n} \int v^2 f(v,x) dv \tag{2.58b}$$

The DD equations are derived by introducing the mobility $\mu = \frac{e\tau}{m^*}$, and replacing $\langle v^2 \rangle$ with it's average equilibrium value $\frac{k_b T}{m^*}$, therefore neglecting thermal effects. Einstein's relation for diffusion $D = \frac{\mu k_b T_0}{e}$ is also introduced, and the resulting current equations are

$$J_n = q n(x) \mu_n E(x) + q D_n \frac{dn}{dx} \tag{2.59a}$$

$$J_p = q p(x) \mu_p E(x) - q D_p \frac{dp}{dx} \tag{2.59b}$$

where q is the electronic charge. To complete the set of equations within the DD model, there are the continuity equations

$$\frac{\partial n}{\partial t} = \frac{1}{q} \nabla \cdot J_n + U_n \tag{2.60a}$$

$$\frac{\partial p}{\partial t} = \frac{1}{q} \nabla \cdot J_p + U_p \tag{2.60b}$$

and the Poisson equation

$$\nabla \cdot (\epsilon \nabla V) = q(p - n + N_D - N_A + p_t - n_t) = \rho \tag{2.61}$$

From Eqs. (2.60a)-(2.60b), $U_{n,p}$ are the net generation and recombination rates. From Eq. (2.61), ϵ is the permittivity, V the electric potential, n and p the electron and hole mobile charge densities, N_D and N_A the donor and acceptor concentrations respectively. The terms p_t, n_t represent trap densities, and finally ρ is the charge density.

Eqs. (2.59)-(2.61) are a set of non-linear equations, that require an iterative approach to be solved. Furthermore, the continuity equations are conservation laws for the charge carriers. Meaning that: (i) the total number of particles inside a device is conserved, and (ii) the positivity of the carrier density is maintained (i.e. negative density is not a physical quantity). This is achieved by solving the DD equations within the finite element method (FEM). In FEM, a subdivision

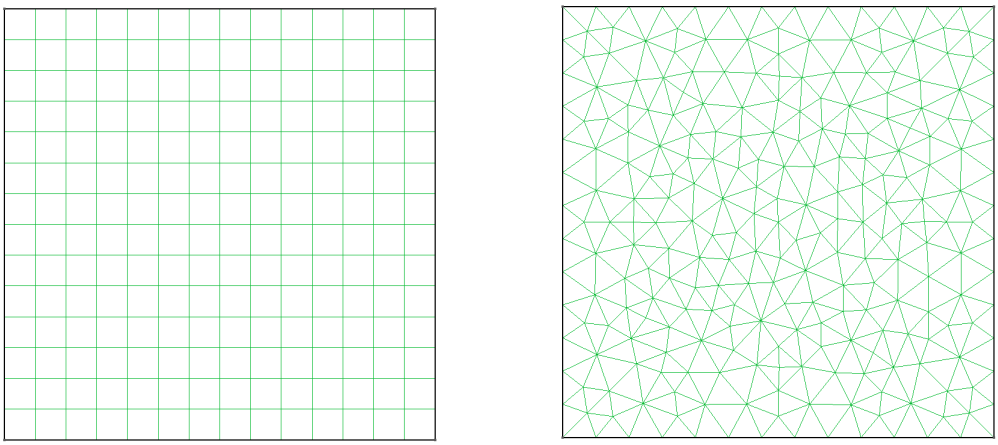

(a) Structured Mesh **(b) Unstructured Mesh**

Fig. 2.2: A basic illustration between **(a)** structured and a **(b)** un-structured mesh.

of the computational domain into smaller elements is carried out, and is referred to as a *mesh*. The currents are then defined on the boundaries of these elements, whereby the current exiting one element side is exactly equal to the current entering the neighbouring element though the common shared side. This enforces conservation. The iterative process begins with solving the Poisson equation for the electrostatic potential. The potential is then substituted into the continuity equations, and are solved to complete a single step. This iteration is continued until convergence is reached, and currents evaluated thereafter.

In order to carry out a successful iterative process in solving the DD equations, certain requirements should be taken into account:

1. Size and number of mesh elements
   - A *mesh characteristic length* defines the size of individual elements inside a computational domain. The smaller the size, the larger number of elements are produced. This implies how fine (or coarse) the resulting mesh is. Naturally, a finer definition is favoured for a more accurate simulation procedure, but this simultaneously increases simulation time-scales. Hence, depending on the domain at hand, a compromise is needed to have an accurate mesh representation (as much as possible), with the least simulation time.

2. Structured vs. unstructured meshes
   - A mesh can either be structured or unstructured (see Fig. 2.2). Both can be (and have been) used towards achieving the desired goal. There can be instances where both mesh variations can be applied together. Nevertheless, it is somewhat obvious that a structured mesh would be a better choice for domains that have sharp edges (i.e. squares, rectangles, hexagons, etc.). Conversely it would be more challenging to apply the same for smooth-around-the edge domains (i.e circles, cylinders, spheres, etc.). Therefore, in that case a unstructured mesh would be a more adequate choice. Consider the following
     - **Example:** A transistor channel region with a a length and thickness of 12 µm

and 10 nm, is placed on top of an oxide with a thickness of 200 nm. Regions are rectangular and an unstructured mesh is used (i.e. usually the default option in meshing software). Since, all important aspects governing charge flow occurs in the channel (and at the interface), this region requires a finer mesh definition as compared to that of the oxide. Given a large difference between sub-domain sizes, there is an abrupt transition from large sized elements of the oxide, to (possibly significantly) lower sized elements in the channel. This abrupt transition could lead to convergence issues. A further degree of complexity is added due to the different orientations of the individual elements. To avoid such an abrupt transition, one can decrease the element size in the oxide region (further increasing their number), but this would increase simulation time-scales. A solution to this problem would be to apply a structured mesh approach. In this fashion, the restriction on *not* wanting to increase the number of mesh elements (in the oxide) is eased. For a same domain size, an unstructured mesh would have more elements than that of a structured one. Furthermore, a smoother and ordered transition is achieved. This example highlights the approach used in the DD simulations detailed in chapter 4. Of course such an argument cannot be generally applied, as it is dependent on the domain (and it's sub-regions) shape and size. Yet it provides a thinking process towards choosing the appropriate meshing algorithm.

Chapter 3

On the atomistic scale

This chapter focuses on atomistic scale simulations. More specifically, an ab-initio approach investigating charge transport through self-assembled monolayers (SAMs). Firstly, an introduction on SAMs is given in Sec. 3.1, discussing several aspects including their structure, the main functions of their building block, and fabrication techniques. Sec. 3.2 provides an insight on the different applications of SAMs, with a focus on enhancing organic field effect transistor (OFET) performance, such as improved charge injection, charge carrier mobilities, etc. Organophosphonate SAMs are the main subject of this theoretical study (in Sec. 3.3). Using density functional theory (DFT), electronic structures of different types of organophosphonate SAMs are calculated in both gas-phase (i.e. stand-alone) and on silicon/aluminum oxide (Si/Al_2O_3) substrates. This is followed by applying the non-equilibrium green's function (NEGF) formalism to simulate charge transport through these monolayers and evaluate corresponding current-voltage (I-V) characteristics. Coupling between both electronic structure and transport analysis aims to provide a deeper understanding towards realizing SAMFETs as novel organic (molecular) devices.

Results reported in this chapter ***are to be submitted*** to a scientific journal[1]. This work was a collaborative effort with the group of Prof. Marc Tornow at the Faculty of Electrical and Computer Engineering (Associate Professorship of Molecular Electronics), at the Technical University of Munich (TUM).

3.1 Self assembly

Over the past decades, research has come a long way in bridging the gap between device engineering and molecular electronics. Furthermore, the field of organics required a much deeper understanding of the physics of charge transport on the nanometer scale. The first approach towards molecular electronics was taken by Aviram and Ratner in 1974 [81], proposing a donor-acceptor linked molecule sandwiched between two metal electrodes acting as a rectifier. This work opened a new avenue towards efforts to realize novel electronic devices, hence the introduction of self-assembled monolayers (SAMs). The keyword here is "self assembly". Witesides and Grzybowski defined it as "autonomous organization of components into patterns and structures, without human intervention" [82]. SAMs are made up of three sub-units illustrated in the top panel of Fig. 3.1. First, is the *anchor* group responsible for binding the molecule onto a substrate [83]. The *chain* comes second, and is responsible for molecular ordering, as well as electrical properties. SAMs can be made insulating or conductive [84, 85, 86, 87, 88, 89]. Last, is the *head* group which determines the surface energy and chemistry of the subsequent layer [90]. Having a variety of choices for the anchor, chain, and head gives the freedom to engineer different types of SAMs with different functionality [91, 92, 93]. Ease of fabrication is another attractive attribute of SAMs. These processes can can either follow a top-down or bottom-up approach

[1] At the time of writing this thesis

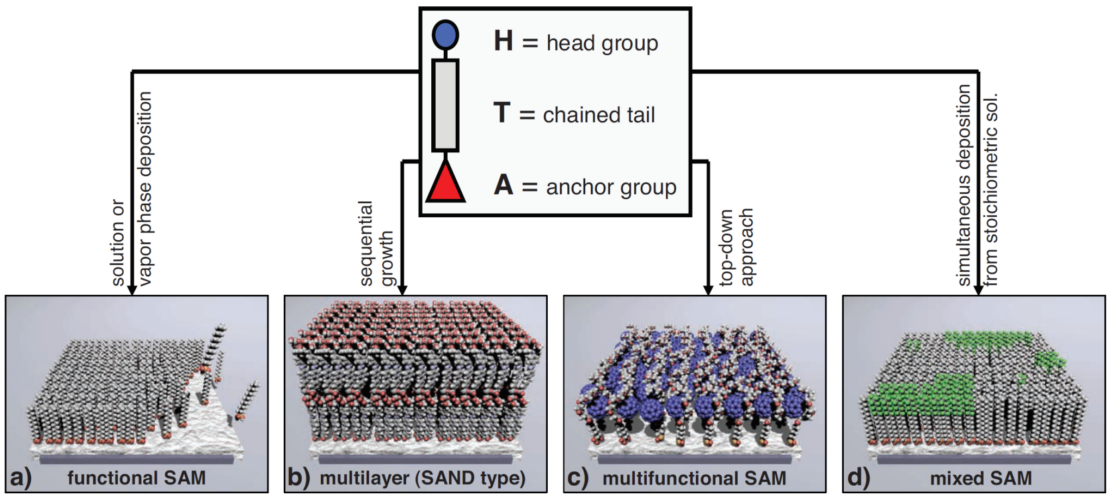

Fig. 3.1: Top panel: Sketch of a SAM-forming molecule depicting the main building blocks. **Bottom panel:** The various functionalities of SAMs in organic based devices. *Reproduced with permission from [90]. Copyright 2011 Wiley-VCH Verlag GmbH*

[90]. In the former, SAMs are synthesized and then deposited on the target surface. As for the latter, a precursor is initially deposited on the target surface which undergoes a subsequent process to form the final structure. Here, the first few adsorbed molecules "lie flat" on the surface. As more molecules start to form they create clusters "standing up" as a result of the intermolecular interaction between adjacent molecules. This clustering continues until a densely packed 2-dimensional (2D) monolayer is obtained [94].

SAMs fabricated from solution based processes or condensed from gas phase, involving either approaches have been demonstrated [95]. One example is micro-contact printing [96]. It involves a stamp with a certain pre-defined pattern, dipped into a solution of SAM-forming molecules which is then transferred and pressed onto the target surface, whereby the SAM is deposited imaging the pattern of the stamp. Using micro-contact printing sub-100 nm feature sizes have been achieved. Another method utilizes scanning probe lithography techniques. Using atomic force microscopy (AFM), SAM-forming molecules are deposited from the probe tip onto the target surface (a process referred to as dip-pen lithography). SAMs can also be removed from a surface by AFM, with enough applied force. The removal is called "nano-shavinig" [97]. If this process is taking place while the surface immersed in a different SAM-forming molecule solution, it is called "nano-grafting" [98], where the removed monolayers are replaced by a different one. Nanometer feature sizes where also reported using dip-pen lithography [99, 100]. What these methods (and various others) attain, is that they are low-cost and low-temperature fabrication techniques. Something conventional pattering and lithography processes (i.e. in inorgaincs) are not known for, especially when it comes to organic based devices.

3.2 SAMs: A wide range of applications

SAMs have been under investigation for a wide range of applications. The field of biotechnology should certainly be mentioned. Applications such as drug delivery [101], implantable devices [102,

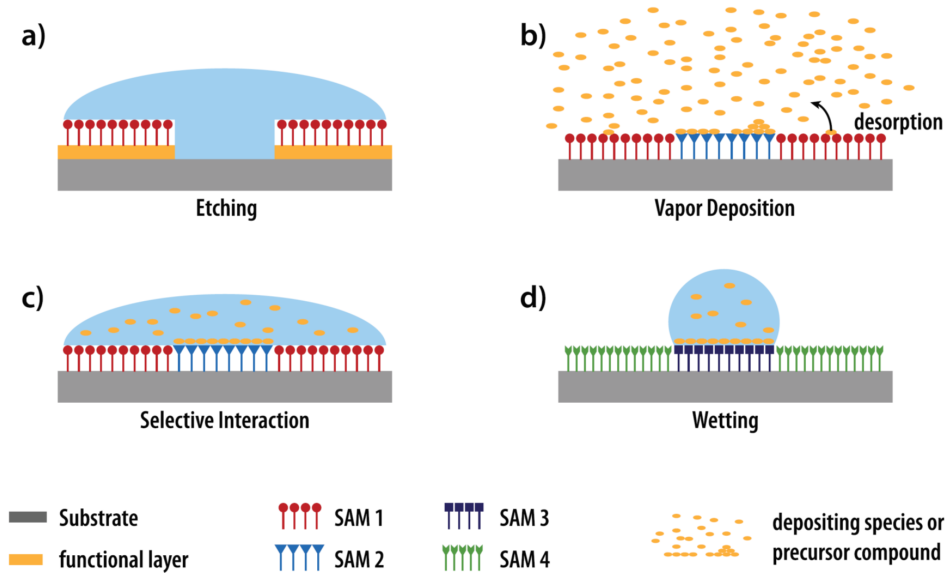

Fig. 3.2: Different approaches of SAM-based patterning techniques. **(a)** SAMs used as protective masks during the etching process of the underlying layer. **(b)** Regio-selective deposition based on favoured/unfavoured interactions between the deposited species and SAMs. **(c)** A similar regio-selective process to vapor deposition, but rather from solution. **(d)** Deposition of the target species based on the wetting properties of the solution used with respect to the SAM. *Reproduced with permission from [94]. Copyright 2017 Wiley-VCH Verlag GmbH*

103], and tissue engineering [104] require a great deal of knowledge on the interaction between biological matter and the attached surfaces. These interactions could then be interpreted as some sort of current or voltage measurement for further analysis and processing. Though, the major challenge here is retaining the functionality and avoiding any kind of structural damage of these biological matters, through the intended interaction. SAMs provide a solution for such challenges. SAM-functionalized surfaces have been reported to promote adhesion of biological matter [105]. Conversely, SAMs can also be used to resist binding of certain species. A process known as anti-fouling [106, 107]. For example, Chapman *et al.* [108] reported on surfaces functionalized with different types of SAMs resisting protein adsorption. Furthermore, they listed the required features these SAMs should possess so that the functionalized surfaces be anti-fouling.

In Sec. 3.1 it was briefly touched upon, the different approaches for the the fabrication of SAMs. To add to their advantageous features, SAMs themselves can be used as patterning tools for organic devices. As it was previously stated, head groups of SAMs define and control the deposition of any subsequent layer. Hence, SAMs with different head groups can be used to selectively define areas where the overlaying layers should be deposited depending on the chemical interaction, with very high precision. In a review written by Schmaltz *et al.* [94], they divide the different SAM-based patterning techniques into four categories. The four categories, namely: (a) etching, (b) vapor deposition , (c) selective interaction, and (d) wetting, are all depicted in Fig. 3.2. SAM-based etching (Fig. 3.2(a)), involves the removal of the underlying layer by an etching process in the areas uncovered by a protective SAM. In vapor deposition (Fig. 3.2(b)), SAMs with different head groups could be used to define the areas of both strong and

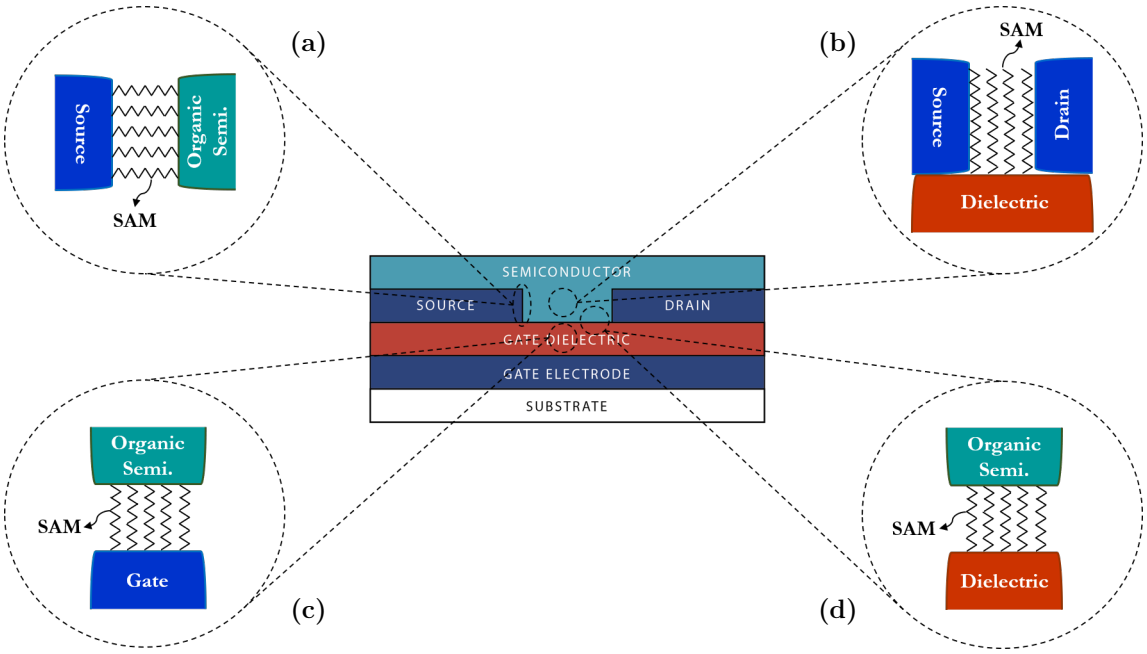

Fig. 3.3: Illustration of the various regions were SAMs can be applied to enhance OFET performance. **(a)** SAM-functionalized contacts, **(b)** SAM active regions, **(c)** SAM nano-dielectrics, and **(d)** Oxide/SAM hybrid dielectrics.

weak adhesion with particles deposited from gas-phase. In the latter, desorption occurs leading to selective growth of subsequent layers. Selective interaction (Fig. 3.2(c)) is similar to vapor deposition, but the process is rather undertaken within a specific solution. Finally, the wetting process (Fig. 3.2(d)) relies on the properties of the solution itself and it's interaction with the SAM, which in turn defines where the the deposition occurs. Indeed, these methods have been demonstrated in processing OFET components, from patterning electrode layers for different types of metals [109, 110], to defining active regions of devices (i.e. between the source and drain contacts) [111, 88].

SAMs can also be used to enhance OFET performance. Hence, the motivation behind the simulation study presented in the following section. To improve device performance, SAMs can be introduced at four distinct regions within an OFET: (i) at the contact-organic interface, (ii) at the dielectric-organic interface, (iii) or itself as a dielectric, (iv) and finally acting as the active material in the channel region. These regions are illustrated in Fig. 3.3.

1. SAM-functionalized contact-organic interfaces
   - As shown in Fig. 3.3(a), these are SAM-forming molecules present at the interface between the electrodes (i.e. source/drain) and organic semiconductor. When it comes to functionalizing electrodes, the family of thiol SAMs are regarded as the most suitable candidates. Thiol-SAMs are made up of molecules, where the chain (can be either aliphatic or aromatic [112]) is terminated by a sulfanyl group (-SH group). It is similar to that of a hydroxyl group, but the oxygen is replaced with a sulfur atom. Gold is probably the most common metal found in the literature to be functionlized by SAMs. Nevertheless, a variety of other metal substrates have been reported as well. A 2014

review by Vericat *et al.* [113] provides an interesting read on various thiol-SAMs on different metal substrates. Concerning OFETs, the electrode-organic semiconductor interface plays a crucial role on device performance relating to the efficiency of charge injection. It is common to observe the presence of defects at the boundary of the electrodes during the growth process of organic semiconductors [114], which has a direct effect on charge injection. With the inclusion of SAMs at the interface, improved morphology of the active layers at the boundaries resulted in enhanced performance for various channel length OFETs [115]. Another common issue present at the interface is formation of Mott-Schottky barriers as a result of a difference between the metal workfunction and either the HOMO or LUMO of the organic semiconductor. SAMs have been shown to tune metal workfunctions with the introduction of interface dipoles, improving device performance [116, 117]. Tuning of metal workfunctions with SAMs have also been adopted for light emitting diodes, improving device external quantum efficiency [118].

2. Hybrid dielectrics: SAM functionalized oxides

   - Charge carrier transport occurs within the first few monolayers inside the channel region of an OFET [119, 120]. Hence, dielectric-organic semiconductor interfaces have a direct effect on charge transport properties. Due to polarization effects, as well as the presence of defects, dielectric surfaces can alter the density of charges and their flow inside the channel [121]. Furthermore, surface properties of dielectrics are one of the main factors that governs the growth process, and subsequently the quality of the organic semiconductor. Size of crystalline domains, molecular orientation, and co-existing polymorphs, are affected by surface tension and roughness of dielectrics [122]. SAMs have been proposed to manipulate surface properties of dielectrics, facilitating improved growth mechanisms of organic semiconductors [123] (Fig. 3.3(d)). Similar to the use of thiol-SAMs on electrodes, there are several types of SAMs that have been utilized at the the dielectric-organic semiconductor interface. Organo-silicon monolayers (sometimes referred to as silanes) are one example, which have been used commonly on silicon oxides [124]. Silanes have been shown to be mechanically robust and thermally stable [125, 126]. They bind strongly to both the underlying surface and adjacent molecules through a silicon-oxygen-silicon (Si-O-Si) network [83]. Both Si atoms are contributed from the SAM molecules, and the O atom from the dielectric respectively. In a study carried out by Shtein *et al.* [127], they compared electrical characteristics of OFETs with pentacene grown on bare SiO_2, and those treated with octadecyltrichlorosilane (ODTS). The SAM modified device exhibited smaller grain sizes within the pentacene thin film, as well as better contact between individual grains. An increase in the charge mobility by a factor of three, and current on/off ratios of 10^8 were measured. A significant improvement from the untreated device. Organo-phosphonates are another type of SAMs used to improve dielectric-organic interface properties of OFETs. These SAMs are terminated with a phosphonic acid head group (i.e. -$PO(OH)_2$). Organo-phosphonates also exhibit high degree of molecular order and stability, even more so than silanes [128]. An experimental study conducted by McDowell *et al.* [129], fabricated pentacene OFETs with organo-phosphonate SAM treated oxides. Compared to devices with bare oxides, they recorded a decrease in the subthreshold slope from 1 V/decade to 0.2 V/decade, and a shift in the threshold voltage from $+13$ V to -4 V.

3. SAMs as nano-dielectrics
    - Application of SAMs in a hybrid dielectric setup certainly improved OFET performance. Nevertheless, these devices still required the need for high operating voltages as the inorganic oxide was mainly responsible for the overall capacitance. Current organic devices incorporate oxides with a typical thickness between 50 nm and 200 nm. Per the relation $V_{GS} = Q/C = Qd/\varepsilon\varepsilon_0$, where V_{GS} is the gate voltage, Q the charge density, C the capacitance, d the oxide thickness, and ε the dielectric permittivity, one coud either reduce the oxide thickness, or use high-κ dielectrics. Both ways lead to lower operating voltages, but neither are long term solutions. With the continuous need to reduce device feature size (i.e. per Moore's law [130]), reducing oxide thickness will lead to increased current leakage through the oxide. High-κ dielectrics merely postpone this effect. To this end the proposition was, to use SAMs serving as oxides. SAMs can be engineered to exhibit insulating properties allowing them to be a suitable candidate, as shown in Fig. 3.3(c). Halik *et al.* [131] reported on pentacene OFETs fabricated with silane-SAMs acting as the dielectric layer. These devices recorded leakage currents as low as $10^{-9}\,\mathrm{A/cm^2}$ operating at gate voltages of 2 V. Furthermore, for a thickness of just 2.5 nm, breakdown occurred at electric fields of 14 MV/cm (i.e. around 2.5 V). These measurements are better than SiO_2 dielectrics of similar thickness [132]. Organo-phosphonates SAMs were also used as nano-dielectrics to fabricate both p- and n-type OFETs on flexible substrates [133]. Device thicknesses just over 100 nm and under bending conditions (i.e. 100 µm radius), were operated at voltages between 2 V and 3 V. Such devices aim for large scale, low power consumption integrated circuits. The use of SAMs as nano-dielectrics was extended further. If the individual molecules possess identical anchor and head groups, one can achieve multi-layered nano-dielectrics though step-by-step self assembly. These structures are referred to as self-assembled nano-dielectrics (SANDs). An excellent review on these novel structures can be found here [134].

4. SAMs as active layers for charge transport
    - SAMs have been used at different interfaces of an OFET, improving device physical and electrical characteristics. Therefore, it does not come as a surprise to see the application of SAMs as the active layer of a device, depicted in Fig. 3.3(b). In this case these devices are rightly named self-assembled monolayer field effect transistors (SAMFETs). The major difference in terms of charge transport, between SAMFETs and OFETs, it that in the former the entire thickness acts as the accumulation layer. The latter is usually much thicker with only the first few nanometers serving as the accumulation layer. Hence, this requires SAMFETs to have strong intermolecular interaction between the individual molecules and a complete coverage of the area defined as the active region. The importance of area coverage was highlighted upon by Mathijssen *et al.* [135]. They carried out a study on SAMFETs with varying channel length between 1 µm-40 µm. Devices were immersed in SAM-forming solutions for different timescales, resulting in either full or partial coverage of the active region. Devices exhibiting full coverage showed the drain current to be inversely proportional to the channel length, with the mobility virtually independent. For partially covered devices, they observed a superlinear decrease in the drain current with increasing channel lengths. Moreover, no current was detected for channel lengths higher than 7.5 µm, and an exponential decrease in mobility. They concluded that transport occurred through percolation paths, that were otherwise difficult to form for increasing channel lengths. Such a study

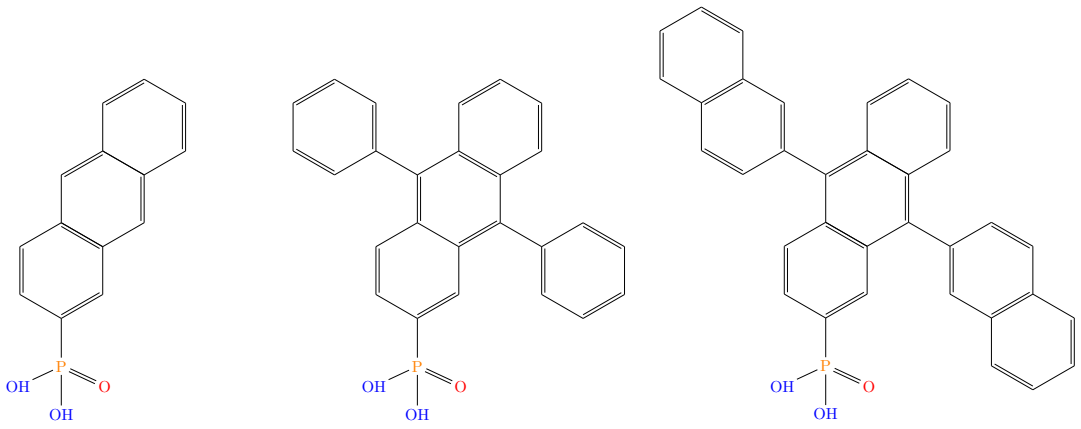

A1mono **A2mono** **A3mono**

Fig. 3.4: Molecular structures of the organo-phosphonate SAM-forming molecules in this study. Anthracene-2-phosphonic acid (A1mono), 9,10-diphenylanthracene-2-phosphonic acid (A2mono), and 9-10-dinaphthylanthracene-2-phosphonic acid (A3mono).

highlighted the importance of processing times to form densely packed SAMs insuring complete coverage within the active region for efficient device performance. One year earlier, the same group successfully demonstrated logic functionality with a 15-bit code generator integrating more than 300 unipolar SAMFETs [86]. In another approach addressing SAMFETs for complementary logic, Novak *et al.* [136] demonstrated both p-and n-type transistors operating in ambient air. More importantly, they combined the several functionalities of SAM to address multiple issues all at once. Using quaterthiophene (C_2-4T-C_{12}-PA; p-type) and fullerene-alkyl phosphonic acid linked SAMs (glycol-C_{60}-C_6-PA; n-type), they fabricated SAMFETs with: (i) hole and electron transport, (ii) low operating voltages, (iii) hybrid dielectrics, and (iv) device stability (for the n-type SAMFET).

Such is the promise of SAMFETs and self-assembly in a wider sense, hence the motivation behind the theoretical investigation presented in the following section.

3.3 Organo-phosphonate SAMs: A DFT/NEGF study

Organo-phosphonate SAMs are the subject of the work detailed here. The aim is to understand the nature of charge transport through these SAM-forming molecules, acting as the active layer of a SAMFET. How exactly do charges flow through these molecules, and if it is *intra*-chain dominant (i.e. within single molecules), or *inter*-chain dominant (i.e. between neighbouring molecules), or a combination of both, are several questions that can be difficult to answer from an experimental perspective. Hence, a theoretical approach using DFT and NEGF (see Chapter 2) is required, towards providing a clearer understanding of charge transport through SAMs. Using the QuantmATK atomistic simulation tool, the three different SAM-forming molecules of interest (also shown in Fig. 3.4) are: (i) anthracene-2-phosphonic acid (***A1mono***),

Geometry Optimization Parameters	
Temperature	300 K
E_{xc} Functional	PBE (GGA)[2]
Basis Sets	Double-zeta polarized (DZP)
Hartree Energy Tolerence	10^{-5} H
Force Tolerence	0.05 eV / Å

Table 3.1: Defined parameters for the geometry optimization process of the organo-phosphonates in gas phase

(ii) 9,10-diphenylanthracene-2-phosphonic acid (***A2mono***), and (iii) 9-10-dinaphthylanthracene-2-phosphonic acid (***A3mono***) respectively. The approach taken in this investigation involves calculating the electronic structure of these SAM-forming molecules both in gas phase (as standalone systems), and on a dielectric surface. The dielectric of choice is aluminum oxide placed on top of a highly doped silicon substrate (p-Si/Al_2O_3) acting as one of the contacts. This is followed by capping the substrate/oxide/molecule configurations with gold as a second contact, for charge transport analysis.

3.3.1 Electronic structure in gas phase (standalone systems)

Electronic structure calculations entail finding the energetic minimum for a given geometry (referred to as geometry optimization). This is interpreted in terms of two quantities, namely the self-consistent calculation of the energy, and the forces (in units of eV/Å) acting on atoms within that geometry following their displacement from an initial position. A spring analogy could be used here for further explanation. Imagine an atom connected to a spring. If this atom is moved to a new position, as a consequence of this displacement an opposite force acts on that spring. If this force is too high, it means that the new position is energetically unfavorable. Hence, it is crucial to achieve low acting forces during a geometry optimization procedure. Geometry optimization also require specifying other parameters including the temperature, the basis sets for the atomic orbital description, etc. These parameters are summarized in Table 3.1, and used for simulating the geometry optimization of the molecules in question.

Following a successful geometry optimization and electronic structure evaluation, several quantities could be extracted. Frontier orbitals, highest occupied molecular orbital (HOMO), and lowest occupied molecular orbital (LUMO), identifying the onset of the valence and conduction bands are of particular interest. Band gaps are then easily evaluated. This is useful, to observe how the band gaps change with respect to the phenyl and and naphthyl substituted aromatic groups. Band gaps corresponding to all three molecules are illustrated in Fig. 3.5. Packed variants of the A2- and A3mono are also depicted. These variants are important to take into consideration. As it will be seen in the following sub-section, the intention is to mimic a monolayer of overlapping molecules (i.e. similar to what is present inside the active region of a SAMFET)[3]. From Fig. 3.5 a slight decrease in band gaps from the A1mono towards the packed variants, can be seen resulting from a shift in both the HOMO and LUMO levels. The further increase in conjugation and therefore, the larger degree of delocalization across the molecules, leads to a reduction in

[3]With respect to defined boundary conditions

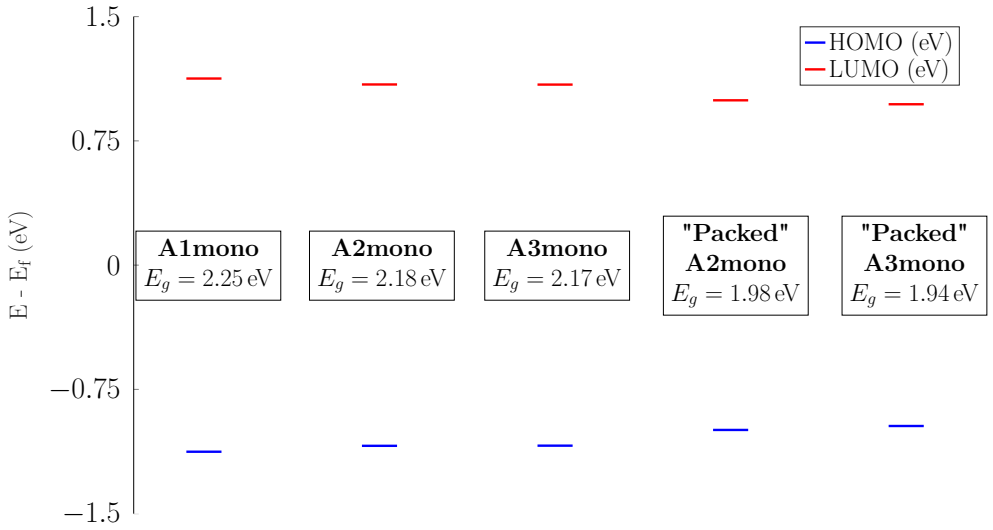

Fig. 3.5: Molecular energy spectrum for all molecular configurations. Band gaps are evaluated (also shown) as the difference between the HOMO (blue) and LUMO (red) energy levels.

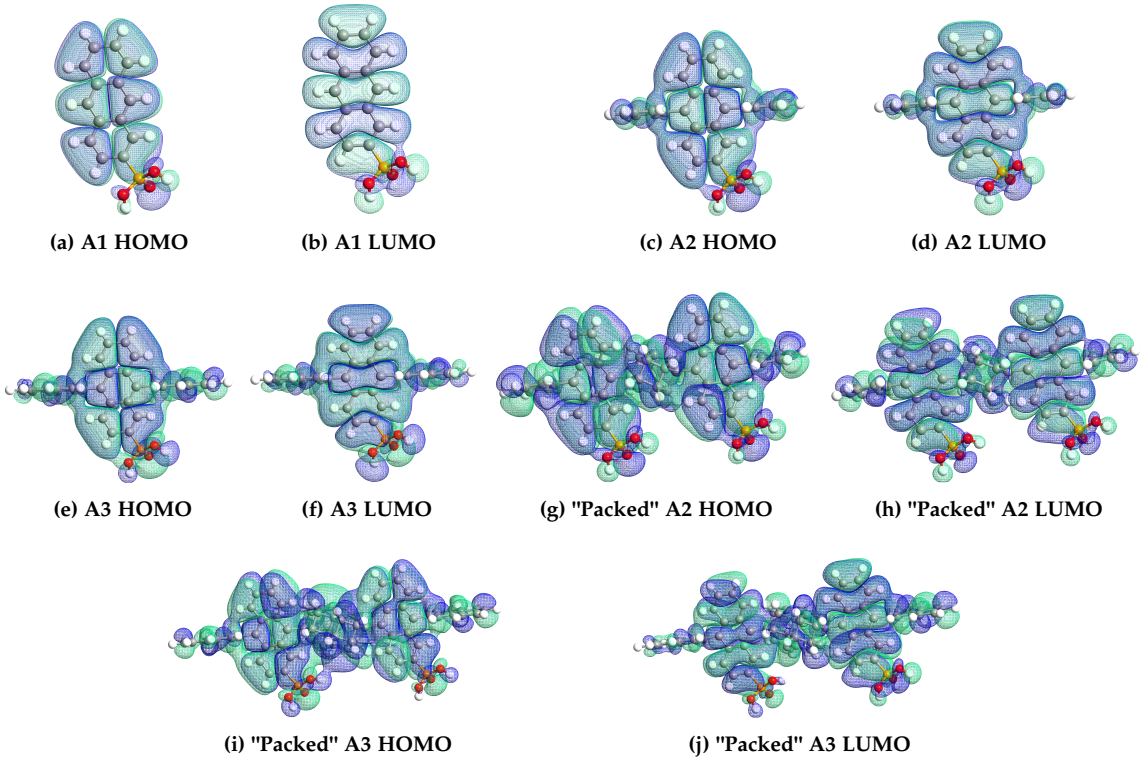

Fig. 3.6: Molecular orbital projections: **(a,b)** A1mono, **(c,d)** A2mono, **(e,f)** A3mono, **(g,h)** "packed" A2mono, **(i,j)** "packed" A3mono.

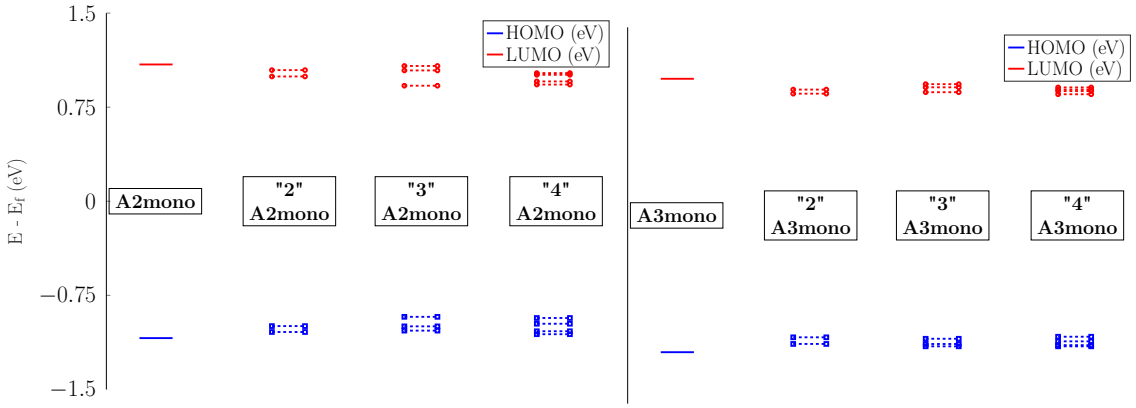

(a) Band splitting A2mono **(b) Band splitting A3mono**

Fig. 3.7: Frontier orbital splitting as a result of increasing number of overlapping molecules. **Left panel:** A2mono, **Right panel:** A3mono.

	A2mono (A3mono)			
	Single	**"2"**	**"3"**	**"4"**
HOMO	−1.09 eV (−1.085 eV)	−0.99 eV (−0.97 eV)	−0.92 eV (−0.98 eV)	−0.93 eV (−0.96 eV)
LUMO	1.09 eV (1.085 eV)	0.99 eV (0.97 eV)	0.92 eV (0.98 eV)	0.93 eV (0.96 eV)

Table 3.2: HOMO and LUMO energies corresponding to different overlapping configurations of both the A2- and A3mono.

evaluated band gaps. Molecular orbital representations (sometimes referred to as eigenstates) of both the HOMO and LUMO are projected on the respective geometries, and further illustrated in Fig. 3.6. From these projections, the orbitals extend across both the molecular backbone and the substituted aromatic groups. This provides a preliminary indication of possible lateral charge transport between neighbouring molecules. Nevertheless, this picture might change for more complex systems involving other surfaces (e.g. contacts).

Another important aspect affecting band gaps, is the molecular overlap. As the intermolecular distances between neighbouring molecules decrease, this leads to an increase in frontier orbital energy level splitting [137, 138, 139]. To study this phenomena, band gaps of up to four adjacent molecules for both the A2- and A3mono were considered. Bands gaps for the different overlapping configurations in increasing order, are depicted in Fig. 3.7. Furthermore, the difference between energy levels within the HOMO and LUMO bands as a result of the overlap, are listed in Table 3.2. From these results, one can conclude that eventhough a somewhat appreciable change in the HOMO (LUMO) is noted for the first instance of overlap, this change decreases and the HOMO (LUMO) level start to stabilize around a certain energy. The combination of both the conjugation and overlap is critical in identifying charge transport barriers with respect to the difference between the HOMO (LUMO) position and the contact workfunction.

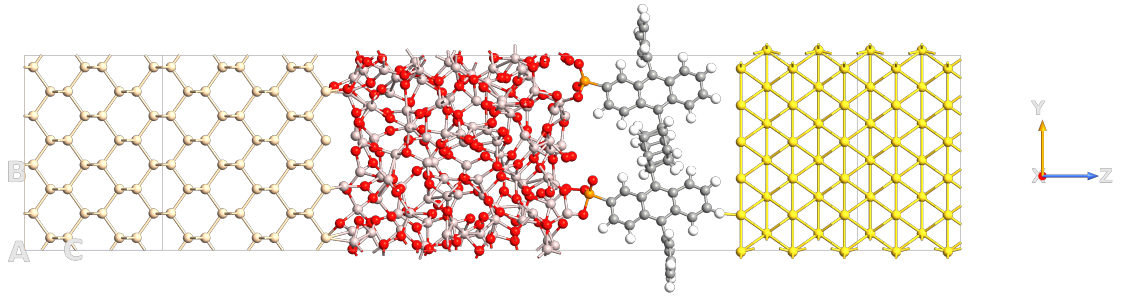

Fig. 3.8: Illustration of a constructed device configuration consisting of the four specified sub-regions: (i) p-Si, (ii) Al_2O3 dielectric, (iii) molecule (A2mono shown here), and (iv) gold contact

3.3.2 Charge transport through anthracene SAM-forming molecules

Following the gas phase analysis, device configurations are now constructed incorporating the previously examined molecular structures. Devices are split up into four sub-regions, namely: (i) the p-doped silicon substrate, (ii) the aluminum oxide dielectric, (iii) the SAM-forming molecule(s), and finally (iv) the gold contact. A process flow was followed to reach the final device layouts (shown in Fig. 3.8), and is detailed as follows:

1. **Substrate (contact)**: This was a fairly straightforward process. A silicon unit cell was used to form a substrate with a 100 crystal direction, and thickness of 3.2 nm in the *C (or z)* direction. The substrate was then left to geometrically relax and prepared for the following step.

2. **Dielectric**: Oxide structures in QuantumATK are all provided in crystalline form. Therefore, to obtain an amorphous Al_2O_3 structure, molecular dynamic (MD) simulations were employed. The resulting amorphous oxide (thickness of 1.9 nm) was then attached on top of the Si substrate. The oxide was left to relax, while keeping the underlying substrate in a fixed position.

3. **SAM-forming molecule(s)**: At this stage, all molecular configurations are attached to the oxide surface. It should be noted that this attachment involved the oxygen atom(s) of the phosphonic anchor groups and the oxide. The hydrogen atoms react with exposed hydroxyl groups on the oxide surface, forming water that is subsequently washed away leaving behind the attached molecules. The same relaxation process is carried out with the p-Si/$Al2O_3$ fixed in position. It is important to note the dimension of the substrate in the x, y directions. These dimensions specify the boundary conditions of the simulation. Whatever is inside these boundaries is then repeated "infinitely" in these directions. In regards to the packed variants of the A2- and A3mono, the x, y dimensions were chosen to be large enough to fit the molecules inside, yet also small enough to insure that the overlap is considered within the repetitions (per the boundary conditions), hence mimicking a SAM for the following simulations.

4. **Gold (contact)**: Similar to the Si substrate, gold with a thickness of 1.6 nm and crystal direction 100 was constructed, relaxed (i.e. standalone), and finally attached to the molecule, completing the device configuration. It should be noted that a hanging mercury droplet

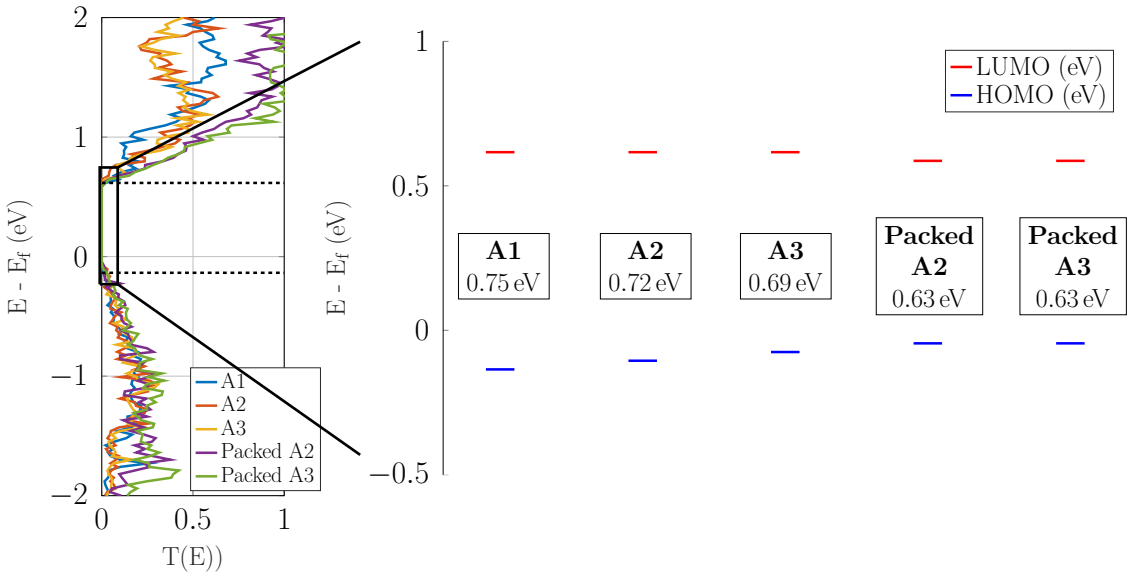

Fig. 3.9: Left panel: Transmission probability functions corresponding to all device configurations. **Right panel:** Conductive band gaps as extracted from the transmission function defined by the onset of the HOMO and LUMO bands (i.e $T(E) = 0$).

was used for which the nature of the contact between the anthracene-SAMs and the droplet was unknown. For this reason, the metal contact was treated as a boundary/layer at which charges are simply extracted (or injected). The contact was brought close enough to the molecule(s) until a covalent bond was formed.

5. The geometry relaxation for the different sub-regions of a device, involved the same simulation parameters described in Table 3.1 with the addition to one more, that is the k-point sampling. Defining k-points is required when dealing with structures inside a boundary box. The k-point sampling for each relaxation step is detailed below:
   - Standalone p-Si substrate ($5 \times 3 \times 3$).
   - Al_2O_3 dielectric on p-Si substrate ($5 \times 3 \times 2$).
   - SAM-forming molecule(s) on p-Si/Al_2O_3 ($5 \times 3 \times 1$).
   - Standalone gold contact ($5 \times 3 \times 3$).
   - Gold contact on p-Si/Al_2O_3/molecule(s) (no relaxation was carried out).

Now that all device configurations are set up, the focus turns to investigating charge transport through the anthracene SAM-forming molecules. This is carried out by first simulating the transmission probability functions for each device configuration. Transmission probabilities are used within the Landauer formalism to evaluate current-voltage (I-V) characteristics. Simulating the transmission function, an energy range between -2 eV and $+2$ eV was specified, and a k-point sampling of 15×7 in the a, b directions[4]. Transmission functions for the five device configurations

[4]k-point sampling tests were carried to to find the optimum values, keeping in mind that b is twice as long as a, hence fewer number of k-points are needed in that direction. Test carried out beyond 15×7 up to 15×15 did not affect the transmission functions

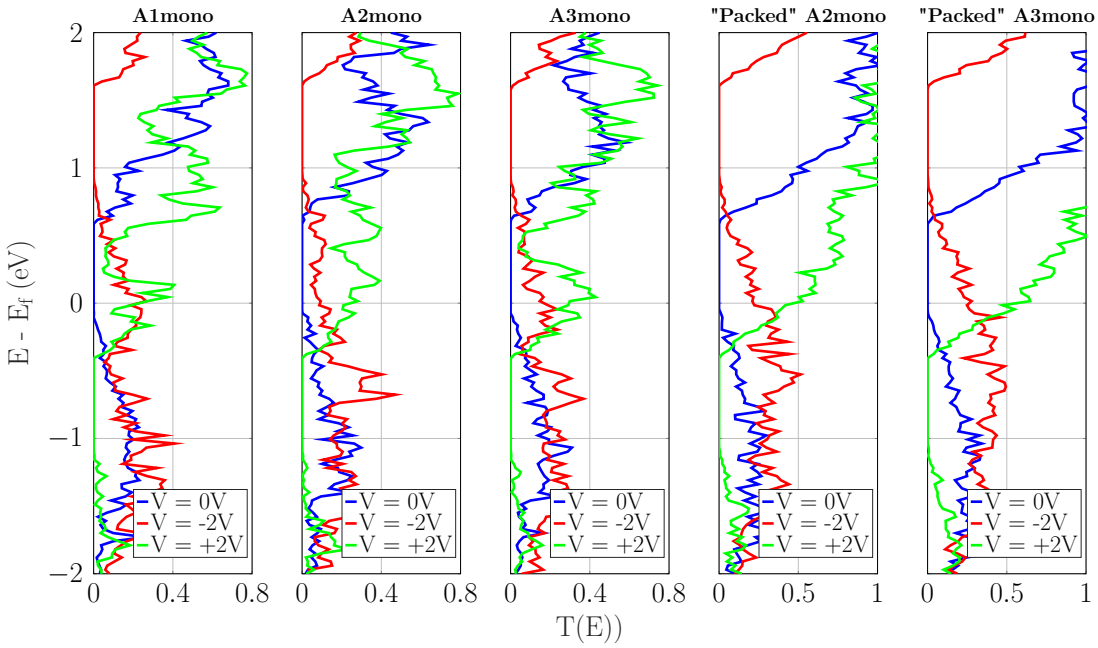

Fig. 3.10: A dependence of the transmission functions on the applied voltage, as a result of an observed shift.

are illustrated in left panel Fig. 3.9. Three distinct regions are clearly observed, the HOMO band, the band gap, and the LUMO band respectively. Onset of the HOMO and LUMO bands are marked at the point of sharp increase from a transmission $T(E) = 0$. Band gaps are evaluated and shown in the right panel of Fig. 3.9. A similar trend (to that of the gas phase analysis) of decreasing band gaps is observed, with the both the packed A2- and A3mono variants recording equal values. This particular aspect on the packed variants will be discussed in further detail shortly. Another question to be addressed reflects on the estimated values. Molecular band gaps within device configurations are around three times smaller than in gas phase. The electronic structure is sensitive to the presence of multiple surfaces. Hence "conductive band gaps" in device configuration are expected to be different from the "optical band gaps" in gas phase. Furthermore, DFT simulations are built on applying certain approximations and assumptions. Had the gold contact treatment been different, that would almost certainly alter the electronic structure of the molecules and subsequently the band gaps from a quantitative perspective. Nevertheless, a trend of decreasing gaps and higher transmission probabilities (i.e. for the packed variants) is captured. These are further indications of enhanced charge transport due to the extended conjugation and $\pi - \pi$ stacking (i.e overlap), of the substituted aromatic groups.

Transmission probability functions depend on both the energy and applied voltage. Yet a so-called "zero-bias" approximation is sometimes used when evaluating the I-V characteristics. This approximation states that for a small window of applied voltages, the transmission function at zero bias does not change much, and therefore could further be used without the need to recalculate the transmission at other voltage points within that same window. The main advantage behind this approximation, is that is saves on computational cost, which is rather high for DFT/NEGF based analysis. However, it is also system specific. Fig. 3.10 shows the effect of an applied voltage on the transmission function for the investigation systems. Eventhough, the

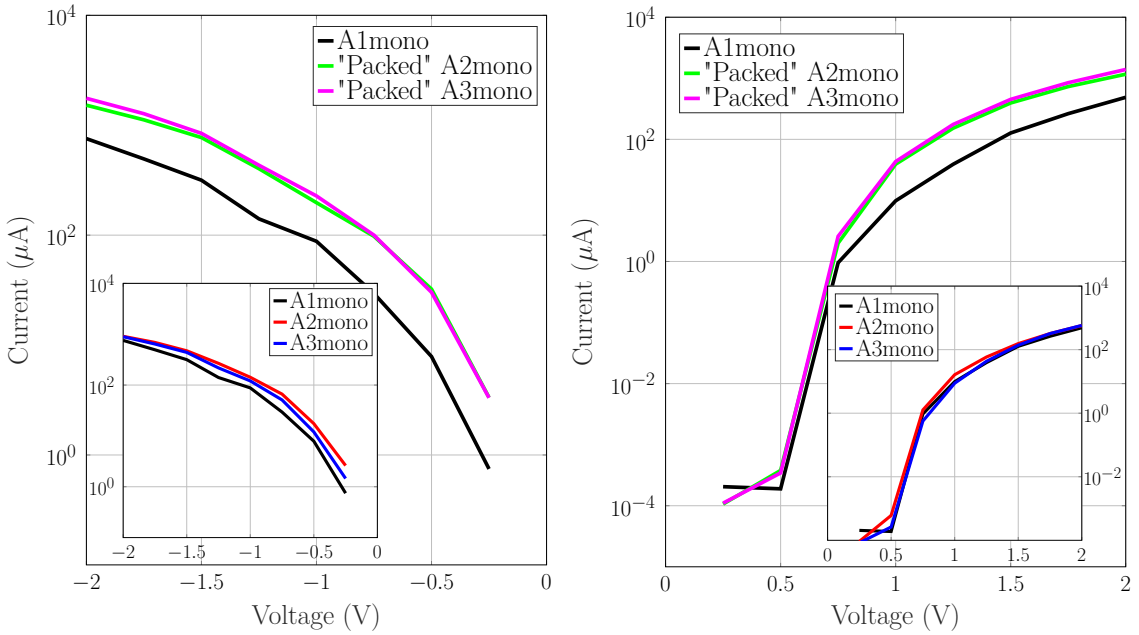

(a) Negative bias **(b) Positive bias**

Fig. 3.11: Current voltage characteristics under **(a)** negative and **(b)** positive biases. Difference in currents corresponding to the single (inset) and packed variants (main), highlight the consideration of a thin-film-like molecular configurations of the A2- and A3mono.

transmission functions more or less maintain their shape, a voltage-dependent shift is induced. For the presented systems, this implies that the zero-bias approximation is otherwise insufficient. For an applied voltage range between $-2\,\mathrm{V}$ and $+2\,\mathrm{V}$, a total of 16 transmission functions were extracted (8 for either the positive and negative branches). The resulting I-V characteristics are depicted in Fig. 3.11. From the insets of Fig. 3.11, both the A2- and A3mono exhibit higher currents compared to the A1mono. This is true for negative applied biases. For positive applied biases, it is difficult to distinguish between all three. Conversely, the main panel of Fig. 3.11 provides a more realistic picture, where the packed variants of the A2-/A3mono represent a monolayer of molecules. Packed variants of the A2-/A3mono exhibit higher current conduction compared to the A1mono, for both negative and positive branches of the applied voltages. Between the A2- and A3mono, only a very slight increase in current is observed for the latter. This recalls the earlier band gap results from Fig. 3.9. As both packed variants have equal sized band gaps, a large difference in current was not expected. The slight increase in favour of the A3mono can be attributed to the smaller distances between subsequent energy levels as a result of the splitting process (see Table 3.2). This simply implies a slight favour in the availability of transmission/conduction channels for the A3mono over the A2mono.

The expected effect of both the extended conjugation and overlap (although partially) was successfully reproduced by the simulations. It should be noted that a "complete" overlap between side aromatic groups was assumed for this investigation. One could argue that the relaxation process of the molecule(s) might alter the overlap and/or their orientation, hence generalizing the applied assumption. Although the orientation certainly changed, all "complete" overlaps were

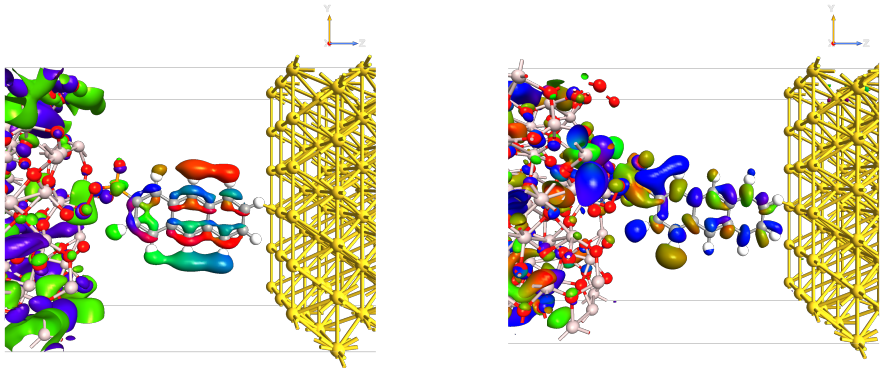

(a) **E** = 1.64 eV, **T(E)** = 0.67

(b) **E** = −1.73 eV, **T(E)** = 0.26

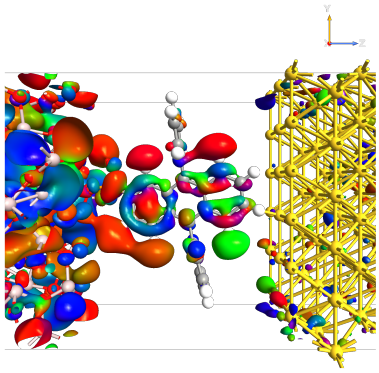

(c) **E** = 1.34 eV, **T(E)** = 0.64

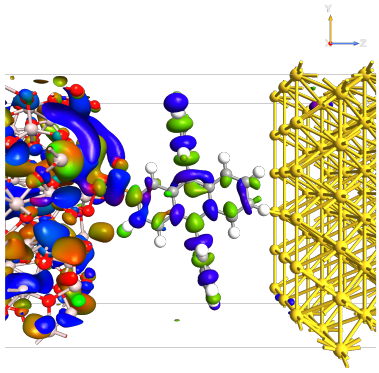

(d) **E** = −1.06 eV, **T(E)** = 0.3

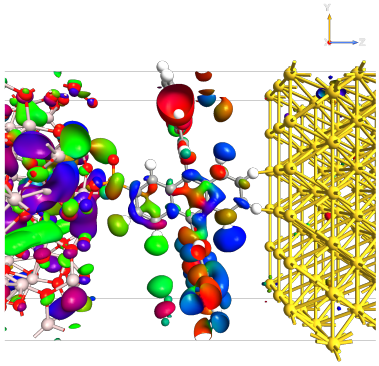

(e) **E** = 1.18 eV, **T(E)** = 0.58

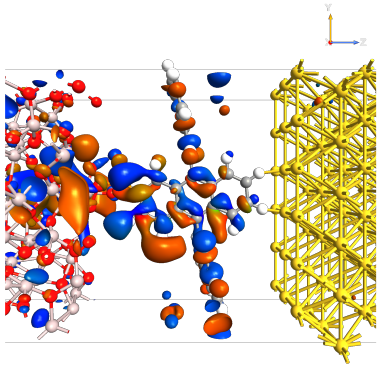

(f) **E** = −1.06 eV, **T(E)** = 0.31

Fig. 3.12: Molecular orbital representations corresponding to high transmission probabilities, identified inside the bands of the A1mono **(a,b)** HOMO, LUMO; A2mono **(c,d)** HOMO, LUMO; and A3mono **(e,f)** HOMO, LUMO.

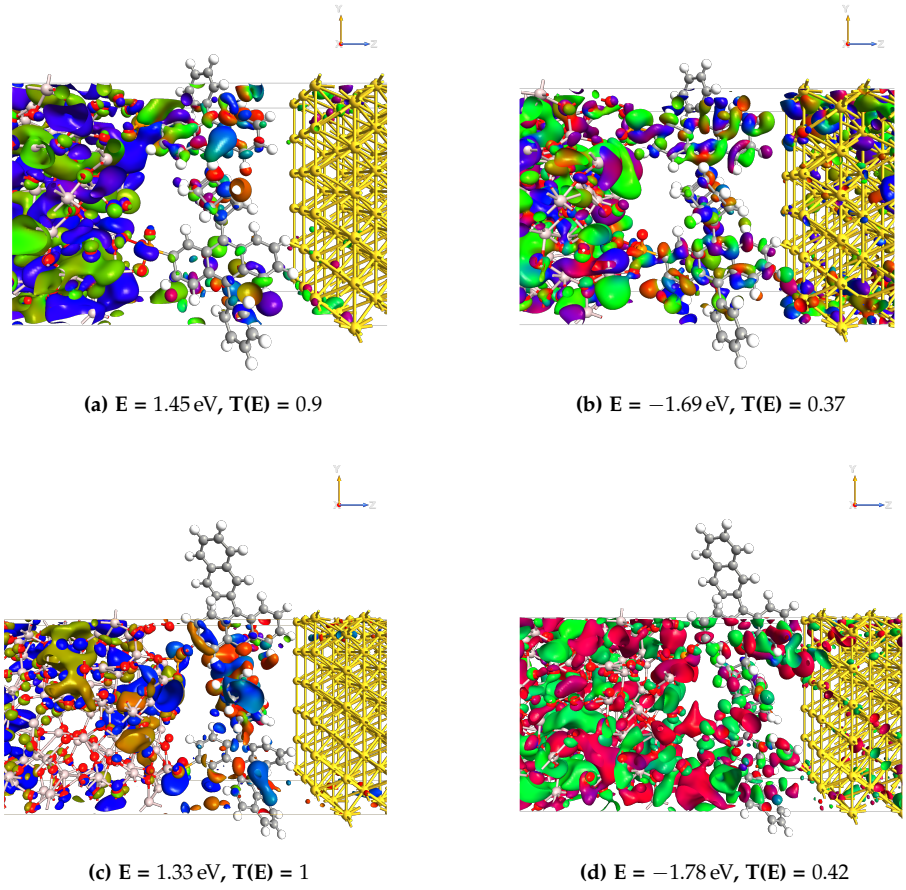

(a) **E** = 1.45 eV, **T(E)** = 0.9

(b) **E** = −1.69 eV, **T(E)** = 0.37

(c) **E** = 1.33 eV, **T(E)** = 1

(d) **E** = −1.78 eV, **T(E)** = 0.42

Fig. 3.13: Molecular orbital representations corresponding to high transmission probabilities, identified inside the bands of the "packed" variants A2mono **(a,b)** HOMO, LUMO; A3mono **(c,d)** HOMO, LUMO.

maintained. In reality, other instances (or even a combination) of overlaps could have existed. This changes the electronic structure significantly, and consequently band gaps, transmission, and finally the I-V characteristics. With that said, the A3mono would have recorded higher simulated currents (as compared to the A2mono) given the larger degree of conjugation and overlap. Nevertheless, the simulated results still show that anthracene-SAMs with substituted aromatic groups exhibit enhanced current drive. Hence, adding more emphasis on the presence of both intra- and inter-chain charge transport.

To justify the claim of possible inter-chain transport, energies with high transmission probabilities relative to the HOMO ($T(E) > 0.2$) and LUMO ($T(E) > 0.5$) bands were identified. Corresponding eigenstates were projected on the molecular-device configurations. Projections for all five configurations are illustrated in Fig. 3.12 and Fig. 3.13[5,6]. Shown projections extend across

[5]The shown transmission eigenstates are a complex wavefunctions. Isosurfaces represent the absolute value of the wavefunctions, while the color indicates the phase. As the phase is periodic, it was best to use a periodic map.

[6]Outlying atoms were *wrapped* around and included within the boundary conditions during the simulation process. For illustrative purposes, molecules were kept *un-wrapped* for the reader to distinguish between the different configurations

the aromatic groups of overlapping molecules, for both the A2- and A3mono. This confirms an exchange of charges between neighbouring molecules takes place as a form of inter-chain charge transport. The major conclusion behind these finding, is that SAMs incorporating substituted aromatic groups in organo-phosphonate molecules could indeed be utilized as active region material for OFETs. It should be noted that these results consider contacts and applied fields on the vertical axis of the configurations, implying that evaluated I-V characteristics account for leakage currents. However, this does not alter the concluding arguments that inter-chain transport does indeed take place. With the presence of source-drain electric fields as a driving force, transport through these molecules would also favour flow of charges in that direction.

3.4 Conclusions

Three different organo-phosphonate molecules were considered in this investigation, as possible candidates for the active region in FETs. Their respective molecular structures differed in terms of the either the absence or presence (with increasing size) of side chain substituted aromatic groups. Electronic structure calculations in gas phase led to the conclusion that the observed trend in decreasing band gaps, was due to: (i) the presence of the aromatic groups, (ii) their size, and finally (iii) the overlap between aromatic groups belonging to adjacent molecules. Increasing the number of overlapping molecules (i.e. towards creating a thin monolayer), showed that band gap defining HOMO and LUMO band edges tend to stabilize around a specific value. Charge transport simulations on device configurations incorporating these SAM-forming molecules resulted in higher current conduction evaluated for the molecules with side chain aromatic groups, albeit only a slight improvement was observed with respect to the size of the overlap. This increase in current conduction, was a consequence of the observed trend of molecular band gaps in device configurations, similar to the earlier findings in gas phase. Upon examination of the transmission function, energies recording high probabilities were identified and the corresponding molecular orbitals projected. It was concluded both inter- and intrachain transport can occur for overlapping molecules with side chain aromatic groups.

Chapter 4

On the macro-scale

In this chapter, the finite element method (FEM) and drift-diffusion model (DD) are applied, for the investigation and characterization of organic field-effect transistors (OFETs). In Sec. 4.1, an overview is provided on the nature of charge transport in organics. The important sub-models used in this theoretical investigation are presented. These include the density of states (DOS), the mobility, and trap models respectively. In Sec. 4.2, simulation and characterization of pentacene OFETs using the DD model is presented. Firstly, some simulation related remarks are highlighted. This is followed by investigating the effect of different kinds of traps, such as bulk and interface traps (either positively or negatively charged). The effect of fixed charges at the interface, between the oxide and organic materials, is also considered. The understanding behind such effects on device operation is then used to successfully fit experimental measurements, and important performance parameters are extracted. Sec. 4.3 ends this chapter with a conclusion of this study.

The results reported in this chapter have ***already been submitted*** to the Journal of Physics D: Applied Physics[1] They represent an organic based drift-diffusion model successfully used to characterize OFETs.

4.1 Charge transport in organics

The working principle of a FET is always the same, regardless of the active material used for the channel region. However, the underlying physics governing charge transport on the other hand is different between organic and inorganic materials. For the latter, charge transport occurs via coherent Bloch waves. In contrast, for the former, it is through hopping from one site to another within a varying energetic landscape, owing to individual molecules being bound together through weak Van der Waals interactions. Therefore, charge transport occurs through hopping between localized states. This hopping mechanism is appropriately described by the Gaussian Disorder Model (GDM) [140]. These energetic sites follow a random distribution which is described by a Gaussian function in the vicinity of an energy level of interest (i.e. Highest or Lowest Occupied Molecular Orbitals (HOMO or LUMO) respectively), and the width of this function is referred to as the energetic disorder. Such disorder is found in both small molecules and polymers, and is more pronounced in the latter. Multiple theoretical models have been proposed to describe the hopping of charges, namely: (1) Nearest Neighbour Hopping (NNH), (2) Variable Range Hopping (VRH), (3) The Transport Energy Model (TE), and (4) Multiple Trap and Release Model (MTR). Motion of charges described by any of these models does not only depend on the electric field but also the temperature. A more detailed overview can be found here [141].

This hopping mechanism is one of several forms of transport used to explain the movement of charges in organic materials. These also include band and polaron transport. Two important requirements need to be achieved for band transport to occur, which are the growth of high

[1] Currently under review

quality crystals, and the observation of a negative temperature dependence of the mobility. This dependence has been previously observed in Rubrene FETs by Podzorov *et al.* [142, 143]. The review by Hasegawa and Takeya [144] further highlights the significance of fabricating high quality single crystals to achieve high charge mobilities. On the other hand, polaron transport accounts for polarizations, which is a common occurence in organic materials. If a charge is present on a site for a long enough time, it starts to polarize the surrounding environment. The initial charge and the resulting polarization then propagate (together) within the material known as a polaron. As Horowitz thoroughly explains in [145], there can be different types of polarizations (i.e. electronic, molecular, and lattice) depending on the residence time of a charge on a specific site. Both electronic and molecular polarizations can occur on a timescale either below or comparable with the residence time. Lattice polarizations, which involves deformations can also occur but require longer timescales. A comparison between the different charge transport theories have been addressed, for example see Stallinga [146] and Troisi [147].

Charge transport in organic semiconductors is a much more complex process, therefore careful considerations need to be taken into account for the description of the sub-models used and their parameterizations in any drift-diffusion (DD) simulation. This allows for the correct characterization of organic based devices and subsequent comparison and validation with experimental measurements. In the following sub-section, the different sub-models used in the DD simulation will be presented and discussed in more detail.

4.1.1 Gaussian density of states (GDOS)

As it was stated before, charge transport in organic semiconductors relies on a a hopping mechanism through a random distribution of localized states. In order to have an appropriate description for this charge hopping, the density of states (DOS) is best described by a Gaussian function. This function is expressed as:

$$g(E) = \frac{N_0}{\sigma\sqrt{2\pi}} \exp\left(-\frac{E^2}{2\sigma^2}\right) \tag{4.1}$$

where N_0 is the site density, E the energy, and σ the energetic disorder respectively. Energetic disorder in organic semiconductors typically lies in the range between 30 meV and 100 meV [148, 149], and it relies on the morphology of the material. That is why polymers suffer from higher disorder compared to small molecules. Going from low to high disorder leads to an increase in the random distribution of sites further away from the transport level, as a consequence some of these sites might act as trap states affecting overall charge transport. Moreover, it has been shown that charge mobilites depend on the applied field, carrier density, and temperature (more on this will be discussed in sub-section 4.1.3). The dependence of the mobility on the latter two is affected by the DOS. Therefore, it is crucial to have a correct description of the DOS and the appropriate amount of disorder depending on the material chosen. Fig. 4.1 illustrates the hopping of charges between localized and extended states as described by the GDOS given some energetic disorder.

4.1.2 The trap model

Charge carrier trapping in organic semiconductor is one of the major factors affecting device performance. Depending on the energy associated with a trap state (i.e. how far is it inside the band gap), this can have different effects on device operations such as degrading mobilites [142, 150, 151], causing hysteresis [152], and leading to threshold voltage shifts [153, 154]. Stability

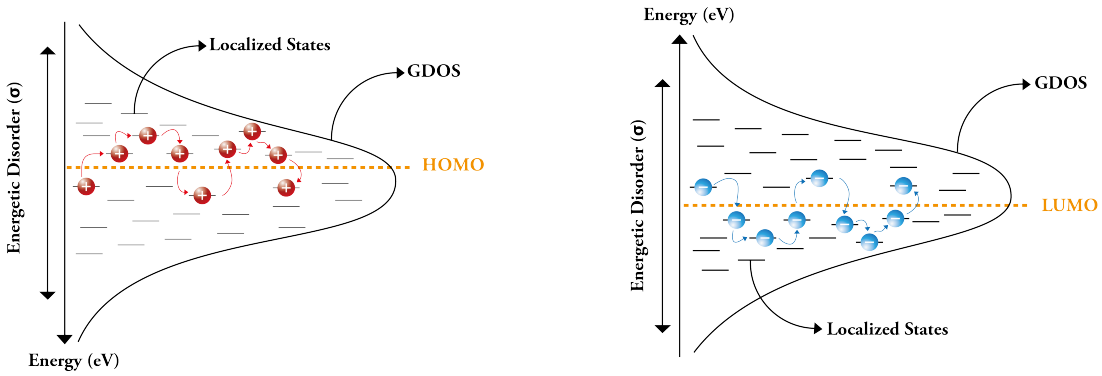

(a) HOMO band **(b) LUMO band**

Fig. 4.1: The hopping of charges through the **(a)** HOMO or **(b)** LUMO bands within a GDOS description

over extended periods of time is also a major issue in organic devices, more specifically the ones incorporating n-type materials as the active region. This is one of the reasons why complementary logic based on organics has been proven difficult to achieve. It is imperative to include traps in any DD simulation, and their effects could be seen from the transfer characteristics of an OFET. Traps are modeled as follows:

(i) A neutral trap that becomes negatively charged when an electron is trapped

$$n_t = \frac{N_t}{1 + \exp\left(\frac{(E_c - E_{t_n}) - E_{F,n}}{k_b T}\right)} \tag{4.2}$$

(ii) A neutral trap that becomes positively charged when an hole is trapped

$$p_t = \frac{N_t}{1 + \exp\left(-\frac{(E_v + E_{t_p}) - E_{F,p}}{k_b T}\right)} \tag{4.3}$$

(iii) Fixed charges where the density is simply defined. They can be either positive or negative.

In Eqs. (4.2) and (4.3), N_t denotes the density of traps, E_{t_n} and E_{t_p} the electron or hole trap energy level, $E_{F,n}$ and $E_{F,p}$ are the quasi-fermi energies, k_b the Boltzmann constant, and T the temperature respectively. The trap level can be taken with reference to the conduction or valence bands (i.e. E_c or E_v).

The above mentioned models (and their subsequent effect on charge transport) have been used extensively for the investigation of inorganic materials and devices. In order to justify their usage towards investigating charge transport in organics, they must be able to represent the physical meaning of certain phenomena (or events) that occur within organic materials and

devices. One of these events is the presence of dipoles, more specially interface dipoles. Dipoles exist as a result of inhomogeneous distribution of charges at a surface [155]. Such dipoles can occur at organic-organic [156, 157], and/or organic-metal interfaces [158, 159, 160]. They could also be present at dielectric interfaces [161]. Infact, self-assembled monolayers (SAMs) have been previously used to intentionally induce interface dipoles between the organic and dielectric materials, to influence the electrical characteristics of OFETs. As a result, controlling of charge densities leading improved field effect mobilities, as well as threshold voltage shifts have been observed [162, 163, 164]. A presence of a dipole causes a shift in the potential between two different interfaces (or surfaces). This shift is expressed as

$$\Delta_d = \frac{q m_d cos\theta}{A_d \varepsilon} \tag{4.4}$$

where q is the electronic charge, m_d is the electric dipole moment (given in units of debye and depends on the distance between the positive and negative charges), θ is the angle of the dipole with respect to the surface, A_d is the area of the surface charges, and lastly ε is the dipole layer's dielectric constant. Similarly, fixed charges represent a surface area of charges present at an interface, and through coulomb attraction, charges of the opposite sign are situated on the other side. Hence, this would be expressed as

$$\Delta_d = \frac{q}{A_d \varepsilon} \tag{4.5}$$

Both Eqs. (4.4) and (4.5) are almost identical with the exception of the angle θ, allowing the use of a fixed charges model to represent the effect of dipoles in DD simulations. This assumption is valid if the distance between the separate charges is within a fraction of a nanometer. In the following section, it will be shown how the fixed charges does indeed affect the threshold voltage and subsequently the field-effect mobility, therefore allowing the use of fixed charges to account for interface dipole effects.

A similar connection can be achieved in regards to modeling of trap states in the DD simulations. It is already quite obvious that the mentioned trap models can be used to describe defects withing organic materials. Such defect can be structural or energetic defects, or even both. However, these trap models can also be used to account for redox states. Organic materials have been shown to go through redox reactions [165]. These reactions involve transfer of electrons from (i.e. oxidation), or to (i.e. reduction) the host material. Organic electrochemical transistors (OECTs) that rely on transitioning between redox states, have been under investigation for biological applications [166]. According to a recent review on OECTs by Zeglio and Inganäs [167], changes in redox states of organic materials are associated with energy levels formed inside the band gap. These intermediate levels act as doping or de-doping centers when the device is operated under an external potential. This process can also be interpreted as charge carrier trapping and de-trapping, and the DD trap models can be used to account for these effects as well.

Therefore, if simulated traps are intended to represent defects, then Eqs. (4.2)-(4.3) stand. On the other hand, if they were to represent redox reactions, in this case both E_{t_n} and E_{t_p} in Eqs. (4.2)-(4.3) are simply replaced with E_{redox}. Furthermore, N_t would then represent the molecules (i.e. they are either reduced or oxidized). This effectively means that N_t has to be equal to N_0 from Eq. (4.1). Nevertheless, it might be possible that N_t be somewhat higher or lower. Eqs. (4.2)-(4.3) represent a classical description of the density. Conversely, in organics the description of the density is of a quantum mechanical nature. This is linked to the delocalization of the wavefunction, where molecules can be charged by a fractional charge (i.e. only a fraction of the quantum state is localized on a specific molecule). As a result, the density N_t can have values

which are both larger or smaller than the value of the molecular density N_0. In the presented simulation process, single trap levels are considered as a starting point, but if needed it is also possible to define a distribution of trap states with the Gaussian function from Eq. (4.1).

4.1.3 The mobility model

Describing how charges move within a transistor channel is an integral part of any DD simulation, and there are multiple models available to choose from[2]. Specific to organic semiconductors there are two models that are usually used for such investigations. An overview on both models is presented, and how the decision is taken on which one is applied moving forward with the simulations.

4.1.3.1 The Pasveer mobility

This mobility model which was developed by Pasveer *et al.* [168, 169], is obtained as a parametrical fit of numerical solutions of a system of master equations, implementing the Miller-Abrahams [170] hopping model between localized states with a Gaussian energy distribution. The model takes into account the dependence of the mobility on the temperature, charge density, and electric field:

$$\mu(T,\rho,F) = \mu\,(T,\rho)\,f(T,F) \tag{4.6a}$$

$$\mu(T,\rho) = \mu_0\,c_1 \exp\left[-c_2\left(\frac{\sigma}{k_bT}\right)^2\right] \exp\left[\frac{1}{2k_bT}\left(\frac{\sigma^2}{k_bT}-\sigma\right)\left(2\rho a^3\right)^{\delta}\right] \tag{4.6b}$$

$$f(T,F) = \exp\left\{0.44\left[\left(\frac{\sigma}{k_bT}\right)^{\frac{3}{2}}-2.2\right]\left[\sqrt{1+0.8\left(\frac{eFa}{\sigma}\right)^2}-1\right]\right\} \tag{4.6c}$$

$$\delta = 2\frac{log(s^2-s)-log(log4)}{s^2}, \qquad s=\frac{\sigma}{k_bT}, \qquad \mu_0=\frac{a^2\nu e}{\sigma} \tag{4.6d}$$

From Eqs. (4.6a)-(4.6d), ρ is the charge density, F the electric field, T the temperature, a the average distance between sites, σ the energetic disorder, ν_0 the attempt to jump frequency of the Miller-Abrahams model, c_1 =1.8×10^{-9} and c_2 =0.42 respectively. The Pasveer mobility has been used to fit experimental results for different semiconducting polymers [171, 172, 173]. Nevertheless, the authors also state that the above parameterization starts to breakdown at high electric fields, hence a cut-off has been defined where beyond it the breakdown occurs [172], and is given by

$$F > \frac{2\sigma}{ea} \tag{4.7}$$

4.1.3.2 The Poole-Frenkel mobility

According to Pasveer, at high electric field and beyond the cut-off mentioned above, the mobility starts to follow the Poole-Frenkel law (PF) [174]. The PF mobility model is a widely known and

[2]TiberCad is the simulation tool used for the presented DD investigation.

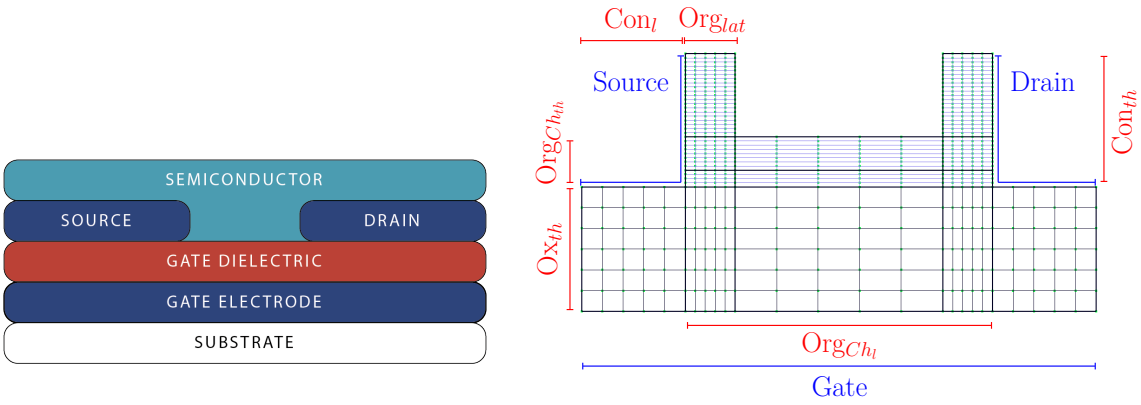

(a) Bottom-gate bottom-contact (BG-BC) **(b) 2D mesh representation**

Fig. 4.2: A 2D illustration of a bottom gate-bottom contact, in both **(a)** device and the corresponding **(b)** meshed representations. Dimension labels are illustrated and further explained in detail in the text.

used one in the literature for investigating charge transport in organic semiconductors [141, 175, 176, 177]. According to PF, the mobility is expressed as:

$$\mu = \mu_0 \exp\left(-\frac{\Delta - \gamma\sqrt{F}}{kT}\right) \tag{4.8}$$

where μ_0 is the zero-field mobility, Δ the zero-field activation energy, γ the Poole-Frenkel constant [178], and F the electric field, respectively. This relation specifies that charges can gain the required energy from the applied electric field to overcome potential barriers, as they hop from one site to another, equal to a certain activation energy that is otherwise not provided (or insufficient) thermally. Furthermore, as the mobility depends on both the temperature and applied field, the dependence on the temperature vanishes at the point of $F = (\Delta/\gamma)^2$. At this point, the applied field is equal to the activation energy so that at different temperatures the mobility will converge to the same value [175].

Both mobility models have been highlighted, as they serve different purposes. Deciding on which model to use for the DD simulations, depends on several aspects. The PF model better suits small molecules, while the numerical solution presented by Pasveer was mainly based on investigating polymers. Furthermore, if the DD model is used to investigate polymer based OFETs, a check of the condition specified by Eq. (4.7) is carried out. If the electric field is lower than the cutt-off, the Pasveer mobility is chosen. If not, the PF is then the one used.

4.2 Simulation and characterization of a pentacene OFET

4.2.1 Simulation related remarks

In this sub-section, some simulation related remarks are pointed out. A bottom gate-bottom contact (BG-BC) transistor architecture will be considered. A 2D illustration is shown in Fig. 4.2 in both device and meshed representations. The device is split up into two major regions, the oxide

Dimension Labels & Values	
Oxide Thickness (Ox_{th})	Defined by experiment
Channel Length (Org_{ch_l})	Defined by experiment
Channel Thickness ($Org_{ch_{th}}$)	10 nm
Organic Lateral Dimension (Org_{lat})	10 nm
Contact Length (Con_l)	50 nm
Contact Thickness (Con_{th})	100 nm

Table 4.1: The different dimension labels used to define the meshed structures and their assigned lengths.

and the organic respectively. The organic region itself is further split up into two regions, where the top part is the bulk, and the bottom part is used to model interface effects. In regards to the contacts, they are all defined as physical lines (i.e. boundaries) of the device. Bulk representation of the contacts are not taken into account, as they effectively do not change anything in terms of current-voltage characteristics. With this exclusion, improvements on simulations times is gained.

In regards to the dimensions, constructing the 2D meshed representation is based on the following device dimension labels: the oxide thickness (Ox_{th}), the channel length (Org_{ch_l}) and thickness ($Org_{ch_{th}}$), the lateral dimension of the organic near the contacts (Org_{lat}), and finally the contact length (Con_l) and thickness (Con_{th}). Only the Ox_{th} and Org_{ch_l} are changed with respect to experimental values, while the rest are pre-defined and are always fixed. A summary of these dimension labels are given in Table 4.1 (also shown in Fig. 4.2(b)). $Org_{ch_{th}}$ was chosen to be 10 nm, as it is well known that charge transport usually occurs within the first few monolayers just above the oxide-organic interface [119, 120]. Furthermore, simulation test runs on increased channel thickness did not show any change in the current-voltage characteristics going beyond this value. For the sake of being consistent, Org_{lat} was chosen to be the same as Org_{ch_l}. Similarly, Con_{th} was also fixed at 100 nm, as increasing the contact thickness simply increased simulation times without any observed changes in the characteristics.

The PF mobility model will be used for the simulation procedure, as pentacene (i.e. a small molecule) is the material of choice for the purpose of this investigation. Lastly, both the source and drain are modeled as Schottky contacts (typical for all organic based devices), unless there has been mention of doping near the source/drain. In the latter case the contacts would then be modeled as ohmic.

4.2.2 Trap-free Vs. fixed charges and interface/bulk traps

Organic materials often suffer from defects such as trap states, that affect device performance. Therefore, in order to successfully characterize and validate experimental data, it is important to have an understanding of effect of trap states on an OFET current-voltage (I-V) characteristics. Here the presence of fixed charges, interface traps, and bulk traps are studied, and how the I-V of a "pristine" device changes under their influence. Examining the transfer characteristics is useful for this purpose, as it provides a detailed picture in both the on-state (i.e. linear scale), as well as the off-state or sub-threshold regime (i.e. logarithmic scale).

Investigating the effect of negative fixed charges at the oxide-organic interface is first carried out

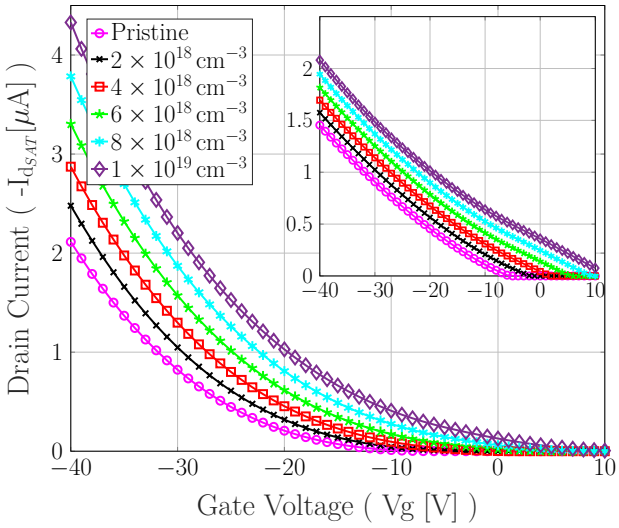

Fig. 4.3: The effect of fixed charges on the transfer characteristics of an OFET. The square root of the drain current versus the gate voltage ($\sqrt{Id_{SAT}}$ vs. V_g) is shown in the inset.

(will be referred to from now on as "**FC**)". From Fig. 4.3, it can be seen that a positive shift in the threshold voltage is induced transitioning from a "pristine" device towards higher concentrations of fixed charges. This behaviour follows the relation:

$$\Delta V_{th} = -\frac{Q_{int}}{C_{ox}} \tag{4.9}$$

where ΔV_{th} is the threshold voltage shift, Q_{int} the fixed charge concentration, and C_{ox} the oxide capacitance respectively. This ΔV_{th} is better depicted in the inset of Fig. 4.3 by plotting the square root of the drain current ($\sqrt{Id}$). The threshold voltage V_{th} is simply the intersection at the x-axis when the current is zero. An increase towards a more positive V_{th} can be clearly seen due to the increasing concentration of negative fixed charges. Conversly, and opposite shift would have been induced in the presence of positive fixed charges.

Following the inclusion of fixed interface charges, either interface or bulk traps can now be introduced. Traps are regarded neutral if empty, then either positively or negatively charged if occupied by a hole or an electron (will be referred to as "**ITH**" and "**ITE**" respectively). In regards to interface traps, a single trap level was chosen above the valence band. The effect of both types of charged traps, modeled at the oxide-organic interface, is depicted in Fig. 4.4(a,b). On one hand, positively charged traps leads to less current drive (i.e lower drain current and a downward shift in the transfer curve). This is true, as a higher gate voltage is required to induce more charges in the channel region. Conversely, negatively charged traps lead to a decrease in the inverse sub-threshold slope, and as a result a high sub-threshold current is evaluated, eventhough the transistor is operated at high positive gate voltages (i.e. in the off state). At high concentrations of electron traps, the positive applied gate voltage becomes insufficient to deplete the channel of holes leading to high currents in the off-state. Under negative applied gate voltages no change is observed in the drain current. This is self-evident, as in this voltage regime the channel is filled up with holes as mobile charges and trapped electron concentrations have no effect on the transfer characteristics. Furthermore, the negatively charged traps also lead to ΔV_{th} shifts (inset

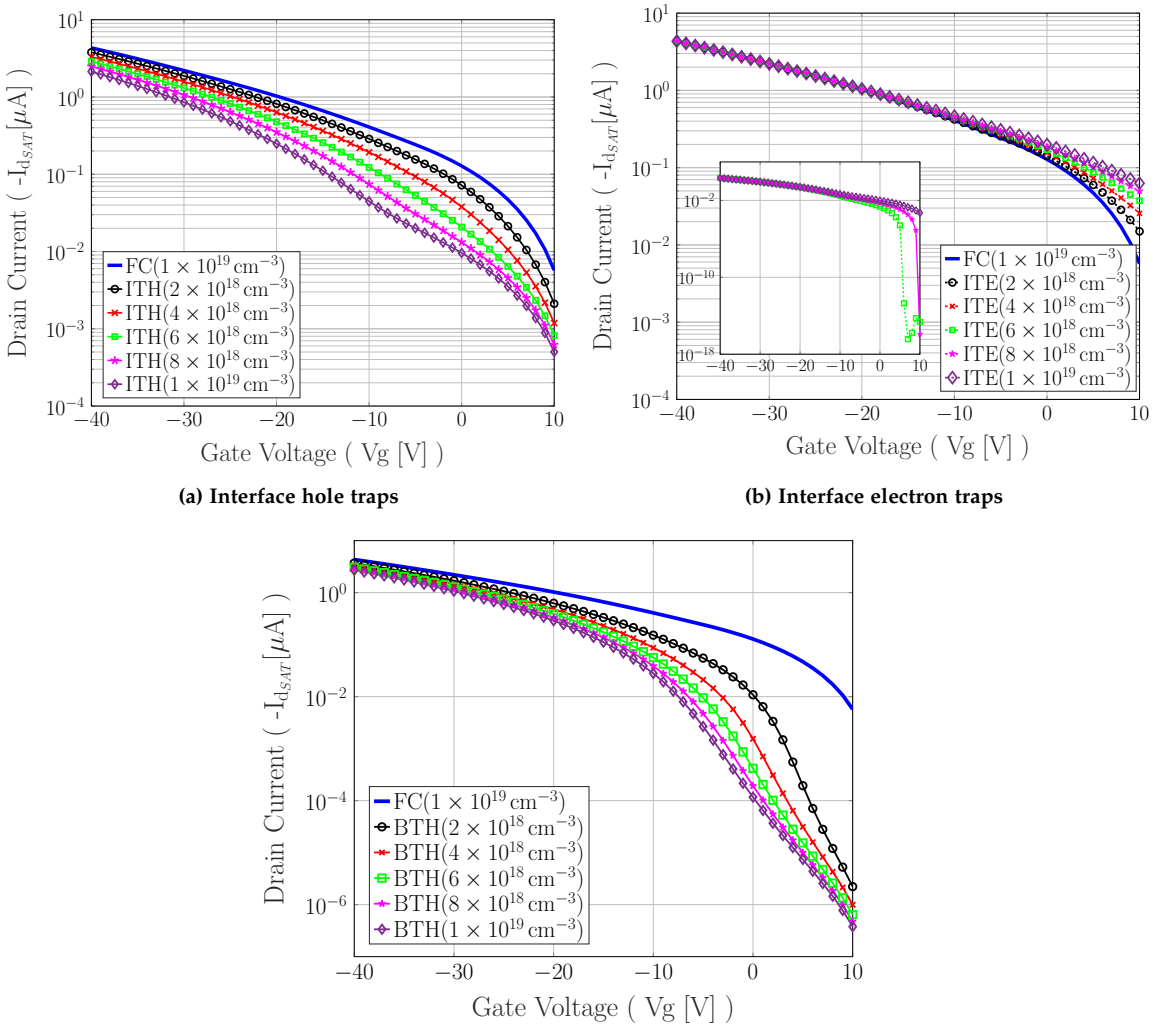

(a) Interface hole traps

(b) Interface electron traps

(c) Bulk hole traps

Fig. 4.4: Transfer Characteristics (at $V_d = -30$ V) of a BG-BC OFET under pristine conditions and different concentrations of interface and bulk traps. **(a)** The effect of positively charged (i.e. hole) interface traps. **(b)** The effect of negatively charged (i.e. electron) interface traps. **(c)** The effect of positively charged (i.e. hole) bulk traps.

of Fig. 4.4(b)) in the absence of fixed charges. This is not apparent in the main panel of Fig. 4.4(b) simply due to the already high presence of fixed charges as a starting point before the interface traps were applied.

Finally, the effect of positively charged bulk traps (will be referred to as "**BTH**") on the transistor performance with a single level above the valence band was investigated. As illustrated in Fig. 4.4(c), they also have a similar effect to that of the positively charged interface traps. Between bulk and interface traps, the former has a more pronounced effect on the inverse sub-threshold slope. This is a consequence of the bulk traps being located deeper in the band gap.

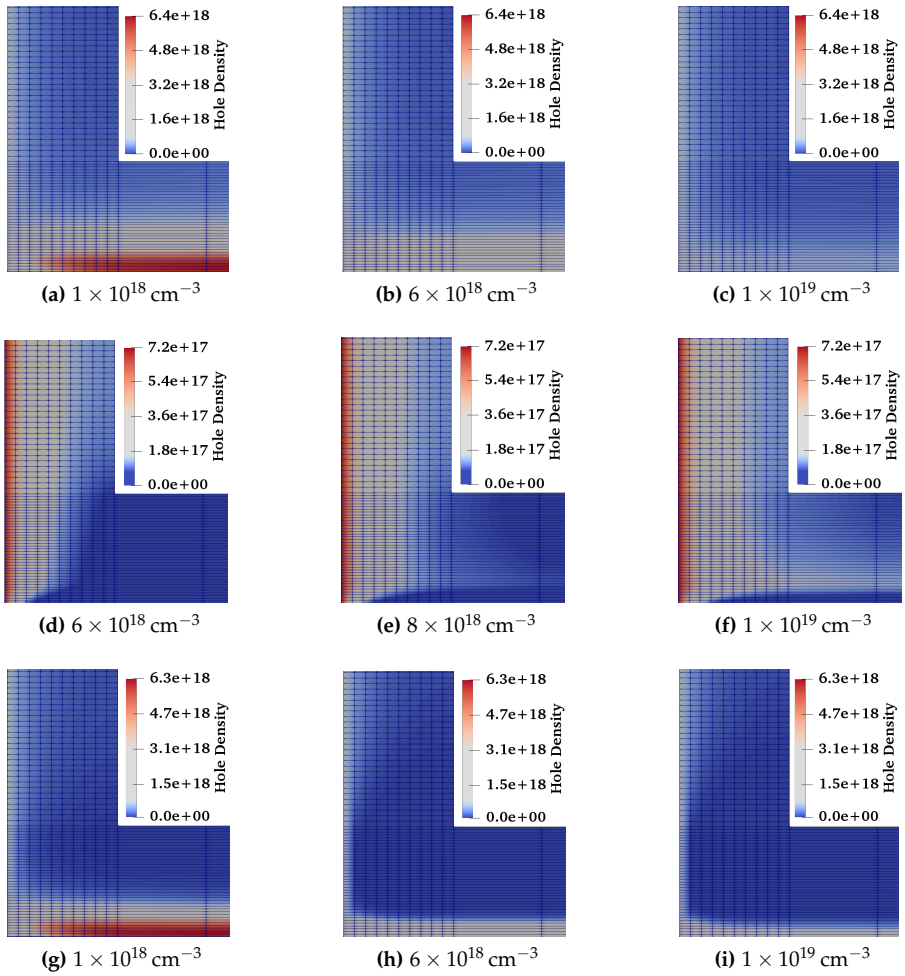

(a) $1 \times 10^{18}\,\mathrm{cm}^{-3}$ **(b)** $6 \times 10^{18}\,\mathrm{cm}^{-3}$ **(c)** $1 \times 10^{19}\,\mathrm{cm}^{-3}$

(d) $6 \times 10^{18}\,\mathrm{cm}^{-3}$ **(e)** $8 \times 10^{18}\,\mathrm{cm}^{-3}$ **(f)** $1 \times 10^{19}\,\mathrm{cm}^{-3}$

(g) $1 \times 10^{18}\,\mathrm{cm}^{-3}$ **(h)** $6 \times 10^{18}\,\mathrm{cm}^{-3}$ **(i)** $1 \times 10^{19}\,\mathrm{cm}^{-3}$

Fig. 4.5: Mobile charge density maps under the influence of **(a-c) ITH** between $1 \times 10^{18}\,\mathrm{cm}^{-3}$ - $1 \times 10^{19}\,\mathrm{cm}^{-3}$, **(d-f) ITE** between $6 \times 10^{18}\,\mathrm{cm}^{-3}$ - $1 \times 10^{19}\,\mathrm{cm}^{-3}$, and **(g-i) BTH** between $1 \times 10^{18}\,\mathrm{cm}^{-3}$ - $1 \times 10^{19}\,\mathrm{cm}^{-3}$.

Mobile charge density maps were also extracted for the different types of traps (see Fig. 4.5)[3]. As depicted in Fig. 4.5(a-c,g-i), the charge density decreases with higher concentrations of **ITH** and **BTH** respectively. Conversely, under the influence of **ITE** (Fig. 4.5(d-f)), the charge density slightly increases. From this analysis, it has been shown that fixed or trapped charges have their own distinct effects on the transfer characteristics of an organic transistor, but another crucial conclusion is that using either fixed charges alone[4] or as a combination with either interface or bulk traps might be insufficient to get a good description of the transfer curves. Possibly a combination between all three of them is required to achieve a good fit with the experimental results.

[3]Corresponding maps show the area of the channel region near the source contact.
[4]For the shown charge concentrations.

Simulation Parameters	
Site Density (N_0)	$4 \times 10^{19}\,\mathrm{cm}^{-3}$
Energetic disorder (σ)	30 meV
μ_0 **(PF)**	$3 \times 10^{-4}\,\mathrm{cm}^2/\mathrm{Vs}$
F **(PF)**	$3 \times 10^{5}\,\mathrm{V/cm}$
n_t/p_t **(Interface) Energy**	0.15 eV
p_t **(Bulk) Energy**	0.3 eV

Table 4.2: A summarized list of the different parameters used for the DD simulation of a pentacene BG-BC OFET.

4.2.3 Validating experimental data

Continuing on from the analysis presented in Sec. 4.2.2, this understanding can now be applied for the comparison with, and validation of experimental data. A study on a BG-BC pentacene OFET from Ref. [179], is selected for the validation process. Per the fabricated transistor, the channel length is 12 μm. The oxide thickness was not specified from the experiment, hence a typical thickness of 200 nm was chosen. The approach is taken, whereby fitting the transfer characteristics is achieved for a given set of parameters. This is followed by simulating the output characteristics using that same set. Following the analysis in Sec. 4.2.2, listed below are three possible scenarios to fit the transfer characteristics starting from a pristine condition, namely:

(i) The first scenario includes:
- Negative interface fixed charges, to get the correct V_{th}, and hence the slope of the transfer curve in the on-state.
- Positively charged bulk traps, to control the sub-threshold characteristics.
- **(If required)** Negatively charged interface traps, to have a more precise control over the sub-threshold slope.

(ii) The second scenario includes:
- Negative interface fixed charges, to get the correct V_{th}, and hence the slope of the transfer curve in the on-state.
- Positively charged interface traps, to get the appropriate evaluated current across the entire voltage range.
- **(If required)** Positively charged bulk traps, to control the sub-threshold characteristics.

(iii) The third scenario includes:
- Negatively charged interface traps, to get the correct V_{th} keeping in mind its added effect on the sub-threshold.
- Positively charged bulk traps to adjust the current drive accordingly.

From here onward the three scenarios mentioned above will be referred to in the same order as **SC1**, **SC2**, and **SC3** respectively. Simulation parameters used to describe the above scenarios (i.e.

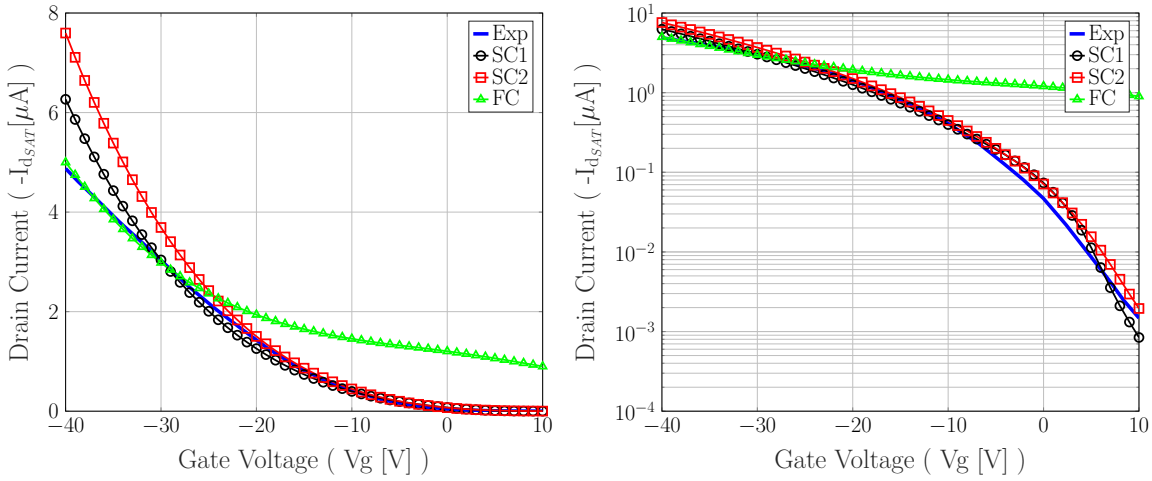

(a) Transfer char. (linear) **(b) Transfer char. (log)**

Fig. 4.6: Comparison between DD simulated results and experimental measurements (at V_d = −30 V) using the fitting scenarios on both the **(a)** linear and **(b)** logarithmic scales (i.e. for **SC1**, **SC2**, and **FC**).

fixed and trap concentrations) will be adjusted accordingly to reach the best fit of the transfer characteristics. All parameters are summarized in Table 4.2. From Table 4.2, all values referring to the μ_0, and interface or bulk trap energies are taken as input from the analysis carried out in [179]. These three parameters will also be carefully adjusted, if it is needed to do so, for the fitting process. The site density N_0, energetic disorder σ, and and electric field F are kept fixed.

All three scenarios were considered carefully. And within each one different concentrations for the fixed charges, interface and bulk traps (as well as their energy level) were investigated. Out of the proposed scenarios, no fit could be reproduced for the transfer characteristics with **SC3**. Using **SC1** or **SC2**, an almost perfect fit is achieved but only within a specific gate voltage range (between the off-state and up to −20 V of the applied gate voltage). The **SC1** and **SC2** fits are shown in Fig. 4.6(a,b), both on the linear and logarithmic scales. Beyond the −20 V mark both **SC1** and **SC2** drift away from the experimental measurement. By re-adjusting any (or all) of the three parameters within either **SC1** or **SC2**, it was only possible to fit the lower part of the transfer curve. This included different trap concentrations as well as their energy level within the band gap. Moreover, applying a GDOS in describing the trap energy as opposed to a single level definition did not improve the fitting process across the entire voltage range. The only way to fit the upper part of the transfer curve was actually using a fourth and different scenario, which involved only the presence of **FC** without the need for any of **ITH**, **ITE**, or **BTH**. The fit corresponding to only using **FC** is also shown in Fig. 4.6(a,b).

This approach concludes that the applied gate voltage range is split into two distinct regimes, where the lower regime is described by considering all of **FC**, **ITE** (from **SC1**) or **ITH** (from **SC2**), and **BTH**. While the upper regime is appropriately described using only **FC**. This conclusion can be further consolidated by looking back at the analysis illustrated in Fig. 4.4. Each of **ITE**, **ITH**, **BTH** only affect the transfer curves substantially in the sub-threshold regime and at low gate voltage in the on-state of the transistor. Possibly, **ITH** can somehow to a slightly larger extent affect the transfer curves at higher gate voltages compared to the other two, but even if **ITH** is

Final Fitting Scenarios			
Parameters	**"SC1"**	**"SC2"**	**"FC"**
FC	$1 \times 10^{19}\,\mathrm{cm}^{-3}$	$4 \times 10^{19}\,\mathrm{cm}^{-3}$	$3 \times 10^{19}\,\mathrm{cm}^{-3}$
ITH (Energy)	—	$6 \times 10^{19}\,\mathrm{cm}^{-3}$ (0.5 eV)	—
ITE (Energy)	$5 \times 10^{18}\,\mathrm{cm}^{-3}$ (0.2 eV)	—	—
BTH (Energy)	$8 \times 10^{17}\,\mathrm{cm}^{-3}$ (0.4 eV)	$7 \times 10^{18}\,\mathrm{cm}^{-3}$ (0.3 eV)	—
μ_0	$4.62 \times 10^{-4}\,\mathrm{cm}^2/\mathrm{Vs}$	$4.69 \times 10^{-4}\,\mathrm{cm}^2/\mathrm{Vs}$	$1.65 \times 10^{-4}\,\mathrm{cm}^2/\mathrm{Vs}$

Table 4.3: The final set of parameters used under each scenario to fit the experimental transfer characteristics in [179]. All other involved parameters remain unchanged.

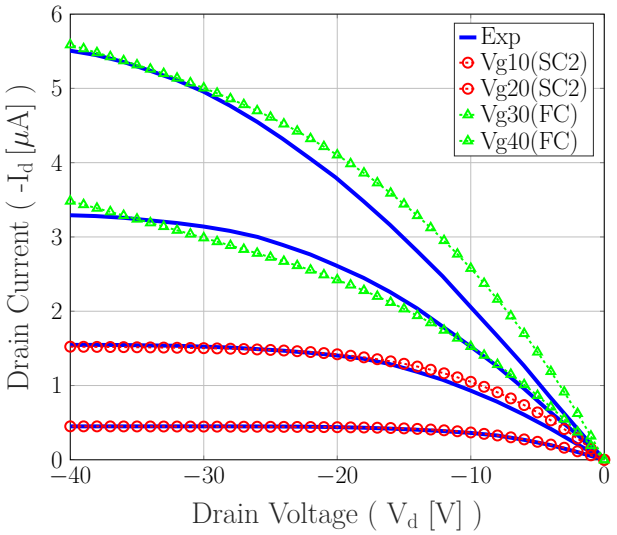

Fig. 4.7: Fitting of the output characteristics using scenarios **SC2** and **FC**.

either further increased in concentration, or the energy level shifted, this leads to losing any fitting in the lower regime of the gate voltage. At high gate voltages the effect of all three is greatly diminished, as all trapped interface and/or bulk charges are freed and join the mobile charges in the channel leading to higher evaluated drain currents. The final simulation parameters used to achieve these fits are summarized in Table 4.3. It is important to note that starting values for both the trap energies and the μ_0 had to be re-calibrated accordingly to reach the final fits.

After achieving a fit for the transfer curve, the output characteristics are now simulated and a comparison is drawn out between the simulated results and experimental measurements. As two scenarios were used for the fitting process (i.e **SC1**/**SC2** and **FC**), the same approach is taken for the output characteristics. Between **SC1** and **SC2**, the latter is chosen to simulate the lower regime of the gate voltage. **FC** was used to simulate the upper regime respectively. Final output characteristics using **SC2** and **FC** are depicted in Fig. 4.7. Quite clearly, with **SC2** a perfect match is successfully reproduced for gate voltages of $-10\,\mathrm{V}$ and $-20\,\mathrm{V}$. Using **FC** to simulate gate voltages of $-30\,\mathrm{V}$ and $-40\,\mathrm{V}$ did not yield a perfect fit but was still able to reproduce the correct

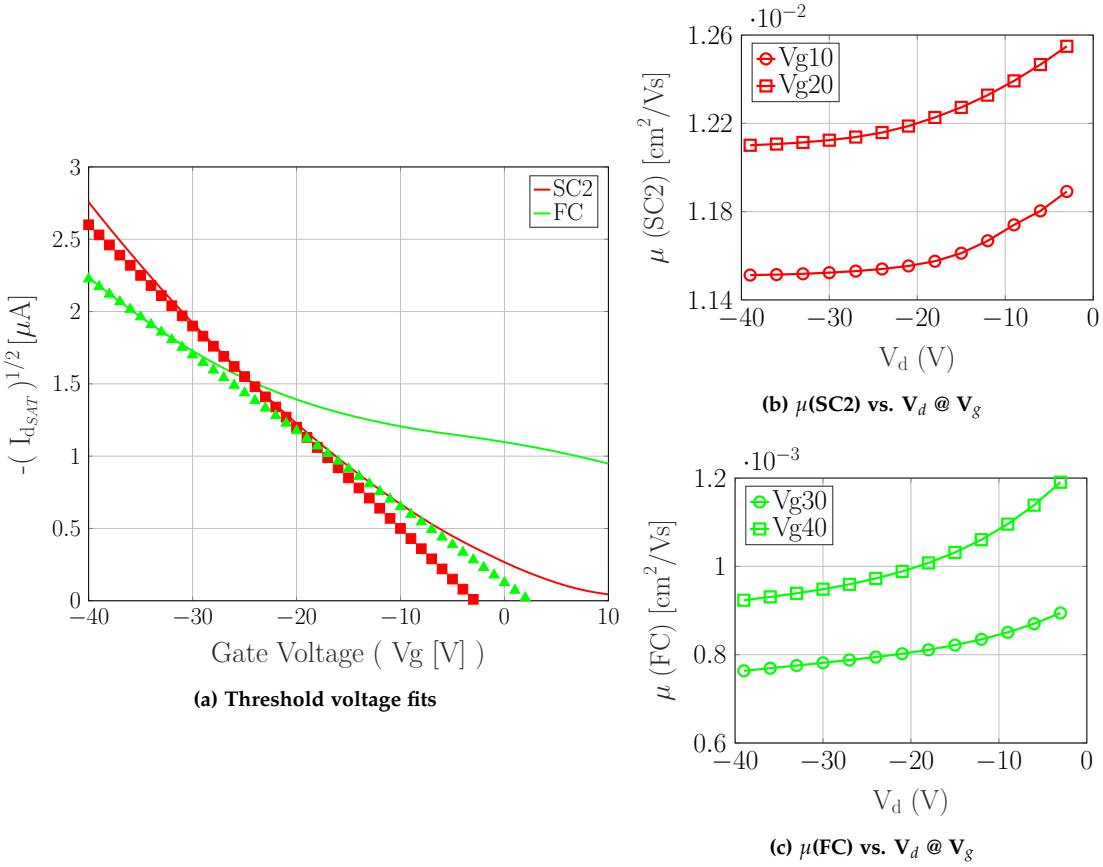

(a) Threshold voltage fits

(b) μ(SC2) vs. V_d @ V_g

(c) μ(FC) vs. V_d @ V_g

Fig. 4.8: (a) Extraction of device threshold voltage. Mobility dependence on the drain voltage V_d at different gate voltages V_g, using **(b) SC2** and **(c) FC**.

behaviour in both the linear and saturation regimes as well as the highest evaluated current respectively.

4.2.4 Extracting performance parameters

A crucial part of this investigation, is once an agreement is achieved between the simulation and experimental results, the important performance parameters can be extracted. These parameters include both the V_{th} and the effective μ of the device in question. Naturally, based on the results presented in the previous sub-section extracting one value for each is not possible. This is due to the fact that there are two gate voltage regimes described by two different fitting parameterizations. Hence, when coming to extract both V_{th} and μ, this depends on the operating conditions of the device. If it is to be operated at low gate voltages then parameterization **SC2** is used, and vise versa **FC** is used if the device is operated at high gate voltages. In extracting V_{th}, Fig. 4.8(a) shows the $\sqrt{Id}$ vs. Vg relation. At the lower regime (i.e. using **SC2**), V_{th}=−2.8 V, conversely at the higher regime (i.e using **FC**) V_{th}=+2.35 V. The latter coincides with the experimental value. But this difference in V_{th} between high and low operating regimes is a consequence of the fixed charges and/or interface (bulk) traps. In the low regime V_{th} highly depends on the interface and bulk traps, therefore a larger negative voltage is required to switch on the device. In the high

regime, it is rather is solely controlled by the fixed charges present and it is shifted towards a more positive value.

A similar approach is taken in extracting the effective μ, and this could easily be done by finding the slope of the linear fits from Fig. 4.8(a). Nevertheless, μ is a rather complex performance parameter that depends on several factors including the temperature, charge density, and the applied voltage (or electric field). It's dependence on the latter was of particular interest, and is obtained by extracting the mobility dependence on the drain voltage (μ vs. V_d @ V_g). These dependencies are illustrated in Fig. 4.8(b,c), and as it can be seen the mobility decreases (rather slightly) transitioning from the linear to the saturation regime. Using **SC2**, the mobility lies between $1.14 \times 10^{-2}\,\mathrm{cm}^2/\mathrm{Vs}$ – $1.26 \times 10^{-2}\,\mathrm{cm}^2/\mathrm{Vs}$, and using **FC** it lies between $7 \times 10^{-4}\,\mathrm{cm}^2/\mathrm{Vs}$ – $1.2 \times 10^{-3}\,\mathrm{cm}^2/\mathrm{Vs}$. Once again with **FC** the estimated mobility is closer to the experimental value of $4 \times 10^{-3}\,\mathrm{cm}^2/\mathrm{Vs}$.

4.3 Conclusions

A drift-diffusion model for the investigation and characterization of OFETs was presented. This model included the GDOS taking into consideration the site density and energetic disorder commonly associated with organic materials, as well as the PF mobility for small molecules (the hopping mobility for polymers). The effects of fixed charges, interface traps and bulk traps (i.e. on the transfer characteristics) were investigated individually. Extending this analysis for the comparison with experimental measurements, it was concluded that more than one scenario is required to achieve a good fit depending on the device operating conditions. Eventhough fixed charges are present, the effect of both interface and bulk traps were found to be significant at low gate voltages. Conversely, the current-voltage characteristics are well described with the influence of fixed charges alone at high gate voltages. This was followed by the extraction of transistor performance parameters.

Chapter 5

On the device scale

This chapter provides an in depth analysis in quantifying low conductance regions in organic field effect transistors (OFETs). The investigation is carried out on the circuit level from a theoretical perspective (i.e. the furthest point moving upwards the dimension scale). The experimental procedure and it's working principle are highlighted, as well as it's different uses described in detail (Sec. 5.1), including the focused-on approach (Sec. 5.2). This is followed by presenting the model used to interpret, validate, and add to experimental findings, aiming towards achieving a greater understanding of defective regions in OFETs (Sec. 5.3). In Sec. 5.4, simulation results are discussed, illustrating why such a model utilizing circuit based components (i.e resistors in this case) is useful for similar investigations. Sec. 5.5 ends this chapter with a conclusion of this study

The results reported in this chapter are published in Ref. [180], and are reprinted with permission. The published work was a collaborative effort with the group of Prof. Bert Nickel at the Faculty of Physics and Center for NanoScience at Ludwig-Maximillians Universität (LMU).

5.1 Scanning photo-current microscopy

Over the years, different microscopy techniques have been used in studying semiconductors, both organics and inorganic materials. These techniques have come to uncover vast amounts of information on structural morphology, and charge transport dynamics. Some famous examples include atomic force microscopy (AFM), and scanning tunneling microscopy (STM). Scanning photo-current microscopy (SPCM) also lies within the same family. In contrast to AFM or STM which utilize physical probes on samples of interest, SPCM relies on scanning the surface of an organic thin film with sub-micron precision, where a laser light is shone onto a specific spot along the length of the film with a certain wavelength. Fig. 5.1 shows a simplified schematic of the SPCM measurement setup. Through this illumination process, charges can be injected and/or excited from within the material and start to flow under the applied electric field. Given that these charges do not recombine, they reach the electrodes in the form of a measured photo-current. This provides a correlation between structural properties and performance measures of devices. Reflected light is used to draw out maps providing a spatially resolved image representing the strength of the photo-currents. Moreover, the extracted information can be attributed to local spots along the semiconducting film.

SPCM have been already used for a variety of different investigations on OFETs. Some of these examples are listed below:

1. Identifying and differentiating between various photo-response mechanisms in OFETs
    - Different mechanisms include photo-voltaic (PV) and photothermo-electric (PTE) effects. It is important to separate the occurrence of such mechanisms for the optimization

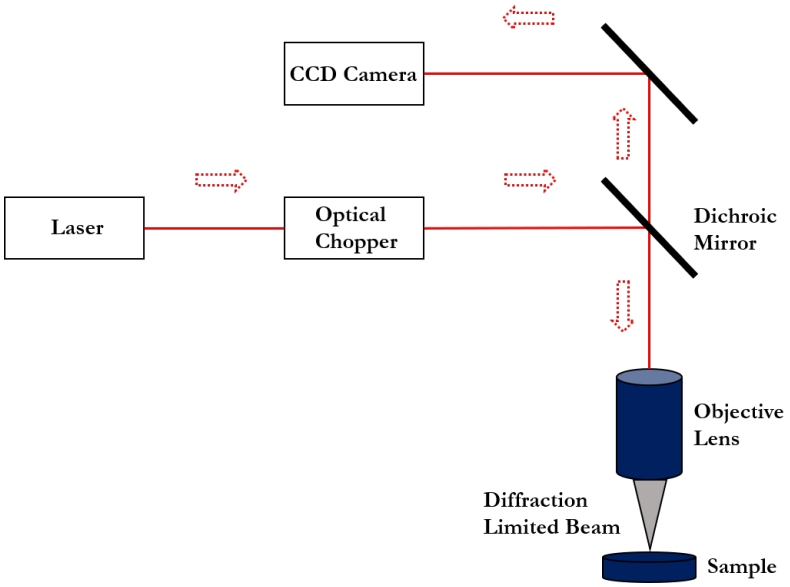

Fig. 5.1: Schematic diagram of the SPCM setup.

of photo-detectors. Molybdenum disulfide (MoS_2) based OFETs have been used for such investigations, as it has been reported that they exhibit these mechanisms [181, 182]. Wu *et al.* [183], using SPCM, have shown that measured photo-currents are dominated by field assisted separation of photo-excited carriers under both moderate and high applied biases, in contrast to PTE effects observed at zero bias. Furthermore, varying the thickness of MoS_2, time-resolved photo-response showed that measured rise times of the photo-currents where in the range of microseconds, much faster than timescales of thermal effects (i.e. milliseconds to seconds [184, 185]). As a result, photo-excited carriers do not have the sufficient time to reach thermal equilibrium with the lattice. Sun *et al.* [186] observed a similar behavior in graphene devices, where they were able to isolate contributions between PV and PTE effects.

2. Band-offsets at single-layer and multi-layer MoS_2 junctions

   - MoS_2 is known to have a structural topology of 2-dimensional (2D) layers. Moreover, single-layer (SL) and multi-layer (ML) MoS_2 exhibit direct and indirect band gaps of different sizes [187, 188] respectively. This leads to a formation of heterojuctions between adjacent layers of varied thickness. It is therefore crucial to investigate band-offsets at these junctions, towards the successful engineering of optoelectronic devices [189, 190, 191, 192]. SPCM is an appropriate tool to identify these band-offsets and their effect on device performance. Howell *et. al* [193] applied a strategy, where SPCM was used to extract a qualitative and quantitative photo-response of uniform thickness MoS_2 FETs. This is followed by finite element modeling to fit the measured photo-currents based on a set of parameters including carrier concentrations and electron affinities. These parameters would then be used to identify the type of alignment between SLs and MLs, and subsequent electrical characterization of MoS_2 heterojuction FETs.

3. Spatial Mapping of efficiency of nanowire array solar cell
    - Non-planar heterostructures have been proposed as an alternative to enhance solar cell performance [194, 195]. Nanowire arrays have been investigated as proposed novel architectures. Nevertheless, in contrast to planar devices, such architectures present a challenge, where structural variations within fabricated arrays has a direct effect on quantum efficiency. Howell *et al.* [196] presented a study on Gallium-Nitride/Indium-Gallium-Nitride (GaN/InGaN) nanowire array solar cells, providing an in-depth understanding behind this correlation. Utilitzing SPCM, they evaluated the external quantum efficiency (EQE) from the ratio between the the collected charges of the measured photocurrents, and the amount of incident photons. Within the fabricated devices, there were ordered arrays of nanowires interrupted with what they refer to as gaps and plateaus. SPCM images showed highest photocurrents and corresponding EQEs in the gap regions, followed by the arrays, and lowest at the plateaus. Furthermore, they carried out finite difference time domain simulations (FDTD), where they illuminated the device at 3 different locations. Namely, centered on a nanowire, centered between adjacent nanowires, and centered within a gap. Total absorption was found to be the same at all 3 location. To explain the variation of the EQE recorded from the SPCM measurements, they concluded that this is due to variations in the internal quantum efficiency (IQE), as a result of increased absorption by the sides of adjacent nanowires as compared to the top or underlying substrate. From this analysis, one can gain valuable information towards improved device processing. In this case, optimization of the pitch an height on the nanowire array.

5.2 Quantifying low conductance regions in OFETs

In the previous section, some examples in which SPCM has been used were briefly introduced. A common occurrence between the aforementioned examples and what will be discussed further, is the application of theoretical simulation models. SPCM on it's own simply provides a picture of a varying intensity of photocurrents, but accompanying simulations can be useful as they provide a much wider understanding of experimental measurements, both quantitatively and qualitatively. Here, the focus turns on the presented work of quantifying low conductance regions in OFETs based on SPCM measurements, from a theoretical perspective.

In simple terms, any OFET must exhibit and maintain good performance measures. These measures are high charge carrier mobilities, low operating voltages, and device stability. With all the promise that they have shown, there still are factors that limit their usage on a large commercial scale. One of these factors is the presence of ineffective regions within the channel of a device. These regions act as defects that limit device performance in terms of the measures mentioned previously and can originate from several sources (i.e. structural or energetic defects). Furthermore, this might lead to charge carrier trapping. To this day, most measurements taken from OFETs are usually done in either ambient atmosphere for shorts periods of time or inside vacuum chambers. Prolonged operation under ambient atmosphere typically leads to performance degradation. One famous example is oxidized pentacene species, where oxygen atoms bond with the pentacene central rings leading to the formation of traps states within the band gap [197, 198]. Furthermore, OFETs are not made up of only organic materials (eventhough efforts have been made to achieve exactly that). Other materials include metals (i.e. for the source and drain contacts) and inorganic oxides. Therefore, interface quality has a large effect on how OFETs

perform. Charge transport in organic materials commonly occurs within the first few monolayers at the organic-oxide interface [119, 120], hence careful consideration must be taken into account as to which materials should be chosen for optimum device performance.

The aforementioned sources of traps states in organic materials are a consequence of the fabrication procedure or the operating conditions. But a major source of traps states in organic semiconductors relates to their nature (i.e. they are inherently present). This highly depends on the partial localization of quantum states in space, due to energy and spatial disorder. Consequently, a broadening of the energy levels in the density of states is generated as a result of such disorder. This is described by Bässler [140] as the Gaussian Disorder Model (GDM) (i.e. see Sec. 5.1.1). With higher energetic disorder, the tail of the Gaussian distribution will extend into the band gap. As the charge transport in organics often relies on hopping from one site to the next, a certain amount of these sites will act as trap states.

As far as how traps affect device performance, this highly depends on their position relative to the transport level. There are two different classifications of traps, shallow and deep traps respectively. Both have very different effects on OFETs. Shallow traps target charge carrier mobilities [142, 150, 151]. Charges are momentarily trapped as they travel from the source to the drain. Such an effect is outlined by the multiple trap and release model (MTR) [141, 199]. This model takes into consideration the amount of time a certain charge spends trapped as well as the time it takes to travel between traps. If charges are trapped for longer periods of time, this leads to hysteresis when switching from forward to backward biases [142, 152]. MTR is usually applied to organics being more crytalline than amorphous because they have both localized and delocalized states. This leads to a transition from localized to delocalized levels, hence transport becomes based on multi-trapping and releasing of charges. On the other hand, deep traps lead to threshold voltage shifts and the need for higher operating voltages [153, 154]. This is obvious since more energy is required to free charges to participate in transport. For all these reasons, it is crucial to locate and quantify defective regions in organic based devices. This requires extracting possible low conductive regions for subsequent analysis of the identified areas (e.g. identifying polymorphs as a potential source of traps states [200]).

Pentacene OFETs are the subject of this investigation. Using SPCM, the laser light is shone onto a specific spot along the length of the film with a certain wavelength (see Fig. 5.2(a)). Under this illumination, charges at that location gain the required energy to become de-trapped and start flowing in the direction of the electric field applied between the source and drain contacts. In pentacene, the de-trapping is governed by the reaction of the prevalent triplet excitons [201, 202] with trapped charges [203, 204]. With such a setup, the photo-response current can be measured and a map can be drawn to show the strength of the current difference (i.e between pre- and post- illumination) with respect to the illuminated spot. In this fashion, defective regions are identified. Previous experimental SPCM studies of pentacene transistors showed inhomogeneous SPCM maps, which were explained with an inhomogeneous trap distribution, revealed by exciton-assisted de-trapping [203, 205, 206].

According to the Thevenin theorem, any complex network of resistors can be simplified to an equivalent circuit with just one resistor. In this investigation, the equivalent simplified network is determined (i.e. the current before and after illumination), as shown in Fig. 5.2(b). Here the addressed question is, to which extent does the total current change still contains information of the local resistance change. The proposed simulation model (introduced in the following section) will be used to answer this question, and further evaluate the density of traps. The latter being a quantity SPCM cannot measure first hand.

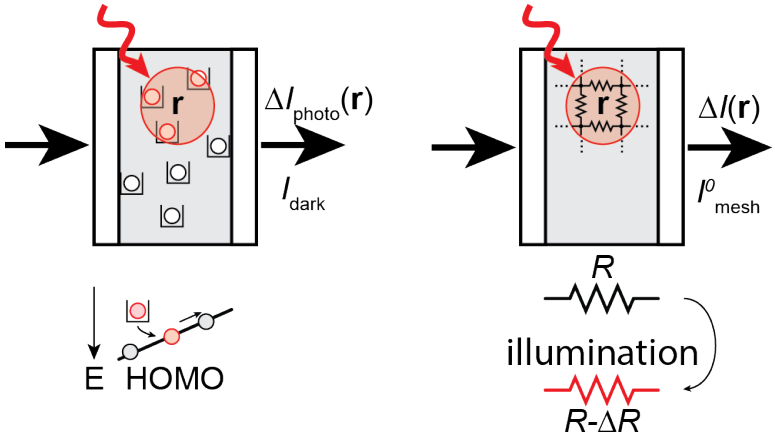

Fig. 5.2: Left panel: Illustration of the SPCM measurement technique. **Right panel:** It's circuit equivalent based on a network of resistors. The organic film is illuminated by a laser light (block resistances manipulated) focusing on sub-micron sized spots. As a consequence of this illumination (manipulation) charges are de-trapped and the photo-current is measured.

5.3 From SPCM to resistor networks

5.3.1 The theoretical model

The simulation model is based on a theory of resistor networks presented in [207]. It is important to begin by noting that investigations of transistor operations using circuit elements has been proposed before by Shockley [14] and Brews [208] (i.e charge sheet model). More recently, such models have also been extended to investigate both organic and inorganic ambipolar transistors [209, 210, 211]. Here we start by considering a two dimensional resistance network with N nodes numbered $i = 1, 2, , 3, ..., N$ respectively (as shown in Fig. 5.3). The conductance between two neighboring nodes is given by $c_{ij} = {r_{ij}}^{-1} = c_{ji}$, and according to Kirchhoff's law

$$\sum_{j=1}^{N}{}' c_{ij}(V_i - V_j) = {I_i}^1, \qquad i = 1, 2, 3, ..., N \tag{5.1}$$

where I and V are the current and voltage respectively. Eq. (5.1) can be rewritten in the following form:

$$L\overrightarrow{V} = \overrightarrow{I} \tag{5.2}$$

From Eq. (5.2), L is defined as a conductance matrix (referred to as the "Laplacian" matrix in [207]). The off diagonal elements of this matrix correspond to the conductance between a pair of nodes. It also should be noted that this matrix is an adjacency matrix, which means if there is no resistor present between nodes i and j, the conductance is equal to zero. The final representation of the conductance matrix is

[1] the prime stands for the omission of the term $j = i$

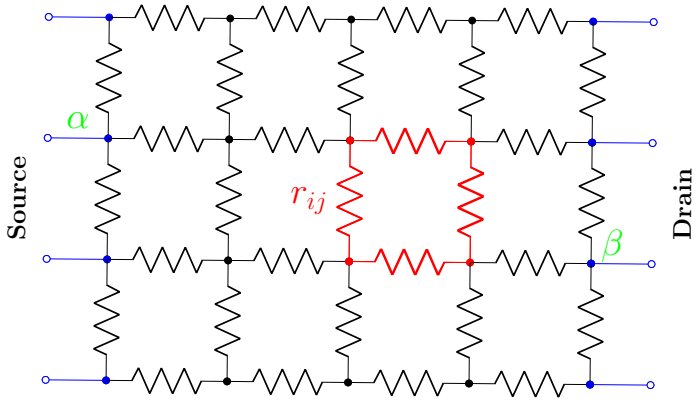

Fig. 5.3: A simple schematic of a 2D resistor network. The block highlighted in red represents a single spot. Letters i and j represent the position of an individual resistor, while α and β denote the chosen nodes for which the network resistance is calculated between them.

$$L = \begin{pmatrix} c_{11} & -c_{12} & \cdots & -c_{1N} \\ -c_{21} & c_{22} & \cdots & -c_{2N} \\ \vdots & \vdots & \ddots & \vdots \\ -c_{N1} & -c_{N2} & \cdots & c_{NN} \end{pmatrix} \tag{5.3a}$$

$$L\Psi_i = \lambda_i \Psi_i \qquad i = 1, 2, 3, ..., N \tag{5.3b}$$

where Ψ_i and λ_i are the eigenvectors and eigenvalues of the conductance matrix respectively. Using Eqs. (5.1)-(5.3), one can calculate the overall resistance between two arbitrary nodes α and β with the following expression:

$$R_{\alpha\beta} = \sum_{i=2}^{N} \frac{1}{\lambda_i} \left| \Psi_{i\alpha} - \Psi_{i\beta} \right|^2 \tag{5.4}$$

As the sum of all columns/rows are equal to zero, one of the eigenvalues is zero. This is usually the first eigenvalue (i.e at $i = 1$), that is why the summation in Eq. (5.4) goes from $i = 2$ to N. Care should also be taken when differentiating the usage of i, j, α, and β since they all represent the same entity (i.e nodes). Variables i and j are referred to when constructing the network and consequently the conductance matrix. On the other hand, α and β represent two nodes that have been chosen, and the resistance of the network is calculated with respect to them (see Fig. 5.3). Therefore, the lowercase r are the values for the individual resistances between the nodes within the network. The uppercase R refers to the resistance of the entire network between two specific nodes. Such reference will stay the same from here onward. Each block inside the network consists of four resistors r and hence represents a spot to be "illuminated". Once a spot has been chosen (at random or otherwise), all four resistors are changed accordingly. This change is applied through the relation between the carrier density and resistance given in Eqs. (5.5a)-(5.5b).

The carrier density is raised to a specific value which provides four new resistances r assigned to a block. In this way, it is possible to mimic the effect of the illumination process onto a specific spot. Pre- and post-illuminated block resistances are always calculated in this fashion.

$$r = \rho \, \frac{l}{wt} \tag{5.5a}$$

$$\rho = \frac{1}{eq\mu_{(p/n)}} \tag{5.5b}$$

where,

a) ρ is the resistivity of the organic semiconductor.

b) l, w, t are the length, width, and thickness of the spot size.

c) e is the electronic charge.

d) q is the charge carrier density (main simulation parameter).

e) $\mu_{(p/n)}$ is the charge carrier mobility.

Once the manipulation process is complete, the new conductance matrix built, and the final network resistance calculated, a voltage is applied across the channel to calculate the "photo-response" current using Eq. (5.2). It should be taken into consideration that all nodes on both the source and drain sides must be at the same potential assigned to them (i.e ground on the source, a voltage V on the drain). With that in mind, this insures that the current entering from any node on the source will have all possible pathways available to choose from in reaching the drain. This dictates how the conductance matrix is set up.

5.3.2 Model validation

The simulation process begins by validating the model to ensure that its functionality is sound. Two approaches have been chosen for this validation. The first one will be simulating a homogeneous network. This means that all block resistances r are assigned the same initial value. The entire network is then manipulated block by block in a sequential manner, and a color map of the network is drawn at the end. As the network is homogeneous and the manipulation process (i.e increasing the carrier density) is the same for every block, it should be expected that "sister" blocks (i.e. same distance from the edges but on opposite sides) will result in the same photo-response current and consequently the same current difference. That is indeed the case, as illustrated by the color map in Fig. 5.4(a) which shows horizontal and vertical symmetry. One important observation, is how the difference between the "dark" current and the photo-response current (in terms of current density) increases towards the contact edges in contrast to the central region of the channel. However this does not affect the symmetry. More on this observation will be discussed in detail in the following section, where simulation and experimental results are compared.

With the previous approach the entire network was scanned block by block. In the second approach, the aim to manipulate specific blocks that were identified beforehand in order to draw out a certain image. The image of choice in this case was a university logo. From Fig. 5.4(b), it can be seen that the initials are visible and clearly readable. The intensity is slightly different across

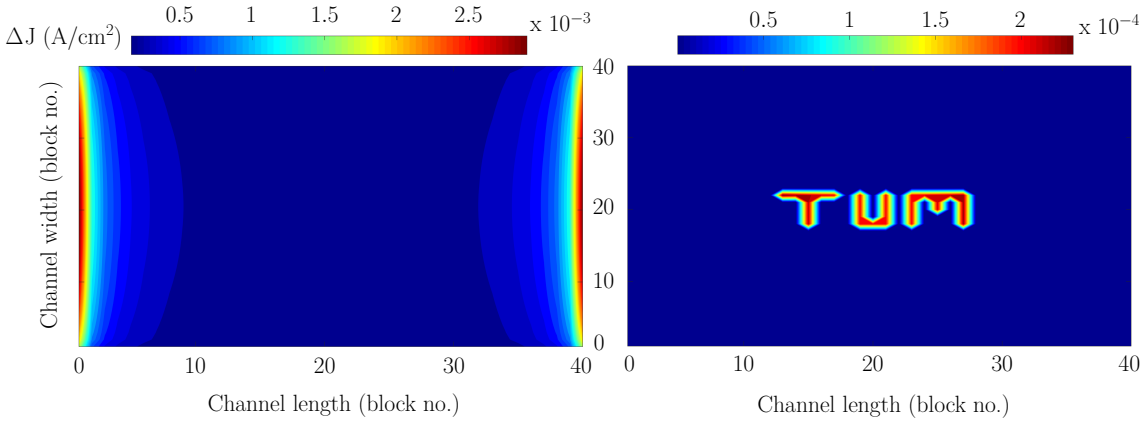

(a) Homogeneous network **(b) TUM logo**

Fig. 5.4: (a) A color map representation of the manipulation process of a homogeneous network. During the manipulation process, each block was returned to it's initial state before moving to the next one. Symmetry is present (taken either horizontally or vertically) meaning that "sister" blocks on opposite sides give the same intensity. **(b)** Illustration of the "TUM" logo. Specific blocks were chosen and manipulated to draw this image

the logo as this depends on the position of the block in question. Pre-illumination current and charge densities were $0.28\,\mathrm{A/cm^2}$ and $10^{14}\,\mathrm{cm^{-3}}$, with post illumination densities are $10^{17}\,\mathrm{cm^{-3}}$ respectively. This provides adequate proof that the model responds well to a predefined input, giving the expected output. Furthermore, this allows extraction local properties of the network (i.e. effect of specific positions with respect to the entire network).

5.4 Simulation vs. experimental: a comparison

In terms of running the model to compare simulation and experimental results, a few changes need to applied to that of the validation procedure. Firstly, charge densities are not homogeneously distributed across the transistor channel. Hence, for a more realistic approach the network in question must be of an inhomogeneous nature. This has been done by providing the model with a range of charge densities, to both choose from and assign individual resistances in a random fashion. Furthermore, results of this model are to be compared with that of an OFET. It is therefore crucial that the network is operating under the same conditions similar to an OFET in order to have a justifiable comparison. In addition to the random assignment of charges across the network, both the effects of the gate and the drain-source must be implemented. For the former, this is done implicitly, as for the latter it is explicitly addressed.

In an OFET, the gate is responsible for inducing charges inside the channel. This attribute is added by providing the network with a specific value for the charge density. A Gaussian distribution with a pre-defined standard deviation is centered around this value. For the drain-source effect, it is assumed that the charge density across the channel should decrease linearly moving from the source towards the drain. Here the network is divided into multiple segments, where a set of values corresponding to the charge densities are assigned to each segment (based on the standard deviation of the Gaussian distribution). The distribution is then simply shifted to a lower value while maintaining the same standard deviation. This is repeated from one segment

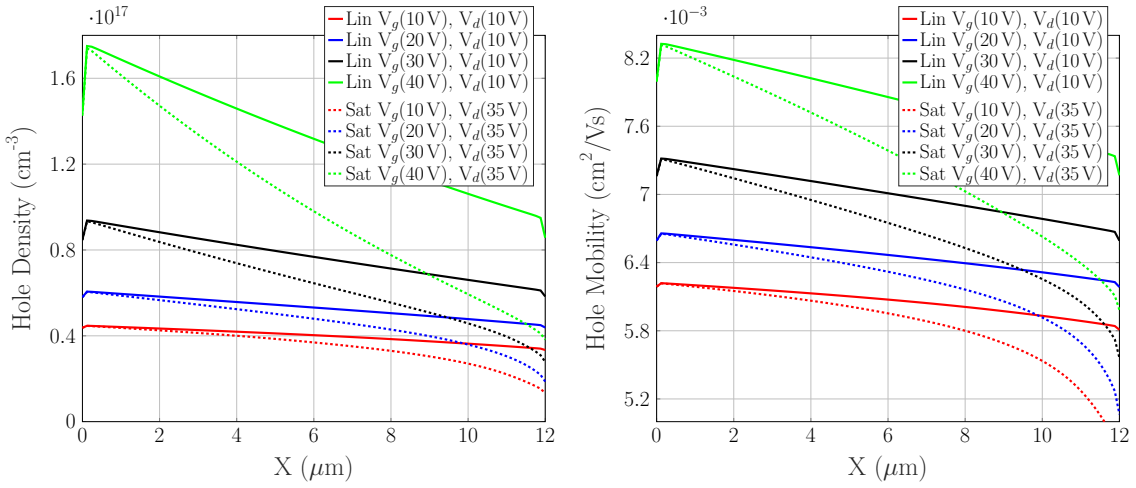

(a) Hole density profile **(b) Hole mobility profile**

Fig. 5.5: Charge **(a)** density and **(b)** mobility profiles in a pentacene OFET, as simulated by DD at different operating conditions.

Simulation Parameters	
Channel Length	$20\,\mu$m
Channel Width	$20\,\mu$m
Channel Thickness	2 nm
Spot Size	500 nm × 500 nm
Charge Density	$1.15 \times 10^{17}\,\mathrm{cm}^{-3} - 1.35 \times 10^{17}\,\mathrm{cm}^{-3}$
Carrier Mobility	$6.5 \times 10^{-3}\,\mathrm{cm}^2/\mathrm{Vs}$

Table 5.1: Summary of the parameters used for the simulation of a pentacene OFET

to the next. To insure that these assumptions are correct, a drift-diffusion (DD) simulation was carried out on a bottom gate/bottom contact pentacene OFET, and the density profile across the channel region was extracted and plotted. This profile is shown in Fig. 5.5(a). A linear drop is clearly observed, hence consolidating the approach described earlier. Nevertheless, closer to the drain contact the density profile deviates from this linear behavior. More on this aspect with be discussed shortly. To summarize, in this fashion OFET operating conditions are considered by implicitly include the gate effect (i.e. charge density value based on a Gaussian distribution), the linear decrease in density due to the explicit drain-source effect (i.e. shifting the distribution accordingly), and finally the inhomogeneity of charge density assignment based on the given standard deviation.

Results presented here will be based on a pentacene OFET, but the model can be generally applied to other materials by properly adjusting the parameters. The parameters used for the simulation procedure are summarized in Table 5.1. The operating point of the network is at a gate voltage of 20 V and drain-source voltage of 10 V respectively (i.e. solid blue line in Fig. 5.5).

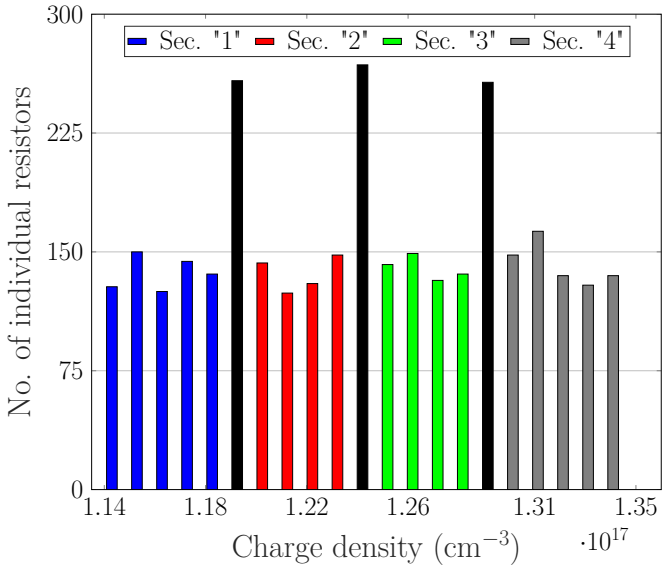

Fig. 5.6: Bar chart showing the distribution of the charge carrier densities and corresponding number of resistors across the four sections of the network. Densities are more or less fairly distributed, except three values which are shared between two adjacent sections highlighted by the black bars.

For the used charge density range, a total of 24 values were chosen to cover the entire range, 6 for each segment in decreasing order. This ensures the linear drop across the channel is present. To find out how the charge densities are assigned to the network, their corresponding number of individual resistances were extracted (i.e for each segment). Fig. 5.6 shows this assignment, and indicates that all values (i.e charge densities) given to a specific segment of the network are more or less evenly distributed. Only three values are higher as they are common between two adjacent segments. The network was divided into four segments.

Now that the model has been appropriately adjusted, the entire network will be manipulated block by block. In this manner the positions which contribute to the highest (and lowest) photo-response current and hence the corresponding defective regions are identified. The resulting color map is depicted in Fig. 5.7(a). The principle of SPCM and the model used is based on the effect of illumination which triggers the de-trapping mechanism at a specific spot, therefore identifying a local effect relating a certain density of traps to a specific location in the transistor channel. Similar to SPCM, the simulated maps can be used to interpret these low conductive (i.e. defective) regions in terms of traps densities. A recurring observation from Figs. 5.4(a) and 5.7(a) is the rather large difference in current density near the contact edges. This raises the question, is what being observed near the contact edges a local effect that de-trapping is much more significant there in contrast to the central region, or is it a global effect due to the close proximity to the contacts that it becomes relevant or even overshadows the effect of de-trapping. It is believed to be the latter, because these edge effects are present regardless of the type of network in question. In close proximity to the edges, the position of the block (i.e. global aspect) has a greater effect on the current than the change applied to the block itself (i.e local aspect).

Focusing on the central region of the channel, all blocks positioned approximately 3 μm to 5 μm away from either contact edges are considered. This allows the exclusion of the the non-linear

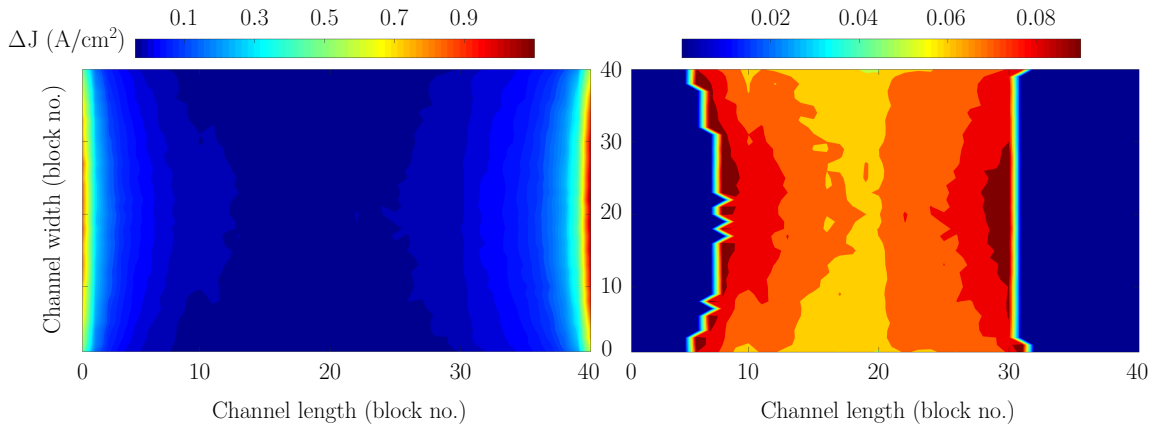

(a) Inhomogeneous network **(b) Central region**

Fig. 5.7: (a) Color map of the entire network after the manipulation process. High current density difference between pre- and post- manipulation observed near the contacts relating to the position of the block rather than local effects. **(b)** A detailed view of the central region of the network where a more local effect due to de-trapping is observed.

behavior previously mentioned (see Fig. 5.5(a)). Furthermore, this non-linearity is present at high drain voltages (i.e 35 V), on the other hand the network is operating at a lower drain voltage of 10 V. A varying intensity of the color map can be seen in Fig. 5.7(b), and the corresponding range of ΔJ lies between 0.01 A/cm^2 - 0.08 A/cm^2. This range is similar to what has been measured experimentally in [203]. In order to achieve this agreement the charge density for the manipulation process was raised to 2×10^{17} cm^{-3}. To calculate the density of traps in the central region, information from the two blocks resulting in both the highest and lowest ΔJ is extracted and used. Combining Eqs. (5.5a)-(5.5b), the resistances r can be rewritten as

$$r_{dark} = \frac{l}{eq\mu_p A} \tag{5.6}$$

and

$$r_{illum} = \frac{l}{e(q + \Delta q)\mu_p A} \quad , \tag{5.7}$$

where r_{dark} and r_{illum} are the resistances before and after the manipulation process, A and Δp are the area and trap density respectively. Finally, the trap density is expressed as

$$\Delta q_{avg} = \frac{l}{(r_{dark} - r_{illum})_{avg} e\mu_p A} \tag{5.8}$$

Both the trap density and the block resistances have a subscript "average" because there are four resistors per block and hence why the average value is calculated. Using Eq. (5.8) the average trap density was evaluated to be between 7.6×10^{16} cm^{-3} - 8×10^{16} cm^{-3}. This corresponds to approximately 40% of the trapped charges being promoted for transport. Given that only 40% of charges were de-trapped, increasing the density of the manipulation process would further promote more charges. Naturally the ΔJ will continue to increase but only up to a certain point,

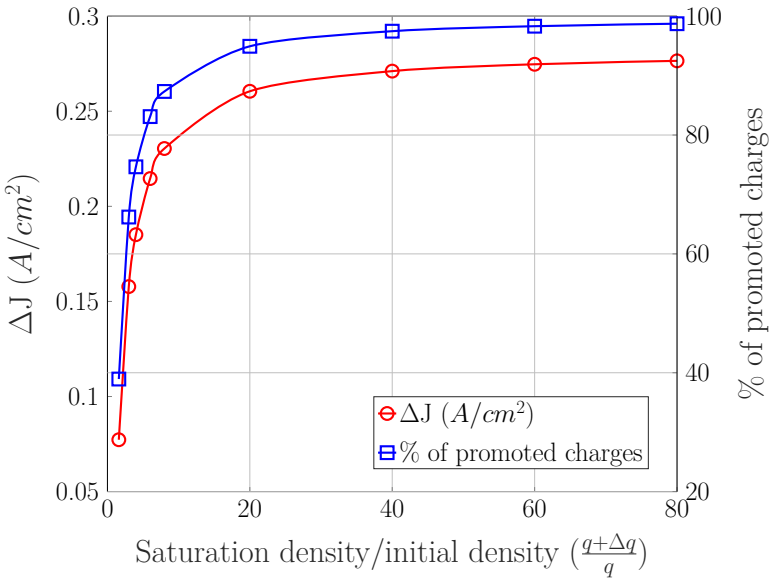

Fig. 5.8: Effect on both the promoted charges (blue) and ΔJ (red) with respect to the ratio between saturation and initial charge densities.

	Experimental	**Simulation**
Dark Current Density	350 A/cm^2	355 A/cm^2
ΔJ	0.01 A/cm^2 - 0.07 A/cm^2	0.01 A/cm^2 - 0.08 A/cm^2
Trap Density	4.4×10^{18} cm^{-3} (From Table I in [212])	4.85×10^{18} cm^{-3}

Table 5.2: Comparison between experimental measurements and simulation results.

at which it saturates irrespective of any further manipulation (i.e. all charges are de-trapped). To find out this onset of saturation, Fig. 5.8 shows the effect on both the promoted charges and the ΔJ for different densities of the manipulation process. From Fig. 5.8, almost all charges are de-trapped (i.e. 97%) when the strength of the manipulation is 40 times higher than the initial state of a chosen block. This corresponds to a total local charge density of 5×10^{18} cm^{-3} and hence a trap density of 4.85×10^{18} cm^{-3}.

The charge mobility given in Table 1 was chosen to obtain the aforementioned trap densities. The mobility itself was extracted from a DD simulation (see Fig. 5.5(b) - profile along the channel region of a pentacene transistor). At the desired operating point of the network, the mobility is almost constant and is estimated to be 6.5×10^{-3} cm^2/Vs. Using this mobility, a very good agreement was achieved between simulated and experimentally evaluated trap densities, as given in Table 5.2.

Finally, given that the above analysis was based on certain approximations such as how the gate and drain-source effects are included or even how the illumination process is interpreted and implemented, this same investigation can be done on the DD level. Using DD all aspects of a transistor operation are explicitly considered through solving both the Poisson and current equations. Moreover, the channel can be divided up into smaller segments where trap states at

a specific energy can be defined for each and every segment. Then, a similar analysis as done previously (i.e. on the resistor network) can be carried out using DD. But given that organic transistors usually have channel lengths in the range of tens of microns, then dividing up such long channels into sub-micron segments and monitoring the effect on the output current due to a change in a specific segment, it becomes increasingly complicated and time consuming. Furthermore, if the channel width is taken into consideration (i.e. going from 2- to 3- dimensions) it would then be nearly impossible to carry out an investigation similar to the SPCM procedure. Thus if an "on the fly" investigation of the effect of traps in organic transistors is required, the proposed resistor network model can act as an appropriate tool for that purpose given that it relies on certain approximations. Nevertheless, the analysis is done considering all important aspects of a transistor operation and on an adequate time-scale. More importantly, it has been shown that the model can be used to quantify low conductive regions in terms of trap densities and their effect on the output current. Hence, the local effect is more pronounced than the global state of the entire network (i.e. which defines the resistance pathway the current will undertake). This is critical as the aim is to trace the effect of traps back to a specific location in the organic film, as done by the SPCM procedure.

5.5 Conclusions

In this study, a simulation model based on a network of resistors to investigate traps states in organic thin films was presented. The model is used to interpret the results provided by scanning photo-current microscopy. Blocks of resistors are chosen and manipulated accordingly to mimic charge carrier de-trapping through an illumination process. Initially, the model has been successfully validated. This is followed by appropriately extending it for a more realistic approach, to identify defective regions in organic thin films. Quantifying these defective regions in term of trap densities, analyses showed that the difference in current observed as a result of spot illumination, can be related to charges being de-trapped at that same spot. This is true assuming respective local spots are not too close to the edges (approximately 3 µm to 5 µm away from the edges), where the effect of the contacts becomes predominant and the local property due to charge de-trapping is greatly overshadowed. Furthermore, to record a ΔJ similar to that of SPCM measurements, it was concluded that only 40% of charges were promoted. Yet a higher manipulation process (i.e. 40 times higher) was required to promote almost all trapped charges. This corresponds to a trap density of $4.85 \times 10^{18}\,\mathrm{cm}^{-3}$ which is also in agreement with experimentally measured trap densities in pentacene transistors.

Chapter 6

Summary and outlook

A theoretical investigation on the nature of charge transport in organic molecules, as well as device characterization in OFETs, on the entire dimension scale has been presented. On the atomistic scale, ab initio methods of DFT and NEGF were used to study the electronic structure and charge transport through SAM-forming molecules for the active region of a FET (i.e. SAMFET). The molecules of interest, were three different types of organo-phosphonates. The difference arising from the addition and size of the side chain substituted aromatic groups. A total of five molecular configurations were considered, with the latter two involving an overlap between the side chains. This was done with the aim to represent a thin monolayer of SAM-molecules given specific boundary conditions. Analyses in gas phase produced a trend of decreasing band gaps. Presence of the aromatic groups, their size, and overlap were concluded to be the main factors towards the observed trend. Furthermore, with increasing number of adjacent overlapping molecules, this eventually led to the stabilization of the HOMO and LUMO band edges. Molecules were then attached to Si/Al_2O_3 substrates, and capped by gold contacts to construct the desired device configurations. Charge transport simulations were carried out and transmission probabilities extracted. From these probabilities, conductive band gaps were identified observing a similar trend of molecular band gap reduction, to that in gas phase. Molecules with side chain aromatic groups exhibited higher evaluated currents. Furthermore, molecular orbital projections corresponding to high transmission probabilities indicated that both inter- and intra-chain flow of charges can occur in these molecules, allowing them to be suitable candidates for active regions in FETs.

Macro-scale investigations involved using the DD model for the characterization of OFETs. Important sub-models responsible for accurate description of events taking place within organic semiconductors were highlighted and considered in the simulation procedure. The effect of fixed charges, interface and bulk traps were investigated. Based on these investigations several scenarios were outlined for the fitting process of experimental transfer and output OFET characteristics. It was concluded that one scenario was insufficient to describe the transistor characteristics over the entire voltage range within device operation. This range was divided into two separate regimes, were each regime was described by a different set of parameterizations. An argument for this regime separation was discussed. Once fitting was achieved, this allowed for the extraction of important deivce performance measures including the threshold voltages and charge mobilities. Extracted values were found to be close to, if not similar, to what have been reported from experimental studies.

At the top of the dimension scale, circuit level modeling was used to identify low conductance regions in organic thin films. The equivalent experimental procedure is SPCM. This involved shining a laser light onto a specific spot along the thin film. Difference between measured photo-currents (post illumination), dark currents (pre- illumination), and hence local spot properties were depicted in the form of colormaps highlighting the strength of that difference. To investigate this process from a theoretical perspective, a theory of network resistors was applied. Manipulation

of block resistances provided the necessary effect of light illumination, and in a similar fashion colormaps were drawn out. The model was initially validated and then used as a comparison with experimental findings. Results were successfully reproduced. Trap densities corresponding to the identified low conductance regions (i.e. defective) were also evaluated. Something that SPCM cannot provide.

Looking forward, improvements could certainly be done on the existing work. Some of these are listed below for the separate investigations:

1. **Atomistic scale:** Improvements on device representations.
   - A full representation of the gold contact rather than a simple boundary for charge collection/injection.
   - Different instances of overlap between adjacent molecules within the packed variants. Only one orientation of overlap was considered, yet other orientations might be present.
2. **Macro-scale:** Inclusion of recombination effects.
   - Eventhough recombination is usually associated with organic solar cells, there is a possibility of it occurring in OFETs as well (i.e. ambipolar OFETs). Hence, affecting the overall transistor characteristics.
3. **Device scale:** Including other electrical components for a more detailed investigation of defective regions in organic thin films.
   - Without increasing the complexity of the model and maintaining the validity of the applied assumptions, other electrical components could be added for a more detailed approach. With the inclusion of capacitive elements, lifetimes of trapped charges could be evaluated. Hence, being able to identify if a defective region is either a shallow or deep trap.

As it was stated previously in the introduction, the presented work acts as a basis towards a multiscale approach. This was implemented to an extend between the DD and circuit based models. Nevertheless, it could applied across the entire dimension scale. Taking blend based OFETs as an example, it was proposed that the morphology of the active region upon material deposition is defined as a phase separation between small molecule and polymer, with the former located in the channel region at the oxide interface exhibiting high degree of structural order. First off all, atomistic simulations could be used to compute transfer integrals between individual molecules. These transfer integrals are taken as input parameters to the Marcus theory of hopping rates of charges within the framework of kinetic Monte Carlo (kMC) simulations. kMC , which is a stochastic based method can in turn compute charge mobilities considering these hopping rates (among other factors and possible occurring events), inside a simplified structure (i.e. a $50\,\text{nm} \times 50\,\text{nm} \times 50\,\text{nm}$ box sandwiched between two contacts). The resulting mobility could then be used as an input to the mobility model of choice inside the DD to characterize a blend based OFET. This allows the evaluation of final device performance parameters such as effective mobility, threshold voltages, and on/off ratios.

List of Figures

List of Tables

Bibliography

[1] L. Lu, T. Zheng, Q. Wu, A. M. Schneider, D. Zhao, and L. Yu. "Recent advances in bulk heterojunction polymer solar cells". In: *Chem. Rev.* 115.23 (2015), pp. 12666–12731. DOI: 10.1021/acs.chemrev.5b00098.

[2] J. Yuan, J. Gu, G. Shi, J. Sun, H. Q. Wang, and W. Ma. "High efficiency all-polymer tandem solar cells". In: *Sci. Rep.* 6.1 (2016), p. 26459. DOI: 10.1038/srep26459.

[3] J. Lui et al. "Fast charge separation in a non-fullerene organic solar cell with a small driving force". In: *Nat. Energy* 1.7 (2016), p. 16089. DOI: 10.1038/nenergy.2016.89.

[4] J. Nishide, H. Nakanotani, Y. Hiraga, and C. Adachi. "High-efficiency white organic light-emitting diodes using thermally activated delayed fluorescence". In: *Appl. Phys. Lett.* 104.23 (2014), p. 233304. DOI: 10.1063/1.4882456.

[5] H. Nakanotani et al. "High-efficiency organic light-emitting diodes with fluorescent emitters". In: *Nat. Commun.* 5.1 (2014), p. 4016. DOI: 10.1038/ncomms5016.

[6] J. H. Jou, S. Kumar, A. Agrawal, T. H. Li, and S. Sahoo. "Approaches for fabricating high efficiency organic light emitting diodes". In: *J. Mater. Chem. C* 3.13 (2015), pp. 2974–3002. DOI: 10.1039/C4TC02495H.

[7] T. Miwa, S. Kubo, K. Shizu, T. Komino, C. Adachi, and H. Kaji. "Blue organic light-emitting diodes realizing external quantum efficiency over 25% using thermally activated delayed fluorescence emitters". In: *Sci. Rep.* 7.1 (2017), p. 284. DOI: 10.1038/s41598-017-00368-5.

[8] K. Myny, S. Steudel, S. Smout, P. Vicca, F. Furthner, B. van der Putten, A. K. Tripathi, G. H. Gelinck, J. Genoe, W. Dehaene, and P. Heremans. "Organic RFID transponder chip with data rate compatible with electronic product coding". In: *Organic Electronics* 11.7 (2010), pp. 1176–1179. DOI: 10.1016/j.orgel.2010.04.013.

[9] B. K. Charlotte Kjellander, W. Smaal, K. Myny, J. Genoe, W. Dehaene, P. Heremans, and G. H. Gelinck. "Optimized circuit design for flexible 8-bit RFID transponders with active layer of ink-jet printed small molecule semiconductors". In: *Organic Electronics* 14.3 (2013), pp. 768–774. DOI: 10.1016/j.orgel.2012.12.027.

[10] T. Someya, A. Dodabalapur, J. Huang, K. C. See, and H. E. Katz. "Chemical and physical sensing by organic field-effect transistors and related devices". In: *Adv. Mater.* 22.34 (2010), pp. 3799–3811. DOI: /10.1002/adma.200902760.

[11] S. Han, X. Zhuang, W. Shi, X. Yang, L. Li, and J. Yu. "Poly(3-hexylthiophene)/polystyrene (P3HT/PS) blends based organic field-effect transistor ammonia gas sensor". In: *Sensors and Actuators B: Chemical* 225.31 (2016), pp. 10–15. DOI: 10.1016/j.snb.2015.11.005.

[12] M. Yun, A. Sharma, C. Fuentes-Hernandez, D. K. Hwang, A. Dindar, S. Singh, S. Choi, and B. Kippelen. "Stable organic field-effect transistors for continuous and nondestructive sensing of chemical and biologically relevant molecules in aqueous environment". In: *ACS Appl. Mater. Interfaces* 6.3 (2014), pp. 1616–1622. DOI: 10.1021/am404460j.

[13] G. Gelinck, P. Heremans, K. Nomoto, and T. D. Anthopoulos. "Organic transistors in optical displays and microelectronic applications". In: *Adv. Mater.* 22.34 (2010), pp. 3778–3798. DOI: 10.1002/adma.200903559.

[14] W. Shockley. "A unipolar field-effect transistor". In: *Proc. IRE* 40.11 (1952), pp. 1365–1376. DOI: 10.1109/JRPROC.1952.273964.

[15] C. Reese and Z. Bao. "Overestimation of the field-effect mobility via transconductance measurements and the origin of the output/transfer characteristics discrepancy in organic field-effect transistors". In: *J. Appl. Phys.* 105.2 (2009), pp. 1365–1376. DOI: 10.1063/1.3029587.

[16] H. Li, Y. Li, H. Li, and J-L. Bredas. "Organic field-effect transistors: a 3d kinetic monte carlo simulation of the current characteristics in micrometer-sized devices". In: *Adv. Func. Mater.* 27.9 (2017), p. 1605715. DOI: 10.1002/adfm.201605715.

[17] T. Okachi. "Mobility overestimation due to minority carrier injection and trapping in organic field-effect transistors". In: *Organic Electronics* 57 (2018), pp. 34–44. DOI: 10.1016/j.orgel.2018.02.034.

[18] A. F. Paterson et al. "Recent progress in high-mobility organic transistors: a reality check". In: *Adv. Mater.* 30.36 (2018), p. 1801079. DOI: 10.1002/adma.201801079.

[19] T. Uemura et al. "On the extraction of charge carrier mobility in high-mobility organic transistors". In: *Adv. Mater.* 28.1 (2015), pp. 151–155. DOI: 10.1002/adma.201503133.

[20] I. McCulloch, A. Salleo, and M. Chabinyc. "Avoid the kinks when measuring mobility". In: *Science* 352.6293 (2016), pp. 1521–1522. DOI: 10.1126/science.aaf9062.

[21] E. G. Bittle, J. I. Basham, T. N. Jackson, O. D. Jurchescu, and D. J. Gundlach. "Mobility overestimation due to gated contacts in organic field-effect transistors". In: *Nat. Commun.* 7.1 (2016), p. 10908. DOI: 10.1038/ncomms10908.

[22] H. H. Choi, K. Cho, C. D. Frisbie, H. Sirringhaus, and V. Podzorov. "Critical assessment of charge mobility extraction in FETs". In: *Nat. Mater.* 17 (2018), pp. 2–7. DOI: 10.1038/nmat5035.

[23] C. Liu et al. "Device physics of contact issues for the overestimation and underestimation of carrier mobility in field-effect transistors". In: *Phys. Rev. Appl.* 8.3 (2017), p. 034020. DOI: 10.1103/PhysRevApplied.8.034020.

[24] A. B. Mallik et al. "Design, Synthesis and Transistor Performance of Organic Semiconductors". In: *Organic Field-Effect Transistors*. Ed. by Zhenan Bao and Jason Locklin. Taylor & Francis, 2007. Chap. 3.1, pp. 161–228.

[25] H. Sirringhaus et al. "Two-dimensional charge transport in self-organized, high-mobility conjugated polymers". In: *Nature* 401.6754 (1999), pp. 685–688. DOI: 10.1038/44359.

[26] Z. Fei et al. "Influence of side-chain regiochemistry on the transistor performance of high-mobility, all-donor polymers". In: *J. Am. Chem. Soc.* 136.43 (2014), pp. 15154–15157. DOI: 10.1021/ja508798s.

[27] D. M. Leeuw, M. M. J. Simenon, A. R. Brown, and R. E. F. Einerhand. "Stability of n-type doped conducting polymers and consequences for polymeric microelectronic devices". In: *Synth. Met.* 87.1 (1997), pp. 53–59. DOI: 10.1016/S0379-6779(97)80097-5.

[28] H. Yan et al. "A high-mobility electron-transporting polymer for printed transistors". In: *Nature* 457.7230 (2009), pp. 679–686. DOI: 10.1038/nature07727.

[29] R. Kim et al. "High-mobility air-stable naphthalene diimide-based copolymer containing extended π-conjugation for n-channel organic field effect transistors". In: *Adv. Func. Mater.* 23.46 (2013), pp. 5719–5727. DOI: 10.1002/adfm.201301197.

[30] M. Kitamura and Y. Arakawa. "Pentacene-based organic field-effect transistors". In: *J. Phys.: Condens. Matter* 20.18 (2008), p. 184011. DOI: 10.1088/0953-8984/20/18/184011.

[31] Y. Xiong et al. "A furan-thiophene-based quinoidal compound: a new class of solution-processable high-performance n-type organic semiconductor". In: *J. Phys.: Condens. Matter* 28.28 (2016), pp. 5949–5953. DOI: 10.1002/adma.201600120.

[32] B. Lüssem, M. Riede, and K. Leo. "Doping of organic semiconductors". In: *Phys. Stat. Sol. (a)* 210.1 (2013), pp. 9–43. DOI: 10.1002/pssa.201228310.

[33] B. H. lee, G. C. Bazan, and A. J. Heeger. "Doping-induced carrier density modulation in polymer field-effect transistors". In: *Adv. Mater.* 28.1 (2016), pp. 57–62. DOI: 10.1002/adma.201504307.

[34] C. Luo et al. "General strategy for self-assembly of high oriented nanocrystalline semiconducting polymers with high mobility". In: *Nano Lett.* 14.5 (2014), pp. 2764–2771. DOI: 10.1021/nl500758w.

[35] A. Perez-Rodriguez, I. Temino, C. Ocal, M. Mas-Torrent, and E. Barrena. "Decoding the vertical phase separation and it's impact on C_8-BTBT/PS transistor properties". In: *Appl. Mater. Interfaces* 10.8 (2018), pp. 7296–7303. DOI: 10.1021/acsami.7b19279.

[36] Z. He, D. Li, D. K. Hensley, A. J. Rondinone, and J. Chen. "Switching phase separation mode by varying the hydrophobicity of polymer additives in solution-processed semiconducting small-molecule/polymer blends". In: *Appl. Phys. Lett.* 103.11 (2013), p. 113301. DOI: 10.1063/1.4820588.

[37] K. Zhao et al. "Vertical phase separation in small molecule:polymer blend organic thin film transistors can be dynamically controlled". In: *Adv. Func. Mater.* 26.11 (2016), pp. 1737–1746. DOI: 10.1002/adfm.201503943.

[38] A. F. Paterson et al. "The impact of molecular p-doping on charge transport in high-mobility small-molecule/polymer blend organic transistors". In: *Adv. Electron. Mater.* 4.10 (2018), p. 1700464. DOI: 10.1002/aelm.201700464.

[39] M. Niazi et al. "Contact-induced nucleation in high-performance bottom-contact organic thin film transistors manufactured by large-area compatible solution processing". In: *Adv. Func. Mater.* 26.14 (2015), pp. 2371–2378. DOI: 10.1002/adfm.201502428.

[40] A. Hamaguchi et al. "Single-crystal-like organic thin-film transistors fabricated from dinaphtho[2,3-b:2′,3′-f]thieno[3,2-b]thiophene (DNTT) precursor–polystyrene blends". In: *Adv. Mater.* 27.42 (2015), pp. 6606–6611. DOI: 10.1002/adma.201502413.

[41] S. Kwon et al. "Organic single-crystal semiconductor films on a millimeter domain scale". In: *Adv. Mater.* 27.43 (2015), pp. 6870–6877. DOI: 10.1002/adma.201502980.

[42] J. Smith et al. "Solution-processed small molecule/polymer blend organic thin-film transistors with hole mobility greater than 5 cm^2/Vs". In: *Adv. Mater.* 24.18 (2012), pp. 2441–2446. DOI: 10.1002/adma.201200088.

[43] J. Soeda, T. Okamoto, C. Mitsui, and Jun. Takeya. "Stable growth of large-area single crystalline thin films from organic semiconductor/polymer blend solution for high-mobility organic field-effect transistors". In: *Organic Electronics* 39 (2016), pp. 127–132. DOI: 10.1016/j.orgel.2016.09.006.

[44] J. Panidi et al. "Remarkable enhancement of the hole mobility in several organic small-molecule, polymers and small-molecule:polymer blend transistors by simple admixing of the lewis acid p-dopant $B(C_6F_5)_3$". In: *Adv. Sci.* 5.1 (2018), p. 1700290. DOI: 10.1002/advs.201700290.

[45] M. Born and R. Oppenheimer. "Zur Quantentheorie der Molekeln". In: *Annalen der Physik* 389.20 (1927), pp. 457–484. DOI: 10.1002/andp.19273892002.

[46] J. Behler, B. Delley, S. Lorenz, K. Reuter, and M. Scheffer. "Dissociation of O_2 at Al(111): the role of spin selection rules". In: *Phys. Rev. Lett.* 94.3 (2005), p. 036104. DOI: 10.1103/PhysRevLett.94.036104.

[47] J. Behler, K. Reuter, and M. Scheffer. "Nonadiabatic effects in the dissociation of oxygen molecules at the Al(111) surface". In: *Phys. Rev. B* 77.11 (2008), p. 115421. DOI: 10.1103/PhysRevB.77.115421.

[48] A. M. Wodtke, J. C. Tully, and D. J. Auerbach. "Electronically non-adiabatic interactions of molecules at metal surfaces: can we trust the born-oppenheimer approximation for surface chemistry?" In: *Int. Rev. Phys. Chem.* 23.4 (2007), pp. 513–539. DOI: 10.1080/01442350500037521.

[49] A. C. Luntz, M. Persson, and G. O. Sitz. "Theoretical evidence for nonadiabatic vibrational de-excitation in $H_2(D_2)$ state-to-sate scattering from Cu(100)". In: *J. Chem. Phys.* 124.9 (2006), p. 091101. DOI: 10.1063/1.2177664.

[50] V. Fock. "Näherungsmethod zur lösung des quantenmechanischen mehrkörperproblems". In: *Z. Physik* 61.1-2 (1930), pp. 126–148. DOI: 10.1007/BF01340294.

[51] D. R. Hartree. "Self-consistent field, with exchange, for beryllium". In: *Proc. R. Soc. Lond. A.* 150.869 (1935). DOI: 10.1098/rspa.1935.0085.

[52] R. Ditchfield, W. J. Hehre, and J. A. Pople. "Self-consistent molecular-orbital methods. IX. An extended gaussian-type basis for molecular-orbital studies of organic molecules". In: *J. Chem. Phys.* 54.2 (1971), p. 724. DOI: 10.1063/1.1674902.

[53] J. E. Bene, R. Ditchfield, and J. A. Pople. "Self-consistent molecular-orbital methods. X. Molecular orbital studies of excited states with minimal and extended basis sets". In: *J. Chem. Phys.* 55.5 (1971), p. 2236. DOI: 10.1063/1.1676398.

[54] D. E. Woon and T. H. Dunning Jr. "Benchmark calculations with correlated molecular wave functions. I. Multireference configuration interaction calculations for the second row diatomic hydrides". In: *J. Chem. Phys.* 99.3 (1993), p. 1914. DOI: 10.1063/1.465306.

[55] D. E. Woon and T. H. Dunning Jr. "Gaussian basis sets for use in correlated molecular calculations. V. Core-valence basis sets for boron through neon". In: *J. Chem. Phys.* 103.11 (1995), p. 4572. DOI: 10.1063/1.470645.

[56] T. H. Dunning Jr. "A road map for the calculation of molecular binding energies". In: *J. Phys. Chem. A* 104.40 (2000), pp. 9062–9080. DOI: 10.1021/jp001507z.

[57] L. H. Thomas. "The calculation of atomic fields". In: *Proc. Camb. Phil. Soc.* 23.5 (1927), pp. 542–548. DOI: 10.1017/S0305004100011683.

[58] E. Fermi. "Un metodo statistico per la determinazione di alcune proprieta dell'atomo". In: *Rend. Accad. Naz. Lincei* 6 (1927), pp. 602–607.

[59] P. Hohenberg and W. Kohn. "Inhomogeneous electron gas". In: *Phys. Rev.* 136.3B (1964), p. 864. DOI: 10.1103/PhysRev.136.B864.

[60] W. Kohn and L. J. Sham. "Self-consistent equations including exchange and correlation effects". In: *Phys. Rev.* 140.4A (1965), p. 1133. DOI: 10.1103/PhysRev.140.A1133.

[61] J. P. Perdew and K. Schmidt. "Jacob's ladder of density functional approximations for the exchange-correlation energy". In: *AIP Conf. Proc.* 577.1 (2001), pp. 1–20. DOI: 10.1063/1.1390175.

[62] M. Gell-Mann and K. A. Brueckner. "Correlation energy of an electron gas at high density". In: *Phys. Rev.* 106.2 (1957), p. 364. DOI: 10.1103/PhysRev.106.364.

[63] D. M. Ceperley and B. J. Adler. "Ground state of the electron gas by a stochastic method". In: *Phys. Rev. Lett.* 45.7 (1980), p. 566. DOI: 10.1103/PhysRevLett.45.566.

[64] J. P. Perdew and A. Zunger. "Self-interaction correction to density-functional approximations for many-electron systems". In: *Phys. Rev. B* 23.10 (1981), p. 5048. DOI: 10.1103/PhysRevB.23.5048.

[65] J. P. Perdew and Y. Wang. "Accurate and simple analytic representation of the electron-gas correlation energy". In: *Phys. Rev. B* 45.23 (1992), p. 13244. DOI: 10.1103/PhysRevB.45.13244.

[66] S. Vosko, L. Wilk, and M. Nusair. "Accurate spin-dependent electron liquid correlation energies for local spin density calculations: a critical analysis". In: *Can. J. Phys.* 58.8 (1980), pp. 1200–1211. DOI: 10.1139/p80-159.

[67] V. N. Staroverov, G. E. Scuseria, J. Tao, and J. P. Perdew. "Tests of a ladder of density functionals for bulk solids and surfaces". In: *Phys. Rev. B* 69.7 (2008), p. 075102. DOI: 10.1103/PhysRevB.69.075102.

[68] G. I. Csonka et al. "Assessing the performance of recent density functionals for bulk solids". In: *Phys. Rev. B* 79.15 (2009), p. 155107. DOI: 10.1103/PhysRevB.79.155107.

[69] J. harl and G. Kresse L. Schimka. "Assessing the quality of the random phase approximation for lattice constants and atomization energies of solids". In: *Phys. Rev. B* 81.11 (2010), p. 115126. DOI: 10.1103/PhysRevB.81.115126.

[70] A. D. Becke. "Density-functional exchange-energy approximation with correct asymptotic behavior". In: *Phys. Rev. A* 38.6 (1988), p. 3098. DOI: 10.1103/PhysRevA.38.3098.

[71] J. P. Perdew, K. Burke, and M. Ernzerhof. "Generalized gradient approximation made simple". In: *Phys. Rev. Lett.* 78.7 (1997), p. 1396. DOI: 10.1103/PhysRevLett.78.1396.

[72] J. P. Perdew and Y. Wang. "Accurate and simple density functional for the electronic exchange energy: Generalized gradient approximation". In: *Phys. Rev. B* 33.12 (1986), p. 8800. DOI: 10.1103/PhysRevB.33.8800.

[73] Y. Wang and J. P. Perdew. "Spin scaling of the electron-gas correlation energy in the high-density limit". In: *Phys. Rev. B* 43.11 (1991), p. 8911. DOI: 10.1103/PhysRevB.43.8911.

[74] C. Lee, W. Yang, and R. G. Parr. "Development of the Colle-Salvetti correlation-energy formula into a functional of the electron density". In: *Phys. Rev. B* 37.2 (1988), p. 785. DOI: 10.1103/PhysRevB.37.785.

[75] S. Datta. *Electronic transport in mesoscopic systems*. Cambridge University Press, 1995.

[76] S. Datta. *Quantum transport: atom to transistor*. Cambridge University Press, 2005.

[77] R. Landauer. "Spatial variation of currents and fields due to localized scatterers in metallic conduction". In: *IBM J. Res. Dev.* 1.3 (1957), pp. 223–231. DOI: 10.1147/rd.13.0223.

[78] R. Landauer. "Electrical resistance of disordered one-dimensional lattices". In: *Phil. Mag.* 21.172 (1970), pp. 863–867. DOI: 10.1080/14786437008238472.

[79] A. Jüngel. *Transport equations for semiconductors*. Springer, 2010.

[80] Karl Hess. *Advanced theory of semiconductor devices*. Wiley-IEEE Press, 1999.

[81] A. Aviram and M. A. Ratner. "Molecular rectifiers". In: *Chem. Phys. Lett.* 29.2 (1974), pp. 277–283. DOI: 10.1016/0009-2614(74)85031-1.

[82] G. Whitesides and B. Grzybowski. "Self-assembly at all scales". In: *Science* 295.5564 (2002), pp. 2418–2421. DOI: 10.1126/science.1070821.

[83] S. Casalini, C. A. Bortolotti, F. Leonardi, and F. Biscarini. "Self-assembled monolayers in organic electronics". In: *Chem. Soc. Rev.* 46.1 (2017), pp. 40–71. DOI: 10.1039/C6CS00509H.

[84] S. Ju et al. "High performance ZnO nanowire field effect transistors with organic gate nanodielectrics: effects of metal contacts and ozone treatment". In: *Nanotechnology* 18.15 (2007), p. 155201. DOI: 10.1088/0957-4484/18/15/155201.

[85] S. DiBenedetto, D. Frattarelli, M. A. Ratner, A. Facchetti, and T. J. Marks. "Vapor phase self-assembly of molecular gate dielectrics for thin film transistors". In: *J. Am. Chem. Soc.* 130.24 (2008), pp. 7528–7529. DOI: 10.1021/ja801309g.

[86] E. C. P. Smits et al. "Bottom-up organic integrated circuits". In: *Nature* 455.7215 (2008), pp. 956–959. DOI: 10.1038/nature07320.

[87] D. J. Gundlach et al. "Contact-induced crystallinity for high-performance soluble acene-based transistors and circuits". In: *Nat. Mater.* 7.3 (2008), pp. 216–221. DOI: 10.1038/nmat2122.

[88] A. L. Briseno et al. "Patterning organic single-crystal transistor arrays". In: *Nature* 444.7121 (2006), pp. 913–917. DOI: 10.1038/nature05427.

[89] H. Ma, H-L. Yip, F. Huang, and A. K-Y. Jen. "Interface engineering for organic electronics". In: *Adv. Func. Mater.* 20.9 (2010), pp. 1371–1388. DOI: 10.1002/adfm.200902236.

[90] M. Halik and A. Hirsch. "The potential of molecular self-assembled monolayers in organic electronic devices". In: *Adv. Mater.* 23.22-23 (2011), pp. 2689–2695. DOI: 10.1002/adma.201100337.

[91] H. Klauk, U. Zschieschang, and M. Halik J. Pflaum. "Ultralow-power organic complementary circuits". In: *Nature* 445 (2007), pp. 745–748. DOI: 10.1002/adma.201100337.

[92] M-H. Yoon, A. Facchetti, and T. J. Marks. "σ-π molecular dielectric multilayers for low-voltage organic thin-film transistors". In: *Proc. Natl. Acad. Sci. USA* 102.13 (2005), pp. 4678–4682. DOI: 10.1073/pnas.0501027102.

[93] U. Zschieschang et al. "Mixed self-assembled monolayer gate dielectrics for continuous threshold voltage control in organic transistors and circuits". In: *Adv. Mater.* 22.40 (2010), pp. 4489–4493. DOI: 10.1002/adma.201001502.

[94] T. Schmaltz, G. Sforazzini, T. Reichert, and H. Frauenrath. "Self-assembled monolayers as patterning tool for organic electronic devices". In: *Adv. Mater.* 29.18 (2017), p. 1605286. DOI: 10.1002/adma.201605286.

[95] A. Ulman. "Formation and structure of self-assembled monolayers". In: *Chem. Rev.* 96.4 (1996), pp. 1533–1554. DOI: 10.1021/cr9502357.

[96] A. Perl, D. N. Reinhoudt, and J. Huskens. "Microcontact printing: limitations and achievements". In: *Adv. Mater.* 21.22 (2009), pp. 2257–2268. DOI: 10.1002/adma.200801864.

[97] G-Y. Liu, S. Xu, and Y. Qian. "Nanofabrication of self-assembled monolayers using scanning probe lithography". In: *Acc. Chem. Res.* 33.7 (2000), pp. 457–466. DOI: 10.1021/ar980081s.

[98] S.Xu and G-Y. Liu. "Nanometer-scale fabrication by simultaneous nanoshaving and molecular self-assembly". In: *Langmuir* 13.2 (1997), pp. 127–129. DOI: 10.1021/la962029f.

[99] S. Hong, J. Zhu, and C. A. Mirkin. "Multiple ink nanolithography: toward a multiple-pen nano-plotter". In: *Science* 286.5439 (1999), pp. 523–525. DOI: 10.1126/science.286.5439.523.

[100] D. S. Ginger, H. Zhang, and C. A. Mirkin. "The evolution of dip-pen nanolithography". In: *Angew. Chem. Intl. Ed.* 43.1 (2003), pp. 30–45. DOI: 10.1002/anie.200300608.

[101] K. Fu, A. M. Klibanov, and R. Langer. "Protein stability in controlled-release systems". In: *Nat. Biotechnol.* 18.1 (2000), pp. 24–25. DOI: 10.1038/71875.

[102] B. D. Ratner. "The engineering of biomaterials exhibiting recognition and specificity". In: *J. Mol. Recognit.* 9.5-6 (1996), pp. 617–625. DOI: 10.1002/(SICI)1099-1352(199634/12)9:5/6<617::AID-JMR310>3.0.CO;2-D.

[103] E. Ostuni, R. G. Chapman, r. E. Holmlin, S. Takayama, and G. M. Whitesides. "A survey of structure-property relationships of surfaces that resist the adsorption of protein". In: *Langmuir* 17.18 (2001), pp. 5605–5620. DOI: 10.1021/la010384m.

[104] L. E. Niklason et al. "Functional arteries grown in vitro". In: *Science* 284.5413 (1999), pp. 489–493. DOI: 10.1126/science.284.5413.489.

[105] D. G. Castner and B. D. Ratner. "Biomedical surface science: foundations to frontiers". In: *Surf. Sci.* 500.1 (2002), pp. 28–60. DOI: 10.1016/S0039-6028(01)01587-4.

[106] P. Harder, M. Grunze, R. Dahint, G. M. Whitesides, and P. E. Laibinis. "Molecular conformation in oligo(ethylene glycol)-terminated self-assembled monolayers on gold and silver surfaces determines their ability to resist protein adsorption". In: *J. Phys. Chem. B* 102.2 (1998), pp. 426–436. DOI: 10.1021/jp972635z.

[107] D. Bandyopadhyay, D. Prashar, and Y-Y. Luk. "Anti-fouling chemistry of chiral monolayers: enhancing biofilm resistance on racemic surface". In: *Langmuir* 27.10 (2011), pp. 6124–6131. DOI: 10.1021/la200230t.

[108] R. G. Chapman et al. "Surveying for surfaces that resist the adsorption of proteins". In: *J. Am. Chem. Soc.* 122.34 (2000), pp. 8303–8304. DOI: 10.1021/ja000774f.

[109] Y. Xia, X-M. Zhao, and G. M. Whitesides. "Pattern transfer: self-assembled monolayers as ultrathin resists". In: *Microelectron. Eng.* 32.1 (1996), pp. 255–268. DOI: 10.1016/0167-9317(95)00174-3.

[110] J. A. Rogers, Z. Bao, A. Makhija, and P. Braun. "Printing process suitable for reel-to-reel production of high-performance organic transistors and circuits". In: *Adv. Mater.* 11.9 (1999), pp. 741–745. DOI: 10.1002/(SICI)1521-4095(199906)11:9<741::AID-ADMA741>3.0.CO;2-L.

[111] S. Steudel, D. Janssen, S. Verlaak, J. Genoe, and P. Heremans. "Patterned growth of pentacene". In: *Appl. Phys. Lett.* 85.23 (2004), p. 5550. DOI: 10.1063/1.1832732.

[112] A. Salomon et al. "Comparison of electronic transport measurements on organic molecules". In: *Adv. Mater.* 15.22 (2003), pp. 1881–1890. DOI: 10.1002/adma.200306091.

[113] C. Vericat et al. "Self-assembled monolayers of thiolates on metals: a review article on sulfur-metal chemistry and surface structures". In: *RSC Adv.* 5.53 (2014), pp. 27730–27754. DOI: 10.1039/C4RA04659E.

[114] W. S. Hu, Y. T. Tao, Y. J. Hsu, D. H. Wei, and Y. S. Wu. "Molecular orientation of evaporated pentacene films on gold: alignment effect of self-assembled monolayer". In: *Langmuir* 21.6 (2005), pp. 2260–2266. DOI: 10.1021/la047634u.

[115] K. Asadi, Y. Wu, F. Gholamrezaie, P. Rudolf, and P. W. M. Blom. "Single-layer pentacene field-effect transistors using electrodes modified with self-assembled monolayers". In: *Adv. Mater.* 21.41 (2009), pp. 4109–4114. DOI: 10.1002/adma.200803455.

[116] F. Gholamrezaie et al. "Controlling charge injection by self-assembled monolayers in bottom-gate and top-gate organic field-effect transistors". In: *Synth. Met.* 161.21-22 (2011), pp. 2226–2229. DOI: 10.1016/j.synthmet.2011.08.020.

[117] T. Abu-Husein et al. "The effect of embedded dipoles in aromatic self-assembled monolayers". In: *Adv. Func. Mater.* 25.25 (2015), pp. 3943–3957. DOI: 10.1002/adfm.201500899.

[118] G. M. Lazzerini et al. "Increased efficiency of light-emitting diodes incorporating anodes functionalized with fluorinated azobenzene monolayers and a green-emitting polyfluorene derivative". In: *Appl. Phys. Lett.* 101.15 (2012), p. 153306. DOI: 10.1063/1.4758682.

[119] R. Ruiz, A. Papadimitratos, A. C. Mayer, and G. G. Malliaras. "Thickness Dependence of Mobility in Pentacene Thin-Film Transistors". In: *Adv. Mater.* 17.14 (2005), pp. 1795–1798. DOI: 10.1002/adma.200402077.

[120] A. Hoppe, T. Balster, T. Muck, and V. Wagner. "Scaling limits and MHz operation in thiophene-based field-effect transistors". In: *Physica Status Solidi (a)* 205.3 (2008), pp. 612–625. DOI: 10.1002/pssa.200723442.

[121] T. Cramer et al. "Water-induced polaron formation at the pentacene surface: quantum mechanical molecular mechanics simulations". In: *Phys. Rev. B* 79.15 (2009), p. 155316. DOI: 10.1103/PhysRevB.79.155316.

[122] S. G. J. Mathijssen et al. "Revealing buried interfaces to understand the origins of threshold voltage shifts in organic field-effect transistors". In: *Adv. Mater.* 22.45 (2010), pp. 5105–5109. DOI: 10.1002/adma.201001865.

[123] H. S. Lee et al. "Effect of the phase states of self-assembled monolayers on pentacene growth and thin-film transistor characteristics". In: *J. Am. Chem. Soc.* 130.32 (2008), pp. 10556–10564. DOI: 10.1021/ja800142t.

[124] S. Onclin, B. J. Ravoo, and D. N. Reinhoudt. "Engineering silicon oxide surfaces using self-assembled monolayers". In: *Angew. Chem.* 44.39 (2005), pp. 6282–6304. DOI: 10.1002/anie.200500633.

[125] R. Helmy and A. Y. Fadeev. "Self-assembled monolayers supported on TiO_2: comparison of $C_{18}H_{37}SiX_3$ (X=H,Cl,OCH_3), $C_{18}H_{37}Si(CH_3)_2Cl$, and $C_{18}H_{37}PO(OH)_2$". In: *Langmuir* 18.23 (2002), pp. 8924–8928. DOI: 10.1021/la0262506.

[126] M. Lessel et al. "Self-assembled silane monolayers: an efficient step-by-step recipe for high-quality, low energy surfaces". In: *Surf. Interface Anal.* 47.5 (2015), pp. 557–564. DOI: 10.1002/sia.5729.

[127] M. Shtein, J. Mapel, J. B. Benziger, and S. R. Forrest. "Effects of film morphology and gate dielectric surface preparation on the electrical characteristics of organic-vapor-phase-deposited pentacene thin-film transistors". In: *Appl. Phys. Lett.* 81.2 (2002), p. 268. DOI: 10.1063/1.1491009.

[128] B. M. Silverman, K. A. Wieghaus, and J. Schwartz. "Comparative properties of siloxane vs phosphonate monolayers on a key titanium alloy". In: *Langmuir* 21.1 (2005), pp. 225–228. DOI: 10.1021/la048227l.

[129] M. McDowell, I. G. Hill, J. E. McDermott, S. L. Bernasek, and J. Schwartz. "Improved organic thin-film transistor performance using novel self-assembled monolayers". In: *Appl. Phys. Lett.* 88.7 (2006), p. 073505. DOI: 10.1063/1.2173711.

[130] G. E. Moore. "Cramming more components onto integrated circuits". In: *Electronics* 38.8 (1965), pp. 114–117. DOI: 10.1109/N-SSC.2006.4785860.

[131] M. Halik et al. "Low-voltage organic transistors with an amorphous molecular gate dielectric". In: *Nature* 431.7011 (2004), pp. 963–966. DOI: 10.1038/nature02987.

[132] K. Sekine, Y. Saito, M. Hirayama, and T. Ohmi. "Highly reliable ultrathin silicon oxide film formation at low temperature by oxygen radical generated in high-density krypton plasma". In: *IEEE Tran. Elec. Dev.* 48.8 (2001), pp. 1550–1555. DOI: 10.1109/16.936559.

[133] T. Sekitani, U. Zschieschang, H. Klauk, and T. Someya. "Flexible organic transistors and circuits with extreme bending stability". In: *Nat. Mater.* 9.12 (2010), pp. 1015–1022. DOI: 10.1038/nmat2896.

[134] R. P. Ortiz, A. Facchetti, and T. J. Marks. "High-κ organic, inorganic and hybrid dielectrics for low-voltage organic field-effect transistors". In: *Chem. Rev.* 110.1 (2010), pp. 205–239. DOI: 10.1021/cr9001275.

[135] S. G. J. Mathijssen. "Monolayer coverage and channel length set the mobility in self-assembled monolayer field-effect transistors". In: *Nat. Nanotechnol.* 4.10 (2009), pp. 674–680. DOI: 10.1038/nnano.2009.201.

[136] M. Novak et al. "Low-voltage p- and n-type organic self-assembled monolayer field effect transistors". In: *Nano Lett.* 11.1 (2010), pp. 156–159. DOI: 10.1021/nl103200r.

[137] J. L. Bredas, J. P. Calbert, D. A. da Silva Filho, and J. Cornil. "Organic semiconductors: a theoretical characterization of the basic parameters governing charge transport". In: *Proc. Natl. Acad. Sci. USA* 99.9 (2002), pp. 5804–5809. DOI: 10.1073/pnas.092143399.

[138] J. L. Bredas, D. belijonne, V. Coropceanu, and J. Cornil. "Charge-transfer and energy-transfer processes in π-conjugated oligomers and polymers: a molecular picture". In: *Chem. Rev.* 104.11 (2004), pp. 4971–5004. DOI: 10.1021/cr040084k.

[139] T. P. Nguyen, J. H. Shim, and J. Y. Lee. "Density functional theory studies of hole mobility in picene and pentacene crystals". In: *J. Phys. Chem C* 119.21 (2015), pp. 11301–11310. DOI: 10.1021/jp511484d.

[140] H. Bässler. "Charge Transport in Disordered Organic Photoconductors: A Monte Carlo Simulation Study". In: *Phys. Stat. Sol. (b)* 175.1 (1993), pp. 15–56. DOI: 10.1002/pssb.2221750102.

[141] R. Noriega and A. Salleo. "Charge Transport Theories in Organic Semiconductors". In: *Organic Electronics II: More materials and Applications*. Ed. by Hagen Klauk. Wiley-VCH, 2012. Chap. 3, pp. 67–104.

[142] V. Podzorov, E. Menard, A. Borissov, V. Kiryukhin, J. A. Rogers, and M. E. Gershenson. "Intrinsic Charge Transport on the Surface of Organic Semiconductors". In: *Phys. Rev. Lett.* 93.8 (2004), p. 086602. DOI: 10.1103/PhysRevLett.93.086602.

[143] V. Podzorov, E. Menard, J. A. Rogers, and M. E. Gershenson. "Hall Effect in the Accumulation Layers on the Surface of Organic Semiconductors". In: *Phys. Rev. Lett.* 95.22 (2005), p. 226601. DOI: 10.1103/PhysRevLett.95.226601.

[144] T. Hasegawa and J. Takeya. "Organic field-effect transistors using single crystals". In: *Sci. Technol. Adv. Mater.* 10.2 (2009), p. 024314. DOI: 10.1088/1468-6996/10/2/024314.

[145] G. Horowitz. "Charge transport in oligomers". In: *Organic Field-Effect Transistors*. Ed. by Zhenan Bao and Jason Locklin. Taylor & Francis, 2007. Chap. 2.2, pp. 73–99.

[146] P. Stallinga. "Electronic Transport in Organic Materials: Comparison of Band Theory with Percolation/(Variable Range) Hopping Theory". In: *Adv. Mater.* 23.30 (2011), pp. 3356–3362. DOI: 10.1002/adma.201101129.

[147] A. Troisi. "Charge transport in high mobility molecular semiconductors: classical models and new theories". In: *Chem. Soc. Rev* 40.5 (2011), pp. 2347–2358. DOI: 10.1039/C0CS00198H.

[148] D. Venkateshvaran et al. "Approaching disorder-free transport in high-mobility conjugated polymers". In: *Nature* 515 (2014), pp. 384–388. DOI: 10.1038/nature13854.

[149] W. Kaiser, T. Albes, and A. Gagliardi. "Charge carrier mobility of disordered organic semiconductors with correlated energetic and spatial disorder". In: *Phys. Chem. Chem. Phys.* 20.13 (2018), pp. 8897–8908. DOI: 10.1039/C8CP00544C.

[150] M. F. Calhoun, C. Hsieh, and V. Podzorov. "Effect of Interfacial Shallow Traps on Polaron Transport at the Surface of Organic Semiconductors". In: *Phys. Rev. Lett.* 98.9 (2007), p. 096402. DOI: 10.1103/PhysRevLett.98.096402.

[151] C. Li, L. Duan, H. Li, and Y. Qiu. "Universal Trap Effect in Carrier Transport of Disordered Organic Semiconductors: Transition from Shallow Trapping to Deep Trapping". In: *J. Phys. Chem. C* 118.20 (2014), pp. 10651–10660. DOI: 10.1021/jp5022906.

[152] C. Ucurum, H. Goebel, F. A. Yildirim, W. Bauhofer, and W. Krautschneider. "Hole trap related hysteresis in pentacene field-effect transistors". In: *J. Appl. Phys.* 104.8 (2008), p. 084501. DOI: 10.1063/1.2999643.

[153] J. Zaumseil and H. Sirringhaus. "Electron and Ambipolar Transport in Organic Field-Effect Transistors". In: *Chem. Rev.* 107.4 (2007), pp. 1296–1323. DOI: 10.1021/cr0501543.

[154] H. Sirringhaus. "Reliability of Organic Field-Effect Transistors". In: *Adv. Mater.* 21.38 (2009), pp. 3859–3873. DOI: 10.1002/adma.200901136.

[155] J. Bisquert. "Nanostructured Energy Devices: Equilibrium Concepts and Kinetics". In: Boca Raton, FL: Taylor & Francis, 2014. Chap. 2.

[156] H. Vázquez, W. Gao, F. Flores, and A. Kahn. "Energy level alignment at organic heterojunctions: Role of the charge neutrality level". In: *Phys. Rev. B.* 71.4 (2005), p. 041306. DOI: 10.1103/PhysRevB.71.041306.

[157] M. Linares et al. "On the Interface Dipole at the Pentacene-Fullerene Heterojunction: A Theoretical Study". In: *J. Phys. Chem. C.* 114.7 (2010), pp. 3215–3224. DOI: 10.1021/jp910005g.

[158] A. Kahn, N. Koch, and W. Gao. "Electronic Structure and Electrical Properties of Interfaces between Metals and π-Conjugated Molecular Films". In: *J. Polym. Sci. B Polym. Phys.* 41.21 (2003), pp. 2529–2548. DOI: 10.1002/polb.10642.

[159] B. H. Hamadani, D. A. Corley, J. W. Ciszek, J. M. Tour, and D. Natelson. "Controlling Charge Injection in Organic Field-Effect Transistors Using Self-Assembled Monolayers". In: *Nano Lett.* 6.6 (2006), pp. 1303–1306. DOI: 10.1021/nl060731i.

[160] Y. Morikawa, K. Toyoda, I. Hamada, S. Yanagisawa, and K. Lee. "First-principles theoretical study of organic/metal interfaces: Vacuum level shifts and interface dipoles". In: *Curr. Appl. Phys.* 12.3 (2012), S2–S9. DOI: 10.1016/j.cap.2012.06.021.

[161] J. Veres, S. D. Ogier, S. W. Leeming, D. C. Cupertino, and S. M. KhaffafF. "Low-k Insulators as the Choice of Dielectrics in Organic Field-Effect Transistors". In: *Adv. Funct. Mater.* 13.3 (2003), pp. 199–204. DOI: 10.1002/adfm.200390030.

[162] S. Kobayashi et al. "Control of carrier density by self-assembled monolayers in organic field-effect transistors". In: *Nat. Mater.* 3.5 (2004), pp. 317–322. DOI: 10.1038/nmat1105.

[163] C. Celle et al. "Interface dipole: Effects on threshold voltage and mobility for both amorphous and poly-crystalline organic field effect transistors". In: *Organic Electronics.* 15.3 (2014), pp. 729–737. DOI: 10.1016/j.orgel.2014.01.003.

[164] T. Nagase, T. Hirose, T. Kobayashi, R. Ueda, A. Otomo, and H. Naito. "Influence of Substrate Modification with Dipole Monolayers on the Electrical Characteristics of Short-Channel Polymer Field-Effect Transistors". In: *Appl. Sci.* 8.8 (2012), p. 1274. DOI: 10.3390/app8081274.

[165] S. Enengl et al. "Spectroscopic characterization of charge carriers of the organic semiconductor quinacridone compared with pentacene during redox reactions". In: *J. Mater. Chem. C.* 4.43 (2016), pp. 10265–10278. DOI: 10.1039/C6TC02717B.

[166] X. Strakosas, M. Bongo, and R. M. Owens. "The organic electrochemical transistor for biological applications". In: *J. Appl. Polym. Sci.* 132.15 (2015), p. 41735. DOI: 10.1002/app.41735.

[167] E. Zeglio and O. Inganäs. "Active Materials for Organic Electrochemical Transistors". In: *Adv. Mater.* 30.44 (2018), p. 1800941. DOI: 10.1002/adma.201800941.

[168] W. F. Pasveer, P. A. Bobbert, and M. A. J. Michels. "Temperature and field dependence of the mobility in 1D for a Gaussian density of states". In: *Phys. Stat. Sol. (c)* 1.1 (2004), pp. 164–167. DOI: 10.1002/pssc.200303631.

[169] W. F. Pasveer et al. "Unified Description of Charge-Carrier Mobilities in Disordered Semiconducting Polymers". In: *Phys. Rev. Lett.* 94.20 (2005), p. 206601. DOI: 10.1103/PhysRevLett.94.206601.

[170] A. Miller and E. Abrahams. "Impurity Conduction at Low Concentrations". In: *Phys. Rev.* 120.3 (1960), p. 745. DOI: 10.1103/PhysRev.120.745.

[171] A. H. Fallahpour et al. "Modeling and simulation of energetically disordered organic solar cells". In: *J. Appl. Phys.* 116.18 (2014), p. 184502. DOI: 10.1063/1.4901065.

[172] F. Santoni, A. Gagliardi, M. Auf der Maur, and A. Di Carlo. "The relevance of correct injection model to simulate electrical properties of organic semiconductors". In: *Organic Electronics* 15.7 (2014), pp. 1557–1570. DOI: 10.1016/j.orgel.2014.04.023.

[173] K. D. Meisel et al. "Charge-carrier mobilities in disordered semiconducting polymers: effects of carrier density and electric field". In: *Phys. Stat. Sol. (c)* 3.2 (2006), pp. 267–270. DOI: 10.1002/pssc.200562718.

[174] J. Frenkel. "On Pre-Breakdown Phenomena in Insulators and Electronic Semi-Conductors". In: *Phys. Rev.* 54.8 (1938), p. 647. DOI: 10.1103/PhysRev.54.647.

[175] L. Wang, D. Fine, D. Basu, and A. Dodabalapur. "Electric-field-dependent charge transport in organic thin-film transistors". In: *J. Appl. Phys.* 101.5 (2007), p. 054515. DOI: 10.1063/1.2496316.

[176] A. Pivrikas, M. Ullah, H. Sitter, and N. S. Sariciftci. "Electric field dependent activation energy of electron transport in fullerene diodes and field effect transistors: Gill's law". In: *Appl. Phys. Lett.* 98.9 (2011), p. 092114. DOI: 10.1063/1.3557503.

[177] I. I. Fishchuk et al. "Electric field dependence of charge carrier hopping transport within the random energy landscape in an organic field effect transistor". In: *Phys. Rev. B.* 86.4 (2012), p. 045207. DOI: 10.1103/PhysRevB.86.045207.

[178] W. D. Gill. "Drift mobilities in amorphous charge-transfer complexes of trinitrofluorenone and poly-n-vinylcarbazole". In: *J. Appl. Phys.* 43.13 (1972), p. 5033. DOI: 10.1063/1.1661065.

[179] A. Bolognesi et al. "Effects of grain boundaries, field-dependent mobility, and interface trap States on the electrical Characteristics of pentacene TFT". In: *IEEE Trans. Elec. Dev.* 51.12 (2004), pp. 1997–2003. DOI: 10.1109/TED.2004.838333.

[180] M. Darwish, H. Boysan, C. Liewald, B. Nickel, and A. Gagliardi. "A resistor network simulation model for laser-scanning photo-current microscopy to quantify low conductance regions in organic thin films". In: *Organic Electronics* 62 (2018), pp. 474–480. DOI: 10.1016/j.orgel.2018.08.002.

[181] M. Fontana et al. "Electron-hole transport and photovoltaic effect in gated MoS_2 schottky junctions". In: *Sci. Rep.* 3.1634 (2013). DOI: 10.1038/srep01634.

[182] M. Buscema et al. "Large and tunable photothermoelectric effect in single-layer MoS_2". In: *Nano Lett.* 13.2 (2013), pp. 358–363. DOI: 10.1021/nl303321g.

[183] C-C. Wu et al. "Elucidating the photoresponse of ultrathin MoS_2 field-effect transistors by scanning photocurrent microscopy". In: *J. Phys. Chem. Lett.* 4.15 (2013), pp. 2508–2513. DOI: 10.1021/jz401199x.

[184] B. C. St-Antoine, D. Menard, and R. Martel. "Position sensitive photothermoelectric effect in suspended single-walled carbon nanotube films". In: *Nano Lett.* 9.10 (2019), pp. 3503–3508. DOI: 10.1021/nl901696j.

[185] B. C. St-Antoine, D. Menard, and R. Martel. "Photothermoelectric effects in single-walled carbon nanotube films: reinterpreting scanning photocurrent experiments". In: *Nano Res.* 5.2 (2012), pp. 73–81. DOI: 10.1007/s12274-011-0186-x.

[186] D. Sun et al. "Ultrafast hot-carrier-dominated photocurrent in graphene". In: *Nat. Nanotech.* 7.2 (2012), pp. 114–118. DOI: 10.1038/nnano.2011.243.

[187] A. J. Grant, T. M. Griffiths, G. D. Pitt, and A. D. Yoffe. "The electrical properties and the magnitude of the indirect gap in the semiconducting transition metal dichalcogenide layer crystals". In: *J. Phys. C: Solid State Phys.* 8.1 (1975), pp. 17–23. DOI: 10.1088/0022-3719/8/1/004.

[188] K. F. Mak, C. Lee, J. Hone, J. Shan, and T. F. Heinz. "Atomically thin MoS_2: a new direct-gap semiconductor". In: *Phys. Rev. Lett.* 105.13 (2010), p. 136805. DOI: 10.1103/PhysRevLett.105.136805.

[189] A. Splendiani et al. "Emerging photoluminescence in monolayer MoS_2". In: *Nano Lett.* 10.14 (2010), pp. 1271–1275. DOI: 10.1021/nl903868w.

[190] H. S. Lee et al. "MoS_2 nanosheet phototransistors with thickness-modulated optical energy gap". In: *Nano Lett.* 12.7 (2012), pp. 3695–3700. DOI: 10.1021/nl301485q.

[191] M. R. Esmaeili-Rad and Sayeef Salahuddin. "High performance molybdenum disulfide amorphous silicon heterojunction photodetector". In: *Sci. Rep.* 3 (2013), p. 2345. DOI: 10.1038/srep02345.

[192] O. Lopez-Sanchez, D. Lembke, M. Kayci, A. Radenovic, and A. Kis. "Ultrasensitive photodetectors based on monolayer MoS_2". In: *Nat. Nanotech.* 8 (2013), pp. 497–501. DOI: 10.1038/nnano.2013.100.

[193] S. L. Howell et al. "Investigation of band-offsets at monolayer-multilayer MoS_2 junctions by scanning photocurrent microscopy". In: *Nano Lett.* 15.4 (2015), pp. 2278–2284. DOI: 10.1021/nl504311p.

[194] J. J. Wierer Jr., Q. Li, D. D. Koleske, S. R. Lee, and G. T. Wang. "III-nitride core–shell nanowire arrayed solar cells". In: *Nanotechnology* 23.19 (2012), p. 194007. DOI: 10.1088/0957-4484/23/19/194007.

[195] A. Polman and H. A Atwater. "Photonic design principles for ultrahigh-efficiency photovoltaics". In: *Nat. Mater.* 11.3 (2012), pp. 174–177. DOI: 10.1038/nmat3263.

[196] S. L. Howell et al. "Spatial mapping of efficiency of GaN/InGaN nanowire array solar cells using scanning photocurrent microscopy". In: *Nano Lett.* 13.11 (2013), pp. 5123–5128. DOI: 10.1021/nl402331u.

[197] D. Knipp and J. E. Northhup. "Electric-field-induced gap states in pentacene". In: *Adv. Mater.* 21.24 (2009), pp. 2511–2515. DOI: 10.1002/adma.200802173.

[198] J. E. Northhup and M. L. Chabinyc. "Gap states in organic semiconductors: hydrogen- and oxygen-induced states in pentacene". In: *Phys. Rev. B* 68.4 (2003), p. 041202. DOI: 10.1103/PhysRevB.68.041202.

[199] A. Salleo et al. "Intrinsic hole mobility and trapping in a regioregular poly(thiophene)". In: *Phys. Rev. B* 70.11 (2004), p. 115311. DOI: 10.1103/PhysRevB.70.115311.

[200] C. Westermeier, A. Cernescu, S. Amarie, C. Liewald, F. Keilmann, and B. Nickel. "Sub-micron phase coexistence in small-molecule organic thin films revealed by infrared nano-imaging". In: *Nat. Commun.* 5.4101 (2014), p. 1. DOI: 10.1038/ncomms5101.

[201] M. W. B. Wilson, A. Rao, B. Ehrler, and R. H. Friend. "Singlet Exciton Fission in Polycrystalline Pentacene: From Photophysics towards devices". In: *Acc. Chem. Res.* 46.6 (2013), pp. 1330–1338. DOI: 10.1021/ar300345h.

[202] H. Marciniak et al. "Ultrafast Exciton Relaxation in Microcrystalline Pentacene Films". In: *Phys. Rev. Lett.* 99.17 (2007), p. 176402. DOI: 10.1103/PhysRevLett.99.176402.

[203] C. Westermeier, M. Fiebig, and B. Nickel. "Mapping of Trap Densities and Hotspots in Pentacene Thin-Film Transistors by Frequency-Resolved Scanning Photoresponse Microscopy". In: *Adv. Mater.* 25.40 (2013), pp. 5719–5724. DOI: 10.1002/adma.201300958.

[204] D. V. Lang, X. Chi, T. Siegrist, A. M. Sergent, and A. P. Ramirez. "Amorphouslike Density of Gap States in Single-Crystal Pentacene". In: *Phys. Rev. Lett.* 93.8 (2004), p. 086802. DOI: 10.1103/PhysRevLett.93.086802.

[205] M. Fiebig, C. Erlen, M. Göllner, P. Lugli, and B. Nickel. "Spatially resolved photoresponse measurements on pentacene thin-film transistors". In: *Appl. Phys. A* 95.1 (2009), pp. 113–117. DOI: 10.1007/s00339-008-5009-x.

[206] C. Liewald, D. Reiser, C. Westermeier, and B. Nickel. "Photocurrent microscopy of contact resistance and charge carrier traps in organic field-effect transistors". In: *Appl. Phys. Lett.* 109 (2016), p. 053301. DOI: 10.1063/1.4960159.

[207] F. Y. Wu. "Theory of resistor networks: the two-point resistance". In: *J. Phys. A: Math. Gen* 37.26 (2004), pp. 6653–6673. DOI: 10.1088/0305-4470/37/26/004.

[208] J. R. Brews. "A charge-sheet model of the MOSFET". In: *Solid-State Electron.* 21.2 (1978), pp. 345–355. DOI: 10.1016/0038-1101(78)90264-2.

[209] R. Schmechel, M. Ahles, and H. von Seggern. "A pentacene ambipolar transitor: Experiment and theory". In: *J. Appl. Phys.* 98.8 (2005), p. 084511. DOI: 10.1063/1.2106009.

[210] D. Knipp, K. Y. Chan, A. Gordijn, M. Marinkovic, and H. Stiebig. "Ambipolar charge transport in microcrystalline silicon thin-film transistors". In: *J. Appl. Phys.* 109.2 (2011), p. 02504. DOI: 10.1063/1.3531990.

[211] A. Risteska, K. Y. Chan, T. D. Anthopoulos, A. Gordijn, H. Stiebig, M. Nakamura, and D. Knipp. "Designing organic and inorganic ambipolar thin-film transistors and inverters: Theory and experiment". In: *Organic Electronics* 13.12 (2012), pp. 2816–2824. DOI: 10.1016/j.orgel.2012.08.038.

[212] W. L. Kalb and B. Batlogg. "Calculating the trap density of states in organic field-effect transistors from experiment: A comparison of different methods". In: *Phys. Rev. B.* 81.3 (2010), 035327(1–13). DOI: 10.1103/PhysRevB.81.035327.